

UNIVERSITÉ LILLE1 SCIENCE ET TECHNOLOGIES

THÈSE N° d'Ordre: 42202

Présentée pour l'obtention du grade de:

Docteur de l'Université de Lille 1

Spécialité :

Sciences de la Matière, du Rayonnement et de l'Environnement

Par:

VALENTYN BOVCHALIUK

**Aerosols properties as retrieved from the
GARLLIC synergetic approach applied to
multi wavelength Raman LiDAR
observations performed over Lille and
Dakar sites**

Thèse soutenue le 6 décembre 2016 devant le jury composé de:

I. Veselovskii	Deputy Director of PIC at GPI	PIC/GPI, Troitsk	rapporteur
V. Amiridis	Senior Researcher	IAASARS/NOA, Athens	rapporteur
J. Pelon	Directeur de Recherche CNRS	LATMOS, Paris 6	examineur
O. Dubovik	Directeur de Recherche CNRS	LOA, Lille 1	examineur
G. Milinevsky	Head of the SPL	TSNUK, Kyiv	examineur
P. Goloub	Professeur	LOA, Lille 1	directeur
D. Tanré	DRCE CNRS	LOA, Lille 1	co-directeur

Laboratoire d'Optique Atmosphérique

U.F.R. de Physique

Université Lille1 Science et Technologies

59655 Villeneuve d'Ascq

France

UNIVERSITÉ LILLE1 SCIENCE ET TECHNOLOGIES

Abstract

U.F.R. de Physique

Docteur de l'Université de Lille 1

**Aerosols properties as retrieved from the GARRLIC synergetic approach applied
to multi wavelength Raman LiDAR observations performed over Lille and Dakar
sites**

by Valentyn BOVCHALIUK

Les aérosols sont une composante très variable de l'atmosphère terrestre et font l'objet d'une attention croissante de la communauté scientifique et de la société. Depuis 2005, le LOA développe une activité reconnue en instrumentation, observation et inversion LiDAR pour la mesure des profils verticaux des paramètres descriptifs de ces aérosols. Depuis 2011, cette nouvelle thématique est soutenue par le projet européen ACTRIS (Aerosol Cloud and Trace gas Infrastructure) et le Labex CaPPA (Chemical and Physical Properties of the Atmosphere). Le premier objectif de cette thèse visait à déployer un nouveau LiDAR multi-longueur d'onde-Raman-polarisé, LILAS, d'une part sur la plateforme de mesures atmosphériques de l'université de Lille et d'autre part sur la station de géophysique de l'IRD à Dakar dans le cadre de la campagne de terrain SHADOW-2. Le second objectif visait à restituer puis étudier les propriétés optiques et microphysiques des couches aérosols détectées. Une méthodologie d'inversion innovante GARRLIC/GRASP a été mise en oeuvre et améliorée pour interpréter une série d'événements aérosols (pollution locale, poussières minérales d'origine désertique transportées jusqu'à Lille mais également observées à Dakar, proche des zones sources). Cette nouvelle technique d'inversion combine les mesures primaires issues de la photométrie solaire (épaisseur optique et luminances spectrales) avec les profils de retrodiffusion LiDAR à 355, 532 et 1064 nm. Les propriétés des aérosols ambiants étant également fonction de l'humidité atmosphérique, une dernière partie a porté sur la mesure du profil de rapport de mélange de la vapeur d'eau accessible à partir de LILAS.

Mots-Clefs

Aérosols atmosphériques, Télédétection, Propriétés optiques, Humidité, Vapeur, Lidar, Photométrie, Inversion (géophysique)

Aerosol particles are a highly variable component of the atmosphere and are now studied by a wide community. Since 2005, LOA is developing a recognized expertise in LiDAR observation devoted to aerosols profiling. Since 2011 this activity is supported by ACTRIS (Aerosol Cloud and Trace gas Infrastructure) and CaPPA (Chemical And Physical Properties of the Atmosphere) projects. The first objective of this work was to build, set up and characterize a new multi-wavelength Raman Polarized LiDAR (LILAS) operating at LOA observation platform located on the Campus. This system has also been operating during the SHADOW-2 field campaign (2015-2016) in M'Bour, near Dakar (Sénégal) at the IRD station. The second objective of the thesis consisted in developing aerosols retrievals and analyzing aerosols retrievals in term of optical and microphysical properties. An innovating synergetic approach (GARLIC/GRASP) has been used and improved to interpret several aerosol events (local pollution, mineral dust transported to Lille and mineral dust detected in Dakar, close to sources). This new technique is combining primary data obtained from sun/sky photometer (spectral AOD and spectral radiance) and elastic LiDAR backscattering profiles (355, 532 and 1064 nm). Since aerosols properties are sensitive to atmospheric humidity, last part of the work has been devoted to profiling water vapor mixing ratio from LILAS night-time data.

Key Words

Atmospheric aerosols, Remote Sensing, Optical properties, Humidity, vapor, Lidar, Photometry, Inversion (geophysics)

Acknowledgements

I would like to gratefully thank my scientific advisers Philippe Goloub and Didier Tanre for wise guidance and thorough support.

Many thanks to Oleg Dubovik and Igor Veselovskii for their help and support on all scientific questions. I sincerely appreciate the efforts of the Vassilis Amiridis for the reviewing the manuscript.

I want to thank everyone who directly or indirectly helped me to understand more about aerosols, their properties, physics of scattering and about all the instrumentations which were used during my thesis. Thanks to my colleagues Anton Lapatsin, Pavel Litvinov, Tatiana Lapyonok, Xin Huang, Benjamin Torres, Augustin Mortier, Yevgeni Derimian, Andrii Holdak, Fabrice Ducos and Christine Deroo for their help in the comprehension and adaptation of the programming codes. Many thanks to Thierry Podvin, Aleksandr Lapyonok and Luc Blarel for their help in instrumentation understanding. To my friends and fellow students Qiaoyun Hu, Kaitao Li, Florin Unga, Ioana Popovici, Lucia Deaconu, Rita Nohra and Laura Rivellini for support and all the fun. Special thanks to Anne Priem, Anne Burlet-Parendel and Marie-Lyse Liévin for all the help with bureaucratic runaround.

Also, I would like to say many thanks to my wife Yuliia, to my brother Andrii and all my family for their understanding and huge support.

Finally, I would like to thank all staff of LOA for their hospitality and friendliness that I was surrounded during my work in Lille.

Contents

Abstract	iv
Acknowledgements	vii
1 Introduction	1
1.1 Introduction	1
1.2 Objectives and outline of the thesis	5
2 Fundamentals	7
2.1 Aerosols and climate	7
2.1.1 How to observe aerosols?	9
2.1.2 Aerosol types	11
Anthropogenic pollutions	12
Biomass Burning aerosols	13
Mineral Dust	13
2.2 Basic radiometric quantities	14
2.3 Light scattering and absorption by atmospheric molecules and aerosols .	16
2.4 Aerosol properties	21
2.4.1 Optical properties	21
Aerosol Optical Depth	21
Single Scattering Albedo	23
Phase matrix and scattering phase function	23
LiDAR and depolarization ratios	25
2.4.2 Microphysical properties	26
2.5 Water vapor, mixing ratio and relative humidity	28
2.6 LiDAR principle, equation and types	30
2.6.1 LiDAR principle	30
2.6.2 LiDAR equation	30
2.6.3 LiDARs types	34
Elastic backscatter LiDAR and depolarization	36
Inelastic or Raman LiDAR	37
2.7 From optical to microphysical aerosol properties: inverse methods . . .	38
3 Experimental sites, instrumentation and modelling tools	41
3.1 Lille and Dakar super-sites	41
3.2 LILAS system	42
3.2.1 LILAS Quality Assurance Procedures	43
3.2.2 LILAS operation and database	47
3.3 CIMEL photometer	51
3.4 Radiosoundings	53
3.5 Modelling tools	54

3.5.1	NMMB/BSC-Dust model	54
3.5.2	HYSPLIT model	54
4	Methodologies to retrieve aerosol properties	57
4.1	Retrieval of optical properties	58
4.1.1	Method which uses sun/sky-photometer primary measurements	58
4.1.2	Methods using LiDAR data	59
a)	Klett method	59
b)	Raman method	60
4.1.3	Method combining sun-photometer and LiDAR measurements .	61
4.2	Retrieval of microphysical properties	62
4.2.1	Inversion of sun/sky-photometer data	62
4.2.2	Inversion of LiDAR data	63
4.2.3	Inversions based on synergy between sun/sky-photometer and LiDAR data	65
4.3	GARRLiC algorithm	68
4.3.1	General description	68
Forward model		69
Numerical inversion		72
4.3.2	Enhancements implemented into the GARRLiC algorithm	74
Molecular extinction and backscatter profiles		74
New normalization procedure		75
Conclusions and advantages		76
5	Application of GARRLiC to data of SHADOW-2 (Phase 1) campaign	79
5.1	Comparison between Raman, LIRIC and Regularization retrievals	80
5.2	Conclusions	96
6	Water vapor mixing ratio profile. Calibration and application	97
6.1	Water vapor and Raman LiDAR measurements	97
6.2	LiDAR mixing ratio calibration	98
6.2.1	Intercomparison with radiosonde measurements	99
6.2.2	Calibration by TWP using lunar-photometer measurements	103
6.2.3	Comparison of obtained calibration constants	107
6.3	Applications	109
6.3.1	Application to measurements over Lille site	109
6.3.2	Application to measurements over Dakar site	110
6.4	Conclusions	114
7	Conclusions and perspectives	117
	Bibliography	123

List of Figures

1.1	Radiative forcing estimates by different constituents of the atmosphere	3
1.2	Aerosol influences on climate	4
2.1	Different aerosols collected at Lille and Dakar observational sites	8
2.2	Representation of differential solid angle	15
2.3	Spectral radiant flux	15
2.4	Solar spectrum on the top and bottom of the atmosphere	17
2.5	Angular dependence of Rayleigh and Mie scattering	19
2.6	Schematic representation of light attenuation through the medium	20
2.7	Representation of scattering phase function of the Rayleigh and Mie scattering	25
2.8	Standard LiDAR setup	31
2.9	Illustration of LiDAR geometry	33
3.1	LILAS photo at Lille site	43
3.2	LILAS and CAML (CIMEL) beams at Dakar site during the observation	44
3.3	LILAS optical scheme	44
3.4	EARLINET check up: Rayleigh fit	45
3.5	EARLINET check up: telecover test	46
3.6	Example of Volume Depolarization Ratio, quick look	47
3.7	Example of volume depolarization ratio, profile	48
3.8	Example of LILAS data level 1.0	50
3.9	Example of LILAS data gluing	52
4.1	Sun-photometer almucantar and principle plane geometries	62
4.2	GARRLiC inversion structure	66
4.3	GARRLiC products derived using single or two mode inversion	67
4.4	Modeling of two aerosol components in GARRLiC algorithm	68
4.5	GARRLiC general scheme	69
4.6	GARRLiC assumption on aerosol volume concentration above and below trustworthy LiDAR altitude range	73
5.1	AOD during SHADOW-2 Phase 1	80
6.1	LILAS MR profile obtained using intercomparison calibration technique	101
6.2	Calibration constants obtained using intercomparison technique	102
6.3	Calibration constants obtained using LP TPW calibration technique	106
6.4	LILAS MR profile obtained using LP TPW calibration technique	106
6.5	LILAS MR profiles obtained using both calibration techniques	108
6.6	Height-temporal distribution of LILAS MR over Lille on 25 November 2014	109

6.7	Back trajectory for Lille site at 04:00 UTC, 25 November 2014	110
6.8	LILAS MR profile on 25 November 2014	110
6.9	Height–temporal distribution of AOT, mixing ratio, particle depolarization ratio, and LiDAR ratio over Dakar on 15–16 March 2015	112
6.11	Height–temporal distribution of LILAS MR over Dakar on 16 March 2015	113
6.12	LILAS MR profile on 16 April 2015	114

List of Tables

2.1	Typical properties for different wet and dry aerosol types	12
4.1	Typical Raman LR at 532 nm for different aerosol types	61
6.1	Calibration constants and TPW obtained using intercomparison and LP TWP calibration techniques	107

List of Abbreviations

LOA	Laboratoire d'Optique Atmosphérique
CaPPA	Chemical and Physical Properties of the Atmosphere
SHADOW-2	Study Saharan dust over the West Africa second campaign
LILAS	Lille LIDAR AtmosphereS
LIRIC	LIDAR-Radiometer Inversion Code
GARRLiC	Generalized Aerosol Retrieval from Radiometer and LIDAR Combined data
AERONET	Aerosol Robotic Network
EARLINET	European Aerosol Research LIDAR Network
MPLINET	Micro-Pulse LIDAR Network
LALINET	Latin American LIDAR Network
ADNET	Asian Dust Network
GAW	Global Atmosphere Watch
GALION	Global Aerosol LIDAR Observation Network
NDACC	Network for the Detection of Atmospheric Composition Change
RF	Radiative Forcing
POM	Particles of organic matters
VOC	Volatile organic compounds
OC	Organic carbon
BC	Black carbon
CCN	Cloud condensation nuclei
TOA	Top of Atmosphere
MODIS	Moderate Resolution Imaging Spectroradiometer
PLASMA	Photomètre Léger Aéroporté pour la Surveillance des Masses d'Air
NMMB/BSC-Dust	Non-hydrostatic Multiscale Model, Barcelona Supercomputing Center
HYSPLIT	Hybrid Single-Particle Lagrangian Integrated Trajectory
GDAS	Global Data Assimilation System
NOAA	National Oceanic and Atmospheric Administration
LR	LIDAR ratio
LS	LIDAR signal
AE	Angström exponent
SD	Size distribution
CRI	Complex refractive index
AOD	Aerosol optical depth
SSA	Single scattering albedo
TWP	Total precipitable water
WV	Water vapor
RCS	Range corrected signal
LSM	Least square method

List of Symbols

λ	wavelength	nm
σ^{ext}	extinction coefficient	m^{-1}
σ^{sca}	scattering coefficient	m^{-1}
$\sigma^{sca,cs}$	scattering cross section coefficient	$m^2 sr^{-1}$
σ^{abs}	absorption coefficient	m^{-1}
Q_{abs}	absorption efficiency factor	
Q_{sca}	scattering efficiency factor	
β	backscatter coefficient	$m^{-1} sr^{-1}$
ω_0	single scattering albedo	
θ'	zenith angle	$^\circ, deg$
θ	scattering angle	$^\circ, deg$
$\mathbf{P}(\theta)$	phase matrix	
$P_{11}(\theta)$	scattering phase function	
δ	depolarization ratio	
α	Angström exponent	
α^{ext}	extinction Angström exponent	
τ	optical thickness	
m_0	relative air mass	
r_{eff}	effective radius	μm
Ω	solid angle	sr
Φ_e	radiant flux	W or J/s
Φ_λ	spectral flux	W/nm^{-1}
I_λ	spectral intensity	$W sr^{-1} nm^{-1}$
L_λ	spectral radiance	$W/(m^2 sr nm)$
x	size parameter	
m	complex refractive index	
n	real part of complex refractive index (RRI)	
k	imaginary part of complex refractive index (IRI)	
$N(r)$	number particle size distribution	μm^{-2}
$S(r)$	surface particle size distribution	$m^2 \mu m^{-2}$

$V(r) = \frac{dV}{d\ln(r)}$	volume particle size distribution	$\mu m^3 \mu m^{-2}$
V	volume of particles	$\mu m^3 \mu m^{-3}$
N	number concentration	m^{-3}
TPW	total precipitable water content	$cm, g cm^{-1}$
$w_{nc}(z)$	not calibrated mixing ratio profile	
$w(z)$	water vapor mixing ratio	$g kg^{-1}$
$e(z)$	profile of water vapor pressure	Pa
$e_w(z)$	profile of saturation water pressure	Pa
$\rho_{H_2O,air}(z)$	water vapor and air densities	$g m^{-3}$
C_1	MR calibration constant using intercomparison technique	
C_2	MR calibration constant using LP TWP technique	
$P(R)$	power of backscattered radiation from distance R	mV
K	factor of LiDAR performance	
$G(R)$	factor of range dependent geometry	
$T(R)$	atmosphere transmittance	
P_{bg}	power of background noise	
V^{dp}	calibration constant of depolarization coefficient	
	coefficients of beam-splitter cube:	
T_p	for parallel light transmittance	
T_s	for perpendicular light transmittance	
R_p	for parallel light reflectance	
R_s	for perpendicular light reflectance	

Chapter 1

Introduction

1.1 Introduction

The globally averaged surface temperature of the Earth calculated by the linear trend shows a warming of 0.85 °C over the period from 1880 to 2012, and global surface temperature change for the end of the 21st century is likely to exceed 1.5 °C (Stocker et al., 2013). Temperature can be critical as it influences our world, where everything is interconnected. The temperature increase has been attributed to changes in the concentrations of greenhouse gases (Stocker et al., 2013). These atmospheric constituents are attributed to human activities; therefore it is possible to influence on their concentrations and globally "control" Earth's atmosphere system.

The Earth's atmosphere consists of gases and particles. There are two groups of gases, with nearly steady and with variable concentrations. Gases with residence times greater than about a decade are considered to be long-lived. Through the mixing and circulation of the atmosphere, these gases have concentrations that are to some extent uniform. Gases with short residence times, such as water vapor and ozone, are considered to be short-lived. They have high concentrations near their sources and low ones near their sinks (Coakley Jr. and Yang, 2014). There is very high confidence that well mixed greenhouse gases positively contribute to radiative forcing estimates (Fig. 1.1), which is defined as a net change of incoming and outgoing energy in the Earth's atmosphere system. Human activities are the main source of the additional greenhouse gases in the atmosphere, thus, by controlling emission of greenhouse gases we could warm up or cool down the atmosphere (Coakley Jr. and Yang, 2014).

Atmospheric components such as clouds and aerosol particles are highly variable in space and time. Aerosols are solid/liquid particles suspended in the atmosphere. Because of a wide variety of aerosols, it differently interacts with radiation. That is the main reason why during last decade significance of aerosol studies stays very vital. Aerosol analysis is complex and requires a lot of resources due to a wide variety of particle types and their mixtures. That is why, according to Stocker et al., 2013 aerosol still contribute the largest uncertainties in total radiative forcing estimates.

Many efforts have been devoted to aerosol studies for better understanding their impacts on a climate. According to Stocker et al., 2013, the radiative forcing of the total aerosol effect in the atmosphere, which includes cloud adjustments due to aerosols, is -0.9 [-1.9 to -0.1] Wm^{-2} (medium confidence). As it is seen from Fig. 1.1, most of the aerosols have negative forcing, and only positive contribution comes from black carbon, which absorbs solar radiation. There is high confidence that aerosols and their interactions with clouds have offset a substantial portion of global mean forcing from well-mixed greenhouse gases. Radiative forcing due to anthropogenic activities estimates in 2011 relative to 1750 is 2.29 [1.13 to 3.33] Wm^{-2} (Fig. 1.1). It has increased more rapidly since 1970, relative anthropogenic RF in 1970 to 1750 is 0.57 [0.29 to 0.85] Wm^{-2} . RF estimates in 2011 is 43% higher than reported in 2007 (IPCC, 2007), it was reported 1.6 [0.6 to 2.4] Wm^{-2} . It is explained by continuing growth of greenhouse gas concentration and due to improved RF estimate. Generally, it brings warming of the atmosphere and the ocean, in changes in the global water cycle, in reductions in snow and ice, etc.

Aerosols influence on climate can be divided into direct, indirect, and semi-direct effects (Fig. 1.2). Aerosols directly interact with radiation by scattering and absorbing mechanisms, and therefore, may result in warming or cooling of the atmosphere. If the total RF is positive in the atmosphere column it warms up the atmosphere, and if the total radiative forcing is negative it cools off the atmosphere. Warming and cooling processes depend on aerosols single scattering albedo and on the albedo of underlying surface (Haywood and Boucher, 2000).

Indirect effect consists in aerosols influence on cloud lifetime, height, albedo, and other cloud properties. The indirect influence can be divided into Twomey (Twomey,

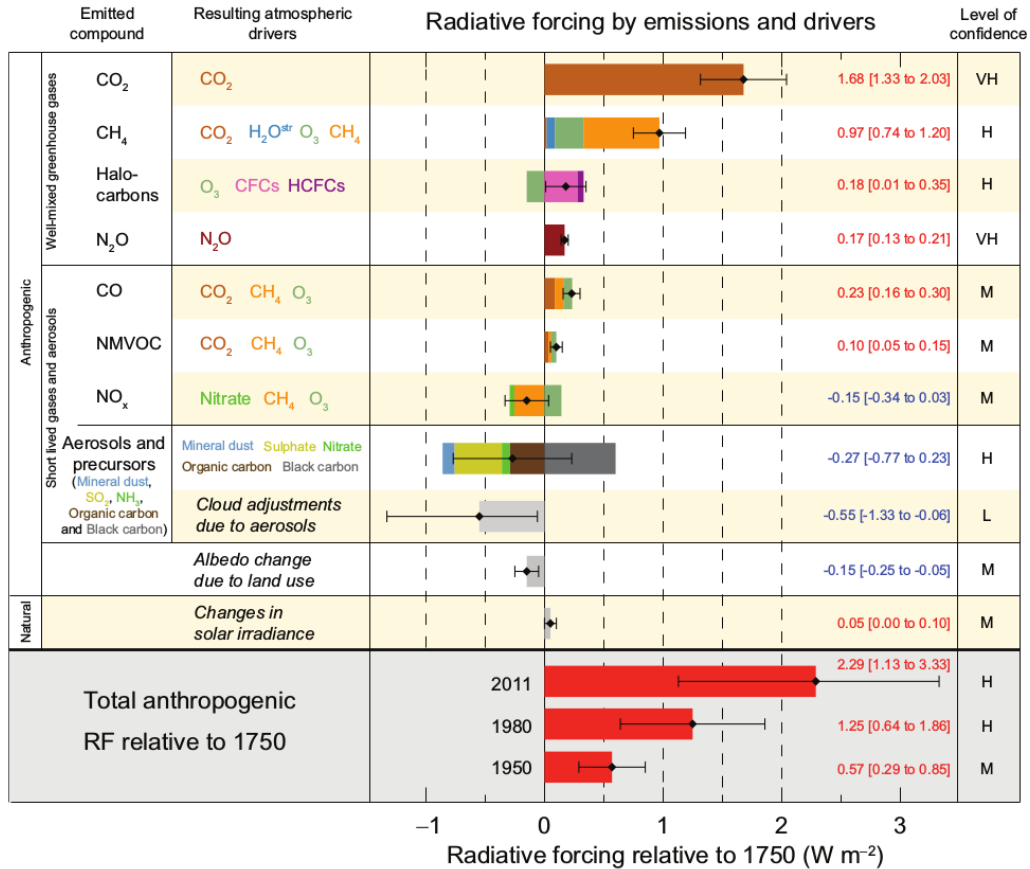


FIGURE 1.1: Radiative forcing estimates in 2011 relative to 1750 and aggregated uncertainties for the primary drivers of climate change. Values are global average radiative forcing, partitioned according to the emitted compounds or processes that result in a combination of drivers. The best estimates of the net radiative forcing are shown as black diamonds with corresponding uncertainty intervals. The numerical values are provided on the right of the figure, together with the confidence level in the net forcing (VH - very high, H - high, M - medium, L - low, VL - very low). Albedo forcing due to black carbon on snow and ice is included in the black carbon aerosol bar. Small forcings due to contrails (0.05 W m^{-2} , including contrail induced cirrus), and HFCs, PFCs and SF 6 (total 0.03 W m^{-2}) are not shown. Concentration-based RFs for gases can be obtained by summing the like-colored bars. Volcanic forcing is not included as its episodic nature makes it difficult to compare to other forcing mechanisms. Total anthropogenic radiative forcing is provided for three different years relative to 1750. Figure is taken from the summary for policymakers (Stocker et al., 2013).

1974; Twomey, 1977) and Albrecht (Albrecht, 1989) effects. In Twomey effect, the aerosols provide an additional nuclei for droplet or ice crystal growth (Twomey, 1974; Boucher, 1999; Lohmann, Kärcher, and Timmreck, 2003) and change the cloud albedo. In Albrecht effect, aerosols can change lifetime of clouds, liquid water content and top height of clouds (Albrecht, 1989; Pincus and Baker, 1994). Indirect effects depend on concentration and type of aerosols and clouds (Kaufman, Tanré, and Boucher, 2002;

Lohmann and Feichter, 2005).

Semi-direct effect consists in temperature profile modification by absorbing aerosols (Johnson, Shine, and Forster, 2004; Koch and Del Genio, 2010). Some tropospheric aerosols can absorb shortwave radiation and heat the atmosphere, it affects the relative humidity and stability of troposphere, and, thereby, influences on cloud formation and lifetime.

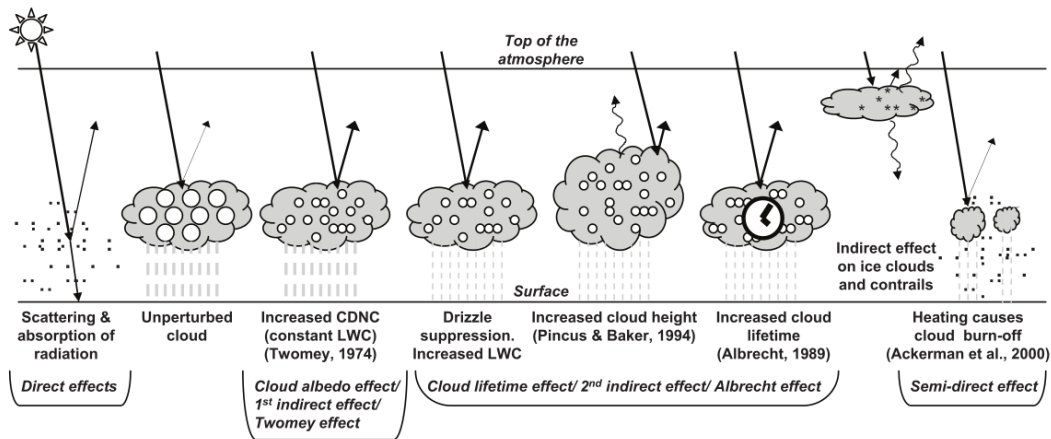


FIGURE 1.2: Schematic diagram showing the various radiative mechanisms associated with cloud effects that have been identified as significant in relation to aerosol (modified from Haywood and Boucher, 2000).

The uncertainties in estimation of the aerosols effects on RF are still high (Fig. 1.1) according to IPCC, 2007; IPCC, 2013. Improvements of observations, development of instrumentation and modeling are the main sources of enhancements in aerosol forcing estimations.

Under conditions of high relative humidity, an aerosol particle may growth due to the water uptake (hygroscopic growth) modifying aerosols size distribution. Water vapor (WV) affects the direct scattering of radiation (Hänel, 1976) and especially the indirect effects, the aerosol water uptake is highly related to their ability to act as cloud condensation nuclei (CCN) (Charlson et al., 1992). Thus, a better knowledge of WV content and relative humidity are in high importance of aerosol studies, in particular, their vertical distribution.

1.2 Objectives and outline of the thesis

Hence, during the thesis newly developed multi-wavelength Raman-polarization LiDAR called LILAS (Lille LiDAR AtmosphereS) was built, set up and used for measurements. Observations were carried out in West Africa and the adjacent oceanic region (SHADOW-2 campaign - a study of SaHAran Dust Over West Africa) which is very consequential location for studying dust properties. Some improvements have been implemented into the GARRLiC algorithm (Generalized Aerosol Retrieval from Radiometer and LiDAR Combined data) which were used for data analyses. Therefore, the first objective of the thesis was to build, set up and characterize a new multi-wavelength Raman-polarization LiDAR system. The second objective of the thesis consisted in an implementation of several improvements into the GARRLiC algorithm and in analyses of aerosol retrievals in terms of aerosol optical and microphysical properties.

LILAS direct measurements provide water vapor mixing ratio profile, which is a suitable tracer that indicates the boundary between dry air masses transported over the continent and moist air masses coming from the ocean. As we already mentioned it, WV vertical distribution is of high importance for aerosol studies. Therefore, last part of the thesis concerns the developed LILAS calibration techniques for water vapor mixing ratio measurements.

The thesis report is organized as followed:

- Chapter 2 is devoted to the description of basic concepts of aerosols, light scattering theory and fundamentals of lidar technique.
- Chapter 3 describes instruments which were used for the thesis and the observational sites in which measurements were carried out. Particular emphasis is made on LILAS LiDAR, its general description, its quality assurance procedures, its operation, and measurements. The procedure for processing the level 1.0 data from the raw data developed during the thesis, is described.

- Chapter 4 describes the methodologies which were used to obtain aerosol properties. Special emphasis is made on GARRLiC algorithm and on its enhancements implemented during the thesis.
- Chapter 5 presents the results of an application of the various methods described in Chapter 4. Results of GARRLiC application on LiDAR data which were carried out during SHADOW 2 campaign are presented and included as a paper (Bovchaliuk et al., 2016) published in Atmospheric Measurements Technique journal.
- Chapter 6 presents and discusses calibration techniques for LILAS measurements of water vapor mixing ratio. These calibration techniques were developed considering observational sites specification (distance between LiDAR and radiosonde measurements and lunar-photometer observation). The derived calibration constants were used in the application on LILAS measurements and are presented in the end of the chapter.
- The manuscript ends with conclusions and perspectives.

Chapter 2

Fundamentals

2.1 Aerosols and climate

Science and society are interested in aerosols for many reasons. High aerosol concentration can cause serious health hazard and have been linked to increasing in morbidity and mortality rates, and degradation of environmental quality concerning of air quality (Amiridis et al., 2012), acid rain and reduction of visibility (Lenoble, Remer, and Tanré, 2013). The decrease of visibility due to high attenuation by the aerosols is a grave concern for some military or civil sighting. Volcanic ash emissions can cause breakage of jet engines and disruption of air traffic (Kienle et al., 1990). In the polar regions aerosols play a major role in the heterogeneous atmospheric chemistry, in stratospheric clouds, they can depress ozone concentration (Andreae and Crutzen, 1997). However, one of the main reason of interest is aerosols influence on Earth's climate. They influence the energy budget and cause climate changes on the regional and global scales (Lenoble, Remer, and Tanré, 2013; IPCC, 2007; IPCC, 2013). As was mentioned above, their impacts can be divided in direct, indirect and semi-direct effects. By these effects aerosols increase/decrease energy budget and cause the Earth's atmosphere warming/cooling. Huge efforts are being performed to study aerosol effects on Earth's climate. The total aerosol effect in the atmosphere is -0.9 [-1.9 to -0.1] Wm^{-2} (IPCC, 2013), the uncertainties in the aerosol radiative forcing have been reduced with respect to IPCC, 2007. However, aerosol forcing continues contribute the largest uncertainties to the total radiative forcing estimate.

Aerosols are solid and/or liquid particles suspended in the atmosphere with the exception of clouds. We notice their presence because they scatter and absorb the sunlight. In case of high concentration, they can be seen as haze, smoke from fires, dust storm, etc. Most aerosols are concentrated in boundary layer near production sources. However, they can be lifted by air-masses up to 4-6 km in altitude and transported over long distances. In case of volcanic eruption or huge forest fires they can reach 10-12 km, and even higher altitudes in the stratosphere. Aerosol particles can be divided into two categories: (i) natural, formed by wind, erosion, volcanic eruptions and other natural processes; and (ii) anthropogenic, caused by human activities (Lenoble, Remer, and Tanré, 2013). Particles are removed from the atmosphere by dry deposition, evaporation, and settling with precipitation. Those, which have been emitted directly into atmosphere are called primary aerosol, and the ones formed by gas to particle conversion processes are called secondary aerosols. The size range of aerosol particles varies from few nanometers to tens of micrometers in diameter (Seinfeld and Pandis, 2006). Liquid particles are approximately spherical, whereas solid aerosols have different shapes (see Fig. 2.1). The time of the aerosol residence in the atmosphere varies from minutes for smallest particles that are coagulating rapidly to years for stratospheric particles.

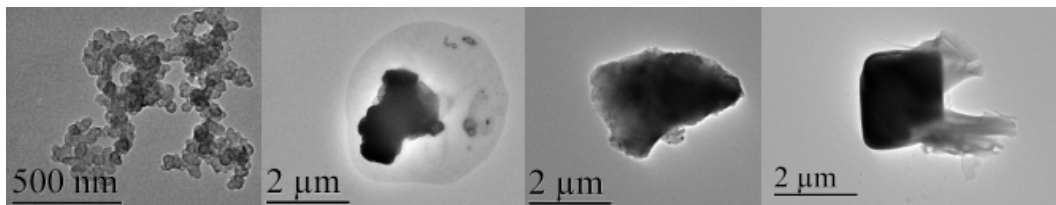


FIGURE 2.1: Wide variety of aerosol and their shapes, from left to right: soot collected at Lille, 29 March 2014; metallic (Iron) surrounded by a shell gathered at Lille, 13 March 2014; dust (Aluminum silicate) received at M'Bour at 2 km altitude during the flight, 10 April 2015; fresh sea salt (NaCl) collected at M'Bour during SHADOW-2 campaign at 3 km altitude during the flight, 10 April 2015 (Pictures from Choël Marie and Florin Unga, LASIR/LOA, 2015).

2.1.1 How to observe aerosols?

In situ and remote sensing measurements are two ways to observe the aerosols. The former is by means through direct interaction with particles at the point of observation. The latter allows measure aerosol properties from a distant point without direct interaction. Remote sensing can be categorized into "active" and "passive" techniques depending on instrumental design. Instruments used for passive remote sensing measures the properties of radiation scattered by particles and molecules whereas active instruments measure the scattered radiation emitted by themselves (the radiation source is a part of the system).

Ground based remote sensing techniques provide accurate results for aerosol characterization (Dubovik and King, 2000; Dubovik et al., 2011; Olmo et al., 2006; Klett, 1981; Ansmann, Riebesell, and Weitkamp, 1990). They provide aerosol properties at local scale. Observing networks have been established using systems with the same or similar measurement techniques to be more efficient and aiming to provide global coverage. Among such networks are EARLINET (European Aerosol Research Lidar Network, www.earlinet.org) (Pappalardo et al., 2014), MPLINET (Micro-Pulse Lidar Network) (Welton et al., 2001; Welton et al., 2005), LALINET (Latin American Lidar Network, www.lalinet.org) (Guerrero-Rascado et al., 2014), ADNET (Asian Dust Network) (Murayama et al., 2001), SKYNET (Takamura, Nakajima, et al., 2004) and AERONET (Aerosol Robotic Network, <http://aeronet.gsfc.nasa.gov/>) (Holben et al., 1998). Also, there is one global aerosol LiDAR network of networks, the GAW (Global Atmosphere Watch) Aerosol Lidar Observation Network (GALION). GALION does not consist of a uniform set of LiDAR systems which are sparsed through the Earth at different stations, but makes use of existing systems in already established stations, of the experienced operators of these systems, and of existing network structures. GALION includes EARLINET, NDACC (Network for the Detection of Atmospheric Composition Change), ADNET and MPLINET (Bösenberg et al., 2007).

Aerosol vertical distribution is important for radiative forcing estimation, especially for accounting indirect and semi-direct aerosol effects (Claquin et al., 1998; Meloni et

al., 2005; Samset et al., 2013). LiDAR instruments are very useful tool for the determination of the aerosol vertical distribution. Such systems are widely used, and variety of LiDAR techniques have been developed for aerosol studies (Klett, 1981; Ansmann, Riebesell, and Weitkamp, 1990; Shipley et al., 1983; Weitkamp, 2005). Depending on LiDAR capabilities, optical and/or microphysical aerosol properties can be derived. Extinction (σ), backscatter (β) and extinction to backscatter ratio (σ/β), so called LiDAR ratio (LR), coefficients refer to optical aerosol properties, whereas aerosol effective radius (r_{eff}), size distribution (SD), volume (V), mass, surface-area (S), number (N) concentrations and complex refractive index (CRI) are belonging to microphysical properties.

There are several methods used to retrieve aerosol properties from LiDAR measurements. However, in general, they can be divided into three main groups (Weitkamp, 2005). The methods from the first group are combining measurements from several different instruments. A preferred approach is to combine lidar and sun-photometer observations. In this case, the treatment of the data is more straightforward, the latter delivers integrated optical depths of the atmospheric column at multiple wavelengths. In the second group, the optical properties like σ and β are calculated by Mie-theory and then are compared with the corresponding properties obtained from Raman LiDAR technique (Wandinger et al., 1995; Barnaba and Gobbi, 2001). Optical properties are calculated using a priori assumptions. The application of these methods has been restricted to special cases (polar stratospheric clouds, ejecta from volcanic eruptions and other atmospheric processes with well-known type of particles) because of the uncertainties associated with such a priori assumptions. The third group, derived from the second one, aims at (i) reducing number of a priori constraints, and (ii) improving the ability to retrieve aerosol properties in the highly variable tropospheric conditions. These retrieval approaches consist of mathematical methods that use spectral LiDAR information (Uthe, 1982; Müller, Wandinger, and Ansmann, 1999; Veselovskii et al., 2002; Veselovskii et al., 2012; Shcherbakov, 2007). More detailed descriptions will be presented in Chapter 4.

2.1.2 Aerosol types

The term "aerosols" by itself is not well defined because of a wide variety of substances by which aerosols are presented. Even sub-classifications of aerosols such as dust or smoke are themselves generic terms because of many combinations of minerals or organics respectively (Lenoble, Remer, and Tanré, 2013). That is why, aerosols can be classified in many terms, according to their chemical composition, mechanism of formation, origin or size of particles. According to aerosols origin, they can be divided into natural and anthropogenic. Natural aerosols includes sea salt, desert dust, volcanic and biogenic emissions, a smoke of wildfires, and biomass burning. Anthropogenic aerosols caused by a human activity, which includes industrial emission, biomass burning for agriculture, land erosion and evaporation of lakes caused by human. According to formation mechanisms, particles which have been emitted directly into atmosphere are called primary aerosols, and the ones formed by a gas to particle conversion processes are called secondary aerosols. Regarding particle size, they can be divided in fine and coarse mode particles. Fine mode particles have diameter $<1 \mu m$, and consist of nucleation or Aitken mode, formed with particles in diameter range from 0.001 to 0.1 μm , and accumulation mode with diameters between 0.1 and 1 μm (Eck et al., 2010). Coarse mode particles have diameter in range from 1 to 100 μm , but most of coarse aerosol mass contained in range from 1 to 10 μm (Lenoble, Remer, and Tanré, 2013).

Aerosol optical properties, which are radiative characteristics, depend on the chemical composition of particles, their sizes and shapes. The composition is represented by the complex refractive indices (CRI), with the real (RRI) and imaginary (IRI) parts contributing to the determination their scattering and absorption properties. These properties can be measured in the laboratory or by in situ instrumentation during a campaign or at observational sites. In this case, such measurements will represent dry aerosol properties and not necessarily the ambient properties of aerosol layer, since several substances are hygroscopic. Some types of aerosols are easily combined with water vapor forming liquid particles with new optical and microphysical properties.

At best, aerosol can be divided into such types: (i) Sulfates; (ii) Black Carbon (BC); (iii)

Particles of Organic Matters (POM); (iv) Dust; and (v) Sea Salt. These aerosol types are also used in climatological models, which form aerosol from estimates of source emissions, then allow the particles to be transported by modeled meteorology, transformed from modeled chemical processes and removed from the atmosphere by modeled wet and dry deposition. In Table 2.1 presented physical properties of dry and wet particles (Lenoble, Remer, and Tanré, 2013). In the following subsection anthropogenic pollution, biomass burning and mineral dust are described with more details.

Physical property	Sulfate	BC	POM	Dust	Sea salt
Real part of refractive index (dry)	~1.53	~1.75	~1.53	~1.53	~1.50
Imaginary part of refractive index (dry)	~0.005	~0.440	~0.006	~0.008	~0.000
Real part of refractive index (wet)	1.35–1.45		1.35–1.45	1.48	1.35-1.45
Imaginary part of refractive index (wet)	~0.002		~0.003	~0.005	~0.000
Effective radius in μm	0.1–0.2		0.1–0.2	1.5–3.0	~ 1
Shape	sphere	*not sphere	sphere	not sphere	sphere

TABLE 2.1: Approximate typical physical properties for different aerosol types. Refractive index presented to 550nm, table taken from (Lenoble, Remer, and Tanré, 2013). *Black carbon (BC) originated as long non-spherical chains, but those chains collapse and are often incorporated in other organic matters (POM) that adds coating over the collapsed BC chains. Rarely BC is seen in its pure state in the real atmosphere.

Anthropogenic pollutions

Traffic and industrial emissions are the greatest sources of anthropogenic pollution, as well as particles originated from precursor gases (SO_2 , NO , NH_4 and volatile organic compounds or VOC). According to the size, they belong to fine mode particles and present spherical shape. These particles are small and that is why they can be transported far from their sources. Particles lifetime, in the atmosphere, varies from several to 15 days.

Primary anthropogenic aerosols compound from Organic Carbon (OC, generates during decaying vegetation, bacterial growth, and other natural processes) and Black Carbon (BC, forms by fossil flues, biomass burning, mainly from anthropogenic origin) (Bond et al., 2007). Secondary aerosol particles, which are originated from precursor gases, mainly compounds from sulfates and nitrates. Sulfates are generated from the oxidation of SO_2 (thermal power plants and industrial activities are emitting sulfates), and nitrates are formed from oxidation of NO_x (traffic and industrial activities are emitting nitrates).

Biomass Burning aerosols

Biomass burning describes the burning of living and dead vegetation. Burning can be caused by anthropogenic (land clearing for further use) and natural (wildfires are also frequent) reasons.

Biomass burning aerosols consist of two major chemical components: BC which primarily absorbs solar radiation and OC which primarily scatters solar radiation. Both usually have a high fine mode contribution. Black carbon originated as long non-spherical chains, but those chains collapse and are often incorporated in other organic matters that adds coating over the collapsed BC chains. Hence, particle properties of both OC and BC are strongly varied depending on the burning process or the processes during the transport (hygroscopic growth, coagulation or photochemical mechanisms, etc.) (Amiridis et al., 2009a; Ancellet et al., 2016; Müller et al., 2007).

Mineral Dust

Mineral dust particles are non-spherical with highly irregular shapes (Fig. 2.1). The size of particles can vary from $0.4 \mu m$ to tens of micrometers. Dust particles are picked up by wind erosion and can be transported at huge distances. For instance, the Saharan dust has formed the coast of Florida (Prospero, 1996; Joseph, 1999; Muhs et al., 2007). But in the same time, because of high weight, the lifetime of the dust aerosols is small, and most of the particles are settling down in few days (up to 7) (Lenoble, Remer, and Tanré, 2013; Freudenthaler et al., 2009). Besides the natural sources, dust

emission is assumed to have a significant anthropogenic component mainly originating from agricultural and industrial practices. Some authors estimate the contribution of anthropogenic dust into annual dust emission about 50-70% (Washington et al., 2003), the annual emission is about 1600 [700-4000] Tg/year. There are a lot of mineral dust sources around the world, among them are Sahara desert in Northern Africa, Wahiba Sands in the Middle East, Makran coastal zone and a broad area of central Pakistan in Southwest Asia, Tarim Basin, Gobi and Mongolia region in China, Mojave and Colorado deserts in North America, etc.

In view of the fact that mineral dust has high annual emission and global coverage, it has global climate effect. This effect is complex, because of wide variety of particle sizes and their chemical composition (Al, Si, Fe, Ti, non-sea-salt (nss) Ca, nssNa, and nssK) which scatter and absorb long-wave terrestrial radiation (Marconi et al., 2014; Tanré et al., 2003). The magnitude and the sign of dust RF strongly depend on a composition of particle mixture, but, generally, the mineral dust has a cooling effect. Depending on the season, dust may be mixed with biomass burning aerosols; it results in single scattering albedo that states the sign of the direct RF effect. An important role on dust radiative estimates also plays vertical distribution of particles (Sokolik et al., 2001). Because of their irregular shapes, the application of randomly oriented spheroids is usually used to describe dust particles (Mishchenko et al., 1997; Mishchenko, 2014; Veselovskii et al., 2010).

2.2 Basic radiometric quantities

Radiative energy transfer is the physical phenomenon of energy transfer in the form of electromagnetic radiation. This phenomenon is responsible for radiative transfer in the atmosphere. The analysis of a radiation field often requires the consideration of radiant energy within one elementary solid angle $d\Omega$. A differential solid angle is defined as a ratio of the differential area dS of a spherical surface intercepted to the square of the radius r : $d\Omega = dS/r^2 = \sin\theta' d\theta' d\varphi$, θ' and φ denote to zenith and azimuthal angles (see Fig. 2.2).

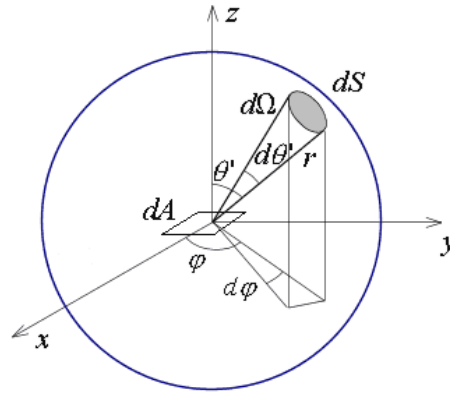


FIGURE 2.2: Illustration of a differential solid angle $d\Omega$. Also shown for demonstrative purpose an element of area dA in directions confined to an element of solid angle $d\Omega$.

Radiant flux (Φ_e) is defined by total radiant energy per unit time. It does not contain any information on spectral or directional distribution of radiation. Radiant flux is measured in the watts (W).

Spectral flux (Φ_λ) is radiant flux (Φ_e) per unit of wavelength (Fig. 2.3). Spectral flux is defined by the radiant energy within wavelength interval $(\lambda, \lambda + d\lambda)$ and the unit is $W\ nm^{-1}$. Radiant flux can be obtained through integration of spectral flux within all wavelengths:

$$\Phi_e = \int \Phi_\lambda(\lambda) d\lambda \quad (2.1)$$

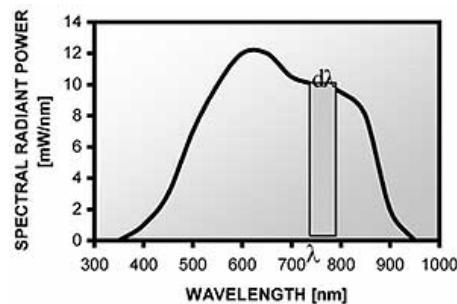


FIGURE 2.3: Relation between spectral radiant flux Φ_λ and radiant flux Φ_e , visualized at a hypothetical example. Radiant flux emitted in the wavelength interval $(\lambda, \lambda + d\lambda)$ is given by the area of the rectangle, which amounts to $\Phi_\lambda(\lambda)d\lambda$. The total amount of radiant flux Φ_e emitted over the whole spectrum is given by the area under the curve. Figure taken from <http://light-measurement.com/basic-radiometric-quantities/>.

Spectral intensity (I_λ) is spectral flux per unit solid angle ($d\Omega$), the unit of spectral intensity is $W\ sr^{-1}\ nm^{-1}$:

$$I_\lambda = \frac{d\Phi_\lambda}{d\Omega} \quad (2.2)$$

Hence, spectral flux can be defined regarding spectral intensity:

$$\Phi_\lambda = \int_{\Omega} I_\lambda d\Omega \quad (2.3)$$

Spectral radiance (L_λ) is spectral intensity which is passing through unit surface dA in direction confident to solid angle $d\Omega$ which is oriented to the normal of dA in an angle θ' (Fig. 2.2):

$$L_\lambda = \frac{dI_\lambda}{\cos(\theta')\ dA} \quad (2.4)$$

In terms of spectral flux, spectral radiance can be written as:

$$L_\lambda = \frac{d\Phi_\lambda}{\cos(\theta')\ dA\ d\Omega} \quad (2.5)$$

The unit of spectral radiance is $W\ m^{-2}\ sr^{-1}\ nm^{-1}$.

2.3 Light scattering and absorption by atmospheric molecules and aerosols

There are two processes (scattering and absorption) by which electromagnetic radiation interacts with atmospheric aerosol particles and molecules. As it was mentioned above, these two processes form direct aerosol effect on RF estimate in the Earth's atmosphere, and the net aerosol effect indicate negative influence.

As a result of absorption, the energy of incident light becomes part of the internal energy of particle/molecule. In case of molecules, absorption process is quantized

because it depends on rotational, vibrational or electronic energies of the molecule. Hence, we should have discrete absorption lines of atmosphere molecules, but there are number of effects which are shifting or broadening the line, such as thermal Doppler effect, pressure broadening effect and others. There are a variety of gases in Earth's atmosphere and, therefore, not all solar energy reach the Earth's surface. Solar spectrum on the top of the atmosphere and at sea level are presented in Fig. 2.4. The main molecular absorber are H_2O (water vapor), CO_2 , O_3 , N_2O , CO , O_2 , CH_4 , N_2 . Most of them absorb solar energy in near- and far-infrared wavelength regions as it shown in Fig. 2.4, except ozone which absorbs mainly in near-ultraviolet wavelengths.

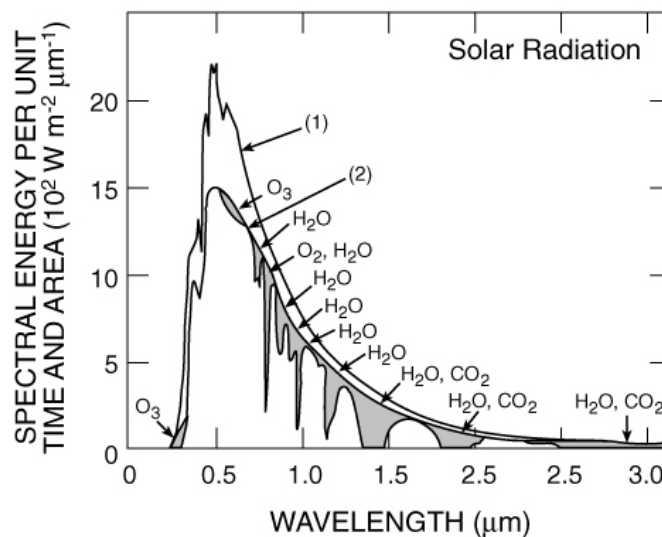


FIGURE 2.4: Solar spectrum on the top of atmosphere (1) and at the sea level (2). Absorption bands of various of gases are presented with identification of molecule; the shaded area correspond to the energy absorbed by various gases in a clear atmosphere. Figure is taken from Chapter 15 (Brasseur, Orlando, Tyndall, et al., 1999).

As a result of scattering, the incident light elastically or inelastically interacts with a particle/molecule. During this interaction, an energy of incident light is redistributed by scattering process. The term elastic scattering means that there is no difference between the wavelengths of the incident and scattered light. During the inelastic scattering some of the particle energy is lost or gained. It is, for example, the so called Raman scattering, by which rotational, vibrational and/or rotational-vibrational energy level of particle changes. For the Stokes Raman scattering, particle gains the energy

(absorbed energy is higher than emitted one), and for anti-Stokes Raman scattering, particle loses the energy (absorbed energy is lower than emitted one). Consequently, for Stokes and anti-Stokes Raman scattering incident photon loses and gains the energy respectively. Wave-number shift caused by inelastic scattering can be calculated as (Weitkamp, 2005).

$$\Delta\nu = \frac{\Delta E}{hc_0} \quad (2.6)$$

where ΔE is the difference between energy levels of the scattering molecule before and after the scattering, $\Delta\nu = 1/\lambda = \nu/c_0$ - wave-number of the scattered radiation, h and c_0 - Planck constant and speed of light, respectively. For LiDAR observations, Raman effect is widely used to obtain concentration profiles of specific molecules.

The process of scattering is highly depends on refractive index ($m = n + ik$) and size parameter (x), which characterized by the ratio of particle radius (r , particle length) and wavelength of incident light (λ), if particles are spherical:

$$x = 2\pi r/\lambda \quad (2.7)$$

Rayleigh theory is used if size parameter and real part of refractive index (n) meets the requirement $x < 0.6/n$. This theory is used to describe molecular scattering. Rayleigh theory is based on the assumption that all particles are spherical and their radii are much smaller than the wavelength of incident light. Rayleigh scattering coefficient depends on wavelength, and in general form like $\sim \lambda^{-4}$.

Mie theory is used when the size parameter and real part of the refractive index (n) satisfy the requirement $0.6/n < x < 5$. This theory is used when radii of particles are comparable with the wavelength of incident light. Scattered light has strong angular dependency, which is prominent in forward direction. Mie scattering is a more general theory and it converges into Rayleigh theory with size parameter decreasing. Rayleigh theory is much simpler in computational implementation. It should be noted, Mie theory is applied only to spherical particles.

Geometric optics approximation is used if size parameter is larger than 5 ($x > 5$). Such type of scattering is mainly a process of reflection and refraction. Geometrical optics is associated with "real" rays, but their analytic continuation to complex values of some associated parameters enables the concept of "complex rays" to be used, often in connection with surface or "evanescent" rays traveling along a boundary while penetrating the less dense medium in an exponentially damped manner (Adam, 2015).

Light scattering strongly depends on scattering angle θ . It is the angle between incident and scattered direction. In case of $\theta = 0^\circ$, scattered light propagates in the same direction as incident light (forward direction). In the event of $\theta = 180^\circ$, scattered light propagates in a backward direction. LiDARs measure the light which is backward scattered. Figure 2.5 shows differences between Rayleigh and Mie scattering. Rayleigh scattering is symmetric scattering in respect to a plane which is perpendicular to the direction of propagation, it finds its minimum at $\theta = \pm 90^\circ$ and maximums at $\theta = 0^\circ$ and $\theta = 180^\circ$. Mie scattering is an asymmetric scattering. In Fig. 2.5 are presented angular dependence of Rayleigh and Mie scattering, larger particles prefer to scatter in a forward direction.

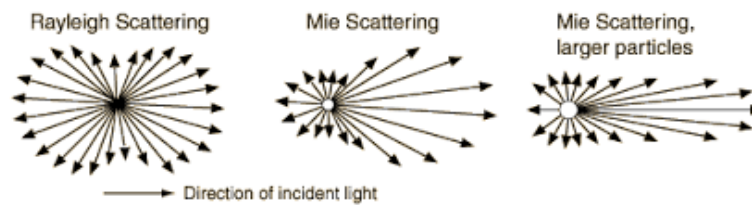


FIGURE 2.5: Rayleigh and Mie scattering. Also it is shown how Mie scattering changes with particle size. Figure is taken from: <http://hyperphysics.phy-astr.gsu.edu/hbase/atmos/blusky.html>

Hence, molecules and particles redistribute the electromagnetic energy that is propagating from the top of the atmosphere to the surface by scattering and absorption processes. Scattering (σ^{sca}) and absorption (σ^{abs}) cross section coefficients have been defined to quantify these processes. Together they form the extinction coefficient ($\sigma^{ext} = \sigma^{sca} + \sigma^{abs}$), which quantified the total attenuation of the atmosphere. Attenuation of the radiative energy can be represented as shown in Fig. 2.6 and defined as:

$$dI_\lambda = -I_\lambda \sigma_\lambda^{ext} ds \quad (2.8)$$

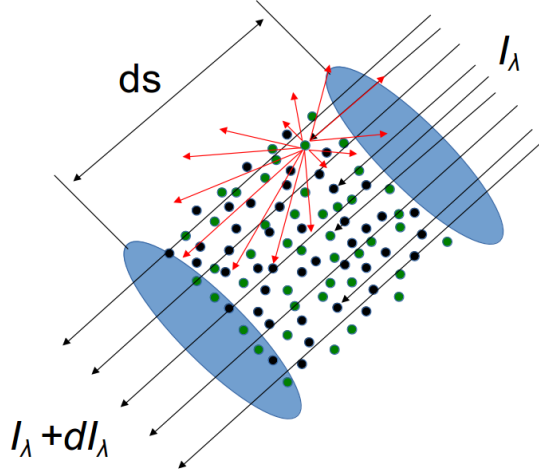


FIGURE 2.6: Schematic representation of attenuation of light propagating through the medium, black circles are particles or molecules which absorb radiative energy, green circles are particles and molecules which scatter radiative energy. Mie scattering on large particles are shown by red arrows.

Scattering and absorption coefficients of spherical particles distributed in size from r_1 to r_2 following $N(r)$ can be defined as:

$$\sigma_\lambda^{sca} = \int_{r_1}^{r_2} \pi r^2 Q_{sca}(r, \lambda, m) N(r) dr \quad (2.9)$$

$$\sigma_\lambda^{abs} = \int_{r_1}^{r_2} \pi r^2 Q_{abs}(r, \lambda, m) N(r) dr \quad (2.10)$$

where Q_{sca} and Q_{abs} are scattering and absorption efficiency factors of particle mixture, $N(r)$ is number size distribution of a particle mixture. As was mentioned above, a summation of coefficients gives extinction coefficient at specific wavelength. A full description of Rayleigh and Mie theories applied to atmospheric molecules could be found in Bohren and Huffman, 2008.

Except the size parameter x and refractive index m , scattering and absorption of atmospheric aerosols highly depend on particles shape. The optical properties of such

particles must be either computed using an advanced theory of electromagnetic scattering or measured experimentally. In this thesis, for the non-spherical particle properties retrieval, the method of T-matrix is used (Mishchenko et al., 1997). This method defines the single-scattering properties as a function of the volume size distribution of randomly oriented, polydisperse spheroids (Dubovik et al., 2002a).

More information about absorption and scattering non-spherical particles and different techniques used nowadays could be found in Mishchenko et al., 1997; Mishchenko, 2014; Dubovik et al., 2002a; Moosmüller, Chakrabarty, and Arnott, 2009; Lenoble, Remer, and Tanré, 2013; Babenko, Astafyeva, and Kuz'min, 2003.

2.4 Aerosol properties

To accurately compute radiative forcing, aerosol optical and microphysical properties should be known precisely. Description of the main aerosol properties is presented in this section.

2.4.1 Optical properties

Aerosol Optical Depth

Aerosol Optical Thickness (AOT) of the medium is defined as the integral of the extinction coefficient between two separated points (z'_1, z'_2) within the medium in the direction of the propagation of the radiation:

$$AOT_\lambda = \int_{z'_1}^{z'_2} \sigma^{ext}(z) dz' \quad (2.11)$$

Aerosol Optical Depth (AOD, τ^{ext}) is more general term, defined as aerosol optical thickness which is measured vertically (distance z between the planes in the parallel-plane medium), it can be written as:

$$\tau_\lambda^{ext}(z_1, z_2) = \int_{z_1}^{z_2} \sigma^{ext} dz = \int_0^{TOA} \sigma^{ext} dz \quad (2.12)$$

The relationship between AOT and AOD in Earth's atmosphere is:

$$AOT_{\lambda} = AOD_{\lambda} m_o \quad (2.13)$$

where m_o is the relative solar air mass, which is a function of solar zenith angle (θ'). Solar zenith angle is defined as an angle between the direction of the propagation of the radiation and zenith direction. If we assume parallel-plane atmosphere with refractive index equal one, we have:

$$m_o = \frac{1}{\cos(\theta')} \quad (2.14)$$

Other approximation should be used for the zenith angles higher than 80° (Kasten and Young, 1989).

Total atmospheric optical depth can be divided into optical depths of atmosphere constituents: molecules and aerosol particles. Hence, total OD can be written as:

$$\tau_{\lambda} = \tau_{mol,\lambda} + \tau_{aer,\lambda} \quad (2.15)$$

where $\tau_{mol,\lambda}$ and $\tau_{aer,\lambda}$ optical depths of molecules and aerosols for the given wavelength λ . At the same time, OD of the molecules can be separated according to different molecules, taking into consideration absorption and scattering processes of each constituent:

$$\tau_{mol,\lambda} = \tau_{H_2O,\lambda} + \tau_{NO_2,\lambda} + \tau_{O_3,\lambda} + \tau_{CO_2,\lambda} + \dots \quad (2.16)$$

where $\tau_{H_2O,\lambda}$, $\tau_{NO_2,\lambda}$, $\tau_{O_3,\lambda}$, $\tau_{CO_2,\lambda}$ correspond to water vapor, nitrogen dioxide, ozone and carbon dioxide optical depths. The OD of other constituents are usually neglect due to their very small concentration in atmosphere.

Aerosol optical depth can also be divided into several AODs regarding aerosol types or fractions, but because of a complexity of aerosol mixtures by which atmosphere is characterized it is commonly defines to a full aerosol mixture in the atmosphere

column. The spectral dependence of the AOD can be parametrized by means of Angstrom law (Ångström, 1964):

$$\tau_\lambda = \tau_{1\mu m} \lambda^{-\alpha} \quad (2.17)$$

where $\tau_{1\mu m}$ and α are the aerosol optical depth at $1\mu m$ and Angstrom exponent. The α characterizes AOD spectral dependence, and it is related to the size of particles. High value of α indicates a predominance of fine particles (anthropogenic pollution, biomass burning, etc.), and the low value of α indicates a predominance of coarse particles (dust and sea salt).

Single Scattering Albedo

Single scattering albedo ($\omega_0(\lambda)$) is the ratio of scattering efficiency to total extinction efficiency. It indicates the dominant process (scattering or absorption) in the atmosphere and can be written:

$$\omega_0(\lambda) = \frac{\sigma_\lambda^{sca}}{\sigma_\lambda^{ext}} = \frac{\sigma_\lambda^{sca}}{\sigma_\lambda^{abs} + \sigma_\lambda^{sca}} \quad (2.18)$$

This parameter shows how much radiative power is scattered over total extinction. Absorption of solar radiation by atmospheric aerosols mainly results from elemental carbon originated from biomass burning and fuel combustion, that absorbs in visible spectrum, and from the hematite in a mineral dust, that absorbs in the ultraviolet range.

Phase matrix and scattering phase function

One of the possible formulations commonly referred as Stokes parameters $\tilde{\mathbf{I}}$ (Hulst and Van De Hulst, 1957):

$$\tilde{\mathbf{I}} = \begin{pmatrix} I \\ Q \\ U \\ V \end{pmatrix} \quad (2.19)$$

The Stokes vector element I is the radiant intensity, Q and U are the vector elements which describe the magnitude and direction of linearly polarized intensity, V component describes the circular polarization.

The angular distribution of the scattered electromagnetic wave in the far field, where the distance between the scattering particle and the observation location is much larger than the wavelength, is characterized by the phase matrix $\tilde{\mathbf{P}}(\theta)$. The phase matrix specifies the directionality of the scattering, it allows to perform the transformation from the incident Stokes vector $\tilde{\mathbf{I}}_i$ to the scattered vector $\tilde{\mathbf{I}}_s$:

$$\tilde{\mathbf{I}}_s \propto \tilde{\mathbf{P}}(\theta) \tilde{\mathbf{I}}_i \quad (2.20)$$

$$\begin{pmatrix} I_s \\ Q_s \\ U_s \\ V_s \end{pmatrix} = \frac{\sigma_{sca}}{4 \pi r^2} \begin{pmatrix} P_{11} & P_{12} & P_{13} & P_{14} \\ P_{21} & P_{22} & P_{23} & P_{24} \\ P_{31} & P_{32} & P_{33} & P_{34} \\ P_{41} & P_{42} & P_{43} & P_{44} \end{pmatrix} \begin{pmatrix} I_i \\ Q_i \\ U_i \\ V_i \end{pmatrix} \quad (2.21)$$

where θ is the scattering angle, σ_{sca} is the scattering cross-section for unpolarized incident light and r is the distance from the scattering particles. The first element of the phase matrix, $P_{11}(\theta, \lambda)$, is called the scattering phase function. It describes the angular distribution of scattered intensity for incident unpolarized light. Angular distribution is defined by the angle θ between incident and scattered radiation, representation is shown in Fig. 2.7.

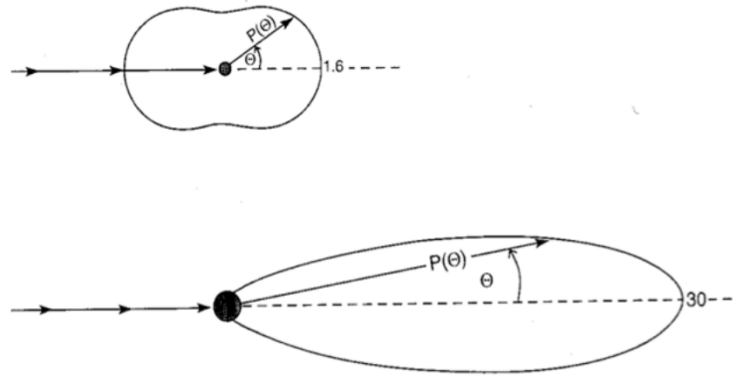


FIGURE 2.7: Representation of scattering phase function of the Rayleigh (top) and Mie (bottom) scattering (see Fig. 2.5).

LiDAR and depolarization ratios

The LiDAR community often use extinction to backscatter ratio, also called LiDAR ratio, as defined:

$$LR(\lambda, z) = \frac{\sigma^{ext}(\lambda, z)}{\beta(\lambda, z)} \quad (2.22)$$

Backscatter coefficient can be defined from scattering phase function in 180° and σ^{sca} :

$$\beta(\lambda, z) = \frac{\sigma^{sca} P_{11}(180^\circ, \lambda)}{4\pi} \quad (2.23)$$

$$LR(\lambda, z) = \frac{4\pi}{\omega_0(\lambda) P_{11}(180^\circ, \lambda)} \quad (2.24)$$

The LR is given in *sr*. This parameter is very useful for aerosol type identification (Amiridis et al., 2011; Josset et al., 2011). Typical LR obtained by LiDAR measurements can be found in Table 4.1.

Commonly, LiDAR emits linearly polarized light. Non-spherical particles change the polarization of light during the scattering process. Thus, polarization sensitive measurements are connected to the amount and shape of non-spherical particles in the atmosphere. The increase of the "contrast" between the parallel and perpendicular

components of the backscattered light indicate increase of amount of non-spherical particles. This contrast is called depolarization ratio:

$$\delta(\lambda) = \frac{P_{11}(180^\circ, \lambda) - P_{22}(180^\circ, \lambda)}{P_{11}(180^\circ, \lambda) + P_{22}(180^\circ, \lambda)} \quad (2.25)$$

As LiDAR ratio, the depolarization ratio (δ) helps to identify aerosol type as well. For example, typical depolarization ratio for mineral dust is in range between 30-35% (Müller et al., 2007; Müller et al., 2010), while marine particle δ is close to 5% (Groß et al., 2011). More information about depolarization ratio presented in Chapter 2.6.3.

2.4.2 Microphysical properties

Because of large size ranges (particle sizes are in range from 0.001 to 100 μm in radius) it is useful to represent distribution in the logarithmical scale, which will be used. Size distribution can be described regarding number, surface and volume size distributions. The former represents the number of particles within specific radii [$\ln(r), \ln(r) + d\ln(r)$]:

$$N(r) = \frac{dN}{d\ln(r)} \quad (2.26)$$

The surface size distribution represents the surface of particles per unity of volume for particles within specific radii, can be defined as:

$$S(r) = \frac{dS}{d\ln(r)} = \frac{4\pi r^2 dN}{d\ln(r)} = 4\pi r^2 N(r) \quad (2.27)$$

Volume size distribution represents aerosol volume in column of unity cross section, it can be defined similarly to previous:

$$V(r) = \frac{dV}{d\ln(r)} = \frac{\frac{4\pi r^3}{3} dN}{d\ln(r)} = \frac{4\pi r^3 N(r)}{3} \quad (2.28)$$

Total number, surface and volume of particles are obtained by integration within all radii:

$$\begin{aligned}
N &= \int_0^{\infty} N(r) d\ln(r) \\
S &= \int_0^{\infty} S(r) d\ln(r) \\
V &= \int_0^{\infty} V(r) d\ln(r)
\end{aligned} \tag{2.29}$$

The column integrated number and volume size distributions are defined by integrating the vertically resolved number and volume particle concentrations. This parameters can be expressed as:

$$\begin{aligned}
N_{column}(r) &= \int_0^{\infty} N(r, z) dz \\
V_{column}(r) &= \int_0^{\infty} V(r, z) dz = \frac{4\pi r^3}{3} N_{column}(r)
\end{aligned} \tag{2.30}$$

As it was mentioned previously, size distribution is one of the properties which defines total AOD, it can be written similarly to Eq. 2.9-2.10:

$$\tau_{\lambda} = \int_{r_1}^{r_2} \pi r^2 Q^{ext}(r, \lambda, m) N_{column}(r) dr \tag{2.31}$$

Commonly, particle size distribution is reproduced by several log-normal distributions (Heintzenberg, 1994), such mathematical representation can be used in inversion algorithms which retrieve aerosol optical and microphysical properties.

Effective radius defines from number size distributions (Eq. 2.32) and can be used as an indicator of particle type, typical effective radii of main aerosol types were presented in Table 2.1. Effective radius defines as:

$$r_{eff} = \frac{\int_0^{\infty} r (r^2 N_{column}(r)) dr}{\int_0^{\infty} (r^2 N_{column}(r)) dr} \tag{2.32}$$

2.5 Water vapor, mixing ratio and relative humidity

Water vapor is one of the most important constituents in the Earth's atmosphere due to its high spatial and temporal variability and its involvement in many atmospheric processes (e.g. formation and development of clouds, affecting on the size, shape and chemical composition of aerosol particles (Reichardt et al., 1996). Hence, it plays a key role in the global radiation budget and in energy transport mechanisms in the atmosphere (Whiteman, Melfi, and Ferrare, 1992; Ferrare et al., 1995). Hence, low uncertainties in both observations and modeling of water vapor are needed for the accurate representation of clouds and precipitation in climate models and predictions.

To achieve a comprehensive understanding of the role of water vapor on local and global scales, systematic and highly accurate observations with high spatial and temporal resolution are required. Among the in situ techniques, radiosonde is extensively used due to its high spatial resolution, but the temporal resolution depends on the launch frequency. There are additional disadvantages: it is an expensive technique, the verticality of the sounding depends on the wind regime and its changes with altitude (balloons drift with the wind), and it is difficult to make accurate water vapor measurements in conditions of low relative humidity.

Several methods and techniques can help to obtain the water vapor in the column of atmosphere, including sun/sky-photometer and direct radiosonde measurements, LiDAR and GPS observations, etc. (Schläpfer et al., 1998; Gao and Goetz, 1990; Schmid et al., 1996; Rocken et al., 1995; Ferrare et al., 1995). Satellite observations, such as MODIS (<http://modis-atmos.gsfc.nasa.gov/index.html>), takes advantage in case of global coverage of water vapor content. Total Precipitable Water, given in $g\ cm^{-2}$, in the atmosphere column can be found as (Lenoble, 1993):

$$TPW = \int \rho_{H_2O}(z) dz \quad (2.33)$$

$$TPW = -\frac{1}{g} \int_{p_0}^0 q(p) dp \quad (2.34)$$

where $\rho_{H_2O}(z)$ is water vapor density, and $q(p) = w(p)/(1 + w(p))$ is specific humidity, g - is standard acceleration of free fall, $w(p)$ is water vapor mixing ratio, which determines as the ratio between the density of water vapor to the density of dry air:

$$w(z) = \frac{\rho_{H_2O}(z)}{\rho_{air}(z)} \sim \frac{N_{H_2O}(z)}{N_{N_2}(z)} \quad (2.35)$$

Water vapor mixing ratio is also proportional to the ratio of the molecular number densities of water vapor and nitrogen. Thus, it can be directly measured with Raman LiDAR, as it will be shown in (Chapter 2.6.3).

Relative humidity, RH, is the ratio of the water vapor partial pressure, $e(z)$, to the saturation vapor pressure, $e_w(z)$, Eq. 2.36. It depends on temperature and pressure of the atmosphere and can be highly variable with altitude.

$$RH = \frac{e(z)}{e_w(z)} 100\% \quad (2.36)$$

$$e(z) = \frac{p(z) w(z)}{0.622 + w(z)} \quad (2.37)$$

$$e_w(z) = 6.107 \exp\left(\frac{M_A [T(z) - 273]}{M_B + [T(z) - 273]}\right) \quad (2.38)$$

where $M_A=17.84$ (17.08) and $M_B=245.4$ (234.2) for T below (above) 273 K (Navas-Guzmán et al., 2014). Hence, for accurate profiling of RH, $p(z)$ and $T(z)$ are needed. Uncertainties of temperature profile (Navas-Guzmán et al., 2014; Foth et al., 2015) cause main errors in obtaining RH, hence, preferably to use accurately measured $T(z)$ instead of modeled one.

The significance of water vapor and relative humidity investigation is very high due to its influence on aerosol particles (coating, CCN) (Hänel, 1976; Charlson et al., 1992; Muñoz, 2014). It changes the aerosol properties, and, therefore, influence on the radiative forcing estimation. Because water vapor is highly variable spatially and temporally in the atmosphere, it is highly preferable to have the continuous measurements

of its vertically distribution.

2.6 LiDAR principle, equation and types

2.6.1 LiDAR principle

LiDAR (Light Detection And Ranging) follows the same principle as RADARs (Radio Detection And Ranging), but it uses radiation with the wavelengths in ultraviolet, visible, near and middle infrared ranges instead of radiation in radio range used in RADARs (Pelon et al., 2013). The principle of instruments consists in emitting of electromagnetic radiation in particular wavelength and measuring the radiation which is backscattered to instrument telescope from some targets. Aerosols are targets for LiDAR observations (Amiridis et al., 2005).

All LiDAR systems consist of transmitter and receiver; the basic setup is presented in Fig. 2.8. The transmitter consists of LASER, which is emitting short light pulses with duration from a few to several hundred nanoseconds with specific spectral properties, and the beam expander, which corrects the divergence and collimates the beam of light. The receiver consists of telescope that collects backscattered light, detectors which measure light irradiance, and data acquisition system which gathers and records the measurements. Depending on LiDAR type, light can be emitted at different wavelengths, and, therefore, different detectors are needed to measure backscattered light.

2.6.2 LiDAR equation

In the simplest form, LiDAR equation can be written:

$$P(R) = K G(R) \beta(R) T(R) + P_{bg} \quad (2.39)$$

where $P(R)$ - a radiative power of backscattered radiation which has been received from a distance R ; P_{bg} - a power of background radiation; K - a factor which describes

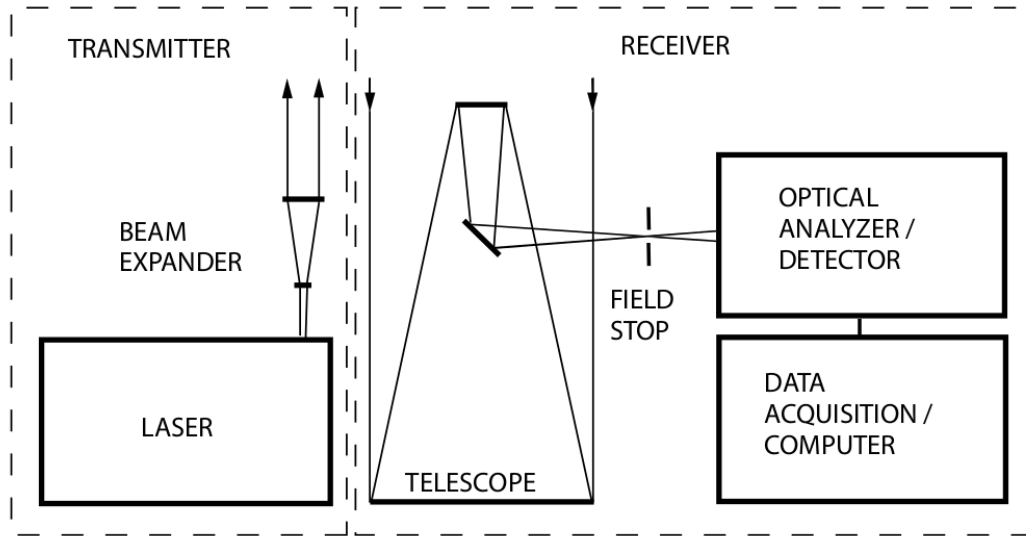


FIGURE 2.8: Standard LiDAR setup, figure taken from (Weitkamp, 2005)

the LiDAR performance; $G(R)$ - a factor which describes the range depending measurement geometry; $\beta(R)$ - backscattered coefficient as a function of distance R ; $T(R)$ - the atmospheric transmission, it describes how much of radiation have been lost on the way to target and back. Both, K and $G(R)$ are the factors which depend on LiDAR system, latter two ($\beta(R)$ and $T(R)$) are unknowns and should be investigated from the measurements.

Detected LiDAR signal always has a contribution from background radiation (P_{bg}). Background noise can be easily subtracted from LiDAR signal by averaging in very far altitude range, where no backscattered photons are expected anymore, or in the range of trigger delay when the laser does not start to emit light yet but system is already started to measure. It should be mentioned, such LiDAR measurements can be considered as a passive remote sensing measurements. The processes which underlie of LiDAR background radiation and sun/sky-photometer measurements are the same, particles and molecules absorb and scatter solar light, that is why background noise is high during the day-time measurements and it is very low (negligible) during the night-time measurements. Hence, if a LiDAR can provide measurements in almucantar or principle plane geometry, it would bring active (LiDAR backscatter signal) and passive (LiDAR background noise) measurements which can complement each other. But in practice, such experiment is complicated because of weight and complexity of

the LiDAR systems.

The system factor K can be written as:

$$K = P_0 \frac{c \Delta\tau}{2} A \eta \quad (2.40)$$

where P_0 - power of a laser pulse; $\Delta\tau$ - temporal pulse duration, $c \Delta\tau/2$ - is the length of the volume from which backscattered light is received at an instant time (shown in Fig. 2.9 as ΔR , effective pulse length); A - area of telescope which receives backscattered light; η - system efficiency which includes efficiencies of light transmittance by all optical elements of the system and the detection efficiency of the receivers.

The geometric factor is related to Overlap function and R^2 :

$$G(R) = \frac{O(R)}{R^2} \quad (2.41)$$

Overlap function is a characteristic of LASER beam divergence and receivers' field of view. It increases from zero at the telescope to unity in the distance where the backscattered laser light is completely imaged onto the detector through the telescope field of view and all further system elements. The quadratic decrease ($1/R^2$) of the backscattered signal intensity caused by a fact that telescope area is the part of sphere's surface with radius R which encloses target (scattering volume V in Fig. 2.9).

The backscattered coefficient $\beta(R, \lambda)$ is the atmospheric parameter, which determines how much of the light is scattered in a backward direction by atmospheric constituents. It directly depends on size, refractive index, shape and, of course, backscatter coefficient depends on wavelength. The backscatter coefficient can be expressed through the concentration of particles (N_j , j is particle type, molecules/aerosols) in the scattering volume and differential scattering cross section ($d\sigma_j^{sca,cs}(\pi, \lambda) / d\Omega$) of the particle type j in the backward direction at wavelength λ :

$$\beta(R, \lambda) = \sum_j N_j(R) \frac{d\sigma_j^{sca,cs}}{d\Omega}(\pi, \lambda) \quad (2.42)$$

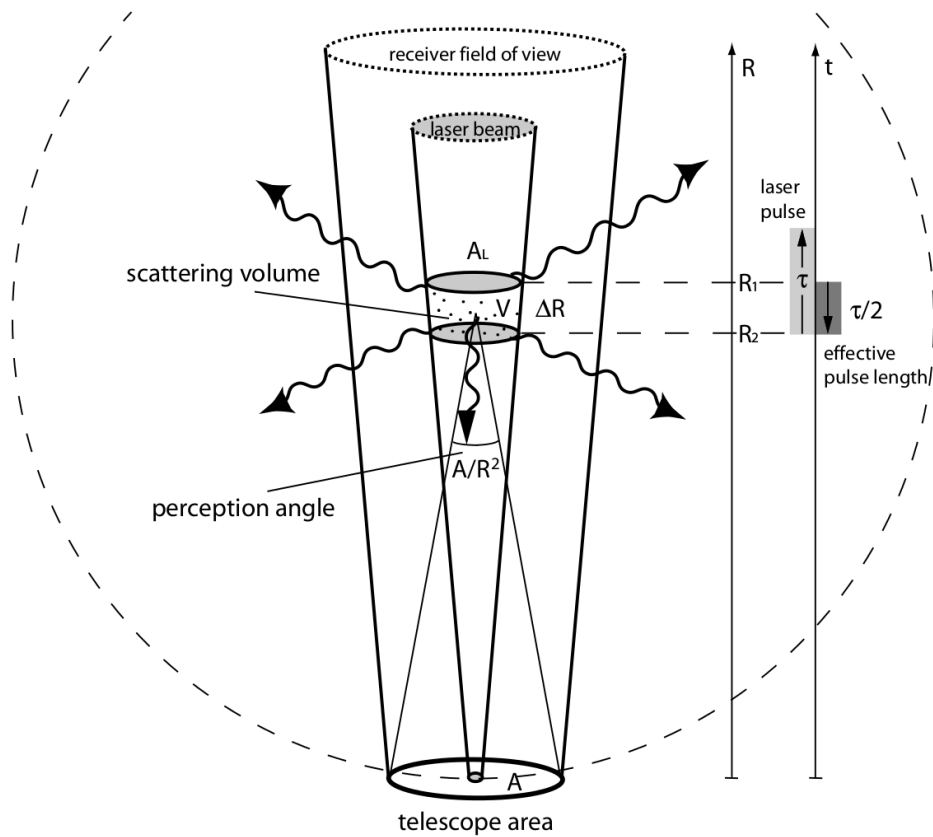


FIGURE 2.9: Illustration of LiDAR geometry, taken from (Weitkamp, 2005).

Since the number concentration is given in m^{-3} and the differential scattering cross section in $m^2 sr^{-1}$, the backscatter coefficient unit is $m^{-1} sr^{-1}$. As it was described previously, it is useful to distinguish coefficient attributed to molecules and aerosol components at the total backscattered coefficient:

$$\beta = \beta_m + \beta_a \quad (2.43)$$

Molecular/gas scattering can be calculated from meteorological data using Rayleigh theory, e.g. model of US standard atmosphere can be used (Krueger and Minzner, 1976). It is possible to calculate molecular backscatter profile using modeled temperature and pressure atmospheric profiles.

The transmission term $T(R, \lambda)$ describes a fraction of laser power which is lost during the way to target and back to the telescope. It can be written as:

$$T(R, \lambda) = \exp \left[-2 \int_0^R \sigma^{ext}(r, \lambda) dr \right] \quad (2.44)$$

This term results from the specific form of the Lambert-Beer-Bouguer law for LiDAR (Weitkamp, 2005). The transmission term considers the path of light from the LiDAR to distance R and back, factor 2 before the total optical depth appears because of that. Extinction coefficient can be presented in the form, similarly to backscatter coefficient:

$$\sigma_{ext}(R, \lambda) = \sum_j N_j(R) \sigma_j^{ext,cs}(\lambda) \quad (2.45)$$

The extinction coefficient includes terms resulted from scattering and absorption of molecules and aerosol particles and can be written as:

$$\sigma_{ext} = \sigma_m^{abs} + \sigma_m^{sca} + \sigma_a^{abs} + \sigma_a^{sca} \quad (2.46)$$

LiDAR wavelengths are selected so as to minimize molecular absorption. Molecular scattering can be defined from the atmospheric models. Aerosol absorption and scattering, which form aerosol extinction, are unknown and to be retrieved later.

Summarizing, the LiDAR equation, in general form, can be written as:

$$P(R, \lambda) = P_o \frac{c \Delta \tau}{2} A \eta \frac{O(R)}{R^2} \beta(R, \lambda) \exp \left[-2 \int_0^R \sigma^{ext}(r, \lambda) dr \right] \quad (2.47)$$

2.6.3 LiDARs types

There are six basic types of LiDAR systems. They correspond to different techniques which use specific interaction processes of the emitted radiation with the atmospheric constituents:

- Elastically backscatter LiDAR;
- Raman LiDAR (non-elastic);
- Differential-absorption LiDAR;

- Fluorescence (resonance) LiDAR;
- Doppler LiDAR;
- High spectral resolution LiDAR (HSRL).

Differential-absorption LiDAR (DIAL) makes use of single absorption lines or broad absorption bands of gases. Such LiDARs are emitting radiation at two wavelengths, one is absorbed by specific molecules more strongly than the other one. Differential molecular absorption coefficients infer the number concentration (see Eq. 2.45). Hence, molecular concentration can be found by the use of Eq. 2.45, if the differential absorption cross section for this molecule is known.

A resonance fluorescence is obtained if the energy of the incoming photon coincides with the energy of a transition in an atom, ion, or molecule from one level to another. That is why resonance fluorescence LiDAR works well with specific metallic atoms and ions. Because of very high scattering cross section, this technique works with very low number concentrations and can be used in altitudes higher 100km.

Doppler LiDAR is mainly used to determine the wind direction and its speed. It is based on Doppler effect which causes the wavelength shift of backscattered light. If the targets move toward to propagation of radiation, it will be shifted to lower wavelength, and vice versa. Such LiDAR has been operated during SHADOW-2 campaign in Dakar in 2015 and 2016 (Windcube).

HSRL LiDAR relies on the differences in the spectral distribution of light elastically backscattered by particles and air molecules. The spectral width of Rayleigh-backscattered photons is increased due to Doppler shifts caused by the thermal motion of the molecules. The thermal motion of aerosol and cloud particles is much slower, so their backscatter spectrum remains nearly unchanged. Here, the molecular backscatter channel measures Rayleigh backscattering by blocking the narrow aerosol peak, e.g., by use of an atomic-vapor filter. A second channel may detect the total backscatter or just the central aerosol peak (Bruneau et al., 2015).

Elastic backscatter LiDAR and depolarization

Elastic backscattered LiDAR is the classic form of LiDARs. Its principle has been fully described previously in this section. Elastic scattering is a process in which wavelength of the scattered radiation remains unchanged. This type of LiDAR delivers information on the presence and location of aerosol and cloud layers. If Eq. 2.43 and Eq. 2.46 substitute into Eq. 2.47, LiDAR equation will have two unknowns, aerosol extinction and backscattering coefficients. Hence, different methods are used to derive aerosol extinction and backscatter coefficients; some will be presented in Chapter 4.

In the atmosphere, there are particles with high variability of shapes (see Fig. 2.1). The actual shape does not play a major role for the scattering properties of small particles with size parameter $x < 1$, in such cases Mie theory can be applied (Lenoble, Remer, and Tanré, 2013). But if the particles are large and non-spherical, like ice crystals, mineral dust, or sea-salt particles, Mie scattering theory can not be used anymore. More complex model, like a model of randomly oriented polydisperse spheroids, should be used. One of the features of non-spherical particles consists of their property to depolarize the backscatter radiation (spherical particles do not change linearly polarized laser light). Hence, polarization-sensitive light detection is particularly relevant for the investigation of non-spherical particles.

Volume depolarization ratio term (δ) comes from taking the ratio of the LiDAR equation (Eq. 2.47) to itself in the two polarization planes (\parallel and \perp to laser emission polarization). Most of the terms are canceled out and depolarization ratio can be written as:

$$\delta(R) = \frac{\beta_{\perp}(R)}{\beta_{\parallel}(R)} \exp(\tau_{\perp} - \tau_{\parallel}) \approx \frac{\beta_{\perp}}{\beta_{\parallel}} \quad (2.48)$$

where β and τ are the backscatter coefficients and optical depths in the planes of polarization orthogonal (\perp) and parallel (\parallel) to that of the laser. In practice, the exponential term is not used because $\beta_{\perp} \ll \beta_{\parallel}$ which gives $\exp(\tau_{\perp} - \tau_{\parallel}) \approx 1$. But it was originally included to account for the possibility that certain anisotropic targets like uniformly

oriented ice crystals or raindrops could affect the transmission of light depending on the polarization state.

It should be reminded, depolarization ratio can be also expressed with Phase matrix element P_{11} and P_{22} , Eq. 2.25.

Satellite mission CALIPSO (Cloud-Aerosol Lidar and Infrared Pathfinder Satellite Observations, Pelon et al., 2011) is using elastic backscatter LiDAR, called CALIOP (Cloud-Aerosol Lidar with Orthogonal Polarization). CALIOP is the primary instrument on the CALIPSO satellite (Winker, Pelon, and McCormick, 2003; Winker et al., 2010). CALIOP is designed to acquire vertical profiles of elastic backscatter at 532 and 1064 nm wavelengths from a near nadir-viewing geometry during both day and night phases of the orbit. In addition to the total backscatter at the two wavelengths, CALIOP also provides profiles of linear depolarization at 532 nm.

Inelastic or Raman LiDAR

Inelastic scattering process which involves the change of the vibrational-rotational energy level of the molecule is called Raman scattering (has been presented in Section 2.3). Because of the wavelength shift caused by Raman scattering and different transmittance of the atmosphere in new scattered wavelength, LiDAR equation is changed (term of background noise is excluded):

$$P_{Ra}(R) = \frac{K O(R)}{R^2} \beta_{Ra}(R) \exp \left[- \int_0^R [\sigma_{Li}(r) + \sigma_{Ra}(r)] dr \right] \quad (2.49)$$

where K and $O(R)$ - are system factor and overlap function which were described above, $\beta_{Ra}(R)$ is the Raman backscatter coefficient at the distance R , $\sigma_{Li}(R)$ and $\sigma_{Ra}(R)$ describe extinction of atmosphere at the emitted LiDAR and backscattered Raman wavelengths. Raman LiDARs usually assembled with an elastic channels. Hence, observations of such LiDAR system can be described with two equations Eq. 2.47 and Eq. 2.49. Description of Raman method will be presented in Chapter 4.

Raman LiDARs are widely used in atmospheric studies. The temperature dependence of the rotational Raman bands of major atmospheric molecules permits to determine atmospheric temperature profile from the ground up to about 40 km height (Weitkamp, 2005). Because of low Raman scattering cross section of gas molecules this technique requires high concentration of the investigated atmospheric component. Nitrogen, oxygen, and water vapor are the major gases constituencies in the atmosphere which are widely used in atmospheric studies. If, for instance, LiDAR system have two Raman nitrogen and/or oxygen signals, one of which is partly absorbed by ozone, it is possible to determine ozone concentrations (Reichardt et al., 1996; Reichardt et al., 2000).

Opposite to oxygen and nitrogen gases, the amount of the water vapor concentration is highly variable temporally and spatially. Thus, observations of Raman LiDAR are widely used to investigate water vapor profiles (Whiteman, Melfi, and Ferrare, 1992; Weitkamp, 2005). As it was shown, water vapor mixing ratio is proportional to number concentration of nitrogen and water vapor (Eq. 2.35). Thus, ratio of two LiDAR Raman signals, one of which corresponds to water vapor and another one to nitrogen molecules, forms water vapor mixing ratio:

$$w(z) \sim \frac{P_{Ra}^{H_2O}(z)}{P_{Ra}^{N_2}(z)} \quad (2.50)$$

2.7 From optical to microphysical aerosol properties: inverse methods

Ground-based measurements of diffuse and direct solar radiation (sun/sky-photometer) have been used to retrieve the size distribution and refractive index of aerosol particles in the atmosphere as well as their optical properties (Dubovik and King, 2000). Look-up tables which contain theoretical solutions of aerosol parameters can be used. For instance, simulated measurements obtained from theoretical calculations are compared with actual measurements and special procedure searching for the best fit between measurements and simulated data. The look-up table solution is stable and

generally fast in implementation, though it is limited to a set of potentially admissible solutions included in the look-up table. This approach was and still use for satellite data inversion because there are a lot of data and time of processing is important.

Rigorous but more complex techniques have also been invoked that consist of "inverting" a set of measurements as a function of wavelength and/or scattering angle to infer the size distribution, refractive index and optical properties (Lenoble, Remer, and Tanré, 2013). These methods are not limited by the predefined set of aerosol classes such as look-up table method. Such techniques use iteration procedure which uses a priori data (aerosol parameters), and each step of iteration procedure defines aerosol parameters more accurately. There are several steps in an iteration procedure: (i) on the first step algorithm defines radiation distribution using theoretical calculation (forward model); (ii) on the second step obtained radiation distribution are compared with actual measurements and difference between modeled and actual measurements are defined; (iii) aerosol parameters are defined more accurately and iteration procedure repeats or algorithm stops if a difference between modeled and actual measurements are within the predefined constraints.

In such methods, several different combinations of aerosol parameters can produce the same or nearly the same radiation distribution. Therefore, the general solution is fundamentally non-unique or becomes non-unique in the presence of minor measurement noise. That is why to decrease the number of solutions, a priori information is necessary and added. Inversion with regularization (Müller, Wandinger, and Ansmann, 1999; Veselovskii et al., 2002; Veselovskii et al., 2004) and GRASP/GARRLiC algorithm (Dubovik et al., 2011; Dubovik et al., 2014; Lopatin et al., 2013) belong to such methods and will be considered in this work.

Chapter 3

Experimental sites, instrumentation and modelling tools

This chapter describes experimental sites where the measurements were carried out, instrumentation, data and modeling tools which were used through the thesis.

3.1 Lille and Dakar super-sites

Laboratoire d'Optique Atmosphérique leads, for more than 20 years, two observational sites. One located on the roof of the laboratory at Villeneuve d'Ascq, South of Lille city, France. The second one is located in M'Bour city, Senegal. Measurements from both sites are considered in this thesis.

Lille site (50.61°N , 3.14°E , 60 m a.s.l.) is influenced by urban and industrial pollutions, marine aerosols. Several times per year the sky over the site is affected by mineral dust and more rarely by aerosols from volcano eruptions (Mortier et al., 2013; Boichu et al., 2015). Site is based in 100 km from Northern sea coast. Dakar site (14.39°N , 16.96°W , 0 m a.s.l.), which is located in M'Bour city, is usually influenced by dust during March–April period and biomass burning during December–January (Kaufman, Tanré, and Boucher, 2002). The site is placed on the coast of Atlantic ocean and, therefore, influenced by maritime aerosols.

Both sites have remote sensing and in situ instruments. They are equipped with lunar-photometers, which provide AOD, AE and TPW for all clear nights for lunar phase, from half to full moon.

A new multi-wavelengths Raman-polarized LiDAR system, called LILAS (Lille LiDAR AtmosphereS), used in the thesis has been purchased in the framework of the CaPPA (Chemical and Physical Properties of the Atmosphere) and IRENI (Institut de recherche en environnement industriel) projects. The major objective of CaPPA project focus on the comprehensive study of the aerosol system and its precursors, allowing a better understanding of their role on the climate: radiative forcing and hydrological cycle. Additionally, CaPPA investigates the evolution of air quality at local, regional and global levels with specific concerns for radionuclides. Lille site is a permanent site for LiDAR observation (<http://www-loa.univ-lille1.fr/index.php/observation/lidar.html>). However, in the framework of CaPPA project a field campaign has been organized in West Africa (SHADOW-2 – study of Saharan dust over the West Africa). Many instruments, including this new LiDAR, have been moved to Dakar site at the beginning of January 2015. Two main objectives of this campaign are: (i) better records of the physical and chemical aerosol properties over the region impacted by considerable amount of dust particles; (ii) study the aerosol dynamic. Seven laboratories with 18 instruments were taking part in the campaign (<http://www.labex-cappa.fr/en/SHADOW>).

3.2 LILAS system

The LiDAR operated in this work is called LILAS (Fig. 3.1 and 3.2) and located at Laboratoire d'Optique Atmosphérique (Lille site). LILAS was assembled and setup in December 2013 in the framework of a French–Russian cooperation (PICS, I. Veselovkii) and first observations started in Lille in January 2014. The system is composed of a laser (Spectra-physics, INDI-40) emitting 1064 nm, 532 nm and 355 nm (100mJ/20Hz), of a Newton telescope, a beam rotator and receiving module (Fig. 3.3). Beam rotator can be used for near or far altitude observations by changing the overlap function. In April 2014, several receiving modules were added. Since mid of 2014, LILAS system

includes five elastic channels (355 nm and 532 nm parallel and perpendicular, analog and photo-counting and 1064 nm total analog) and three Raman channels (387 nm analog and photo-counting, 408 nm and 608 nm photo-counting). At the beginning of 2015, vibrational Raman channel at 608 nm has been changed to rotational Raman channel at 530 nm. This rotational Raman channel shows good and stable performance. The system can be remotely operated and it is coupled with a RADAR for automatic stop for airplane safety.

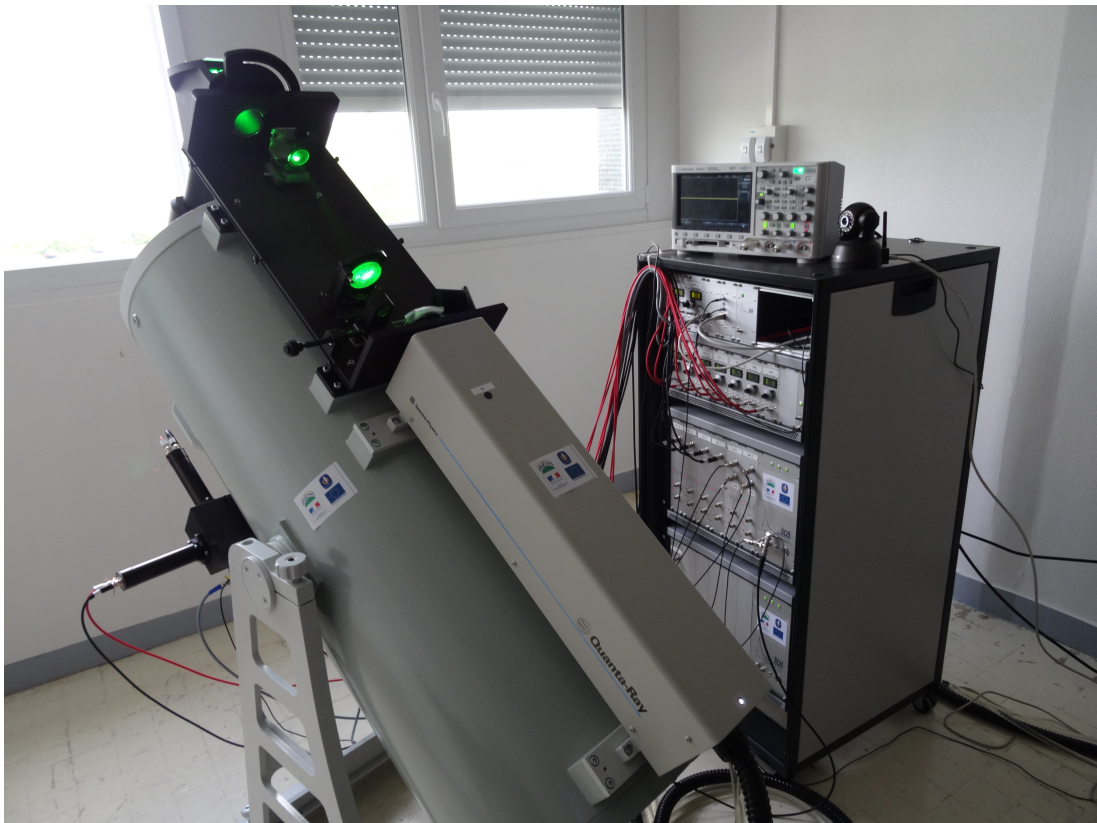


FIGURE 3.1: LILAS system. Newton telescope, Quanta-Ray laser, beam expander and acquisition system (Courtesy LOA, 2014).

3.2.1 LILAS Quality Assurance Procedures

In summer 2014, LILAS was included as a new station in the European Aerosol Research LiDAR Network (EARLINET). The main goal of EARLINET/ACTRIS (Aerosols, Clouds, and Trace gases Research InfraStructure Network, <http://www.actris.eu/>) is to provide a comprehensive, quantitative and statistically significant database about aerosols vertical distribution. The network has special criteria for data quality assurance (Freudenthaler, 2007; Freudenthaler et al., 2007; Freudenthaler, 2010;

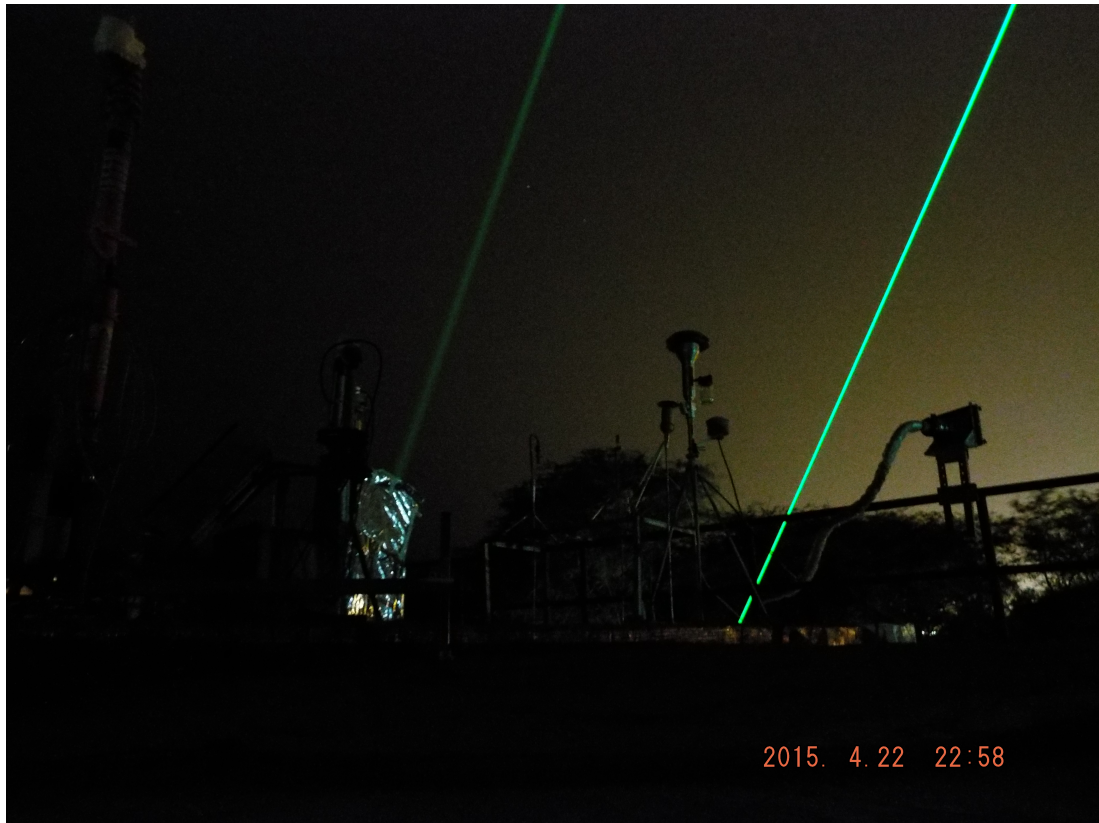


FIGURE 3.2: LILAS beam (more intense) and CAML beam (less intense, Cloud and Aerosol Micro-LiDAR, CIMEL) during the SHADOW-2 campaign in Dakar.

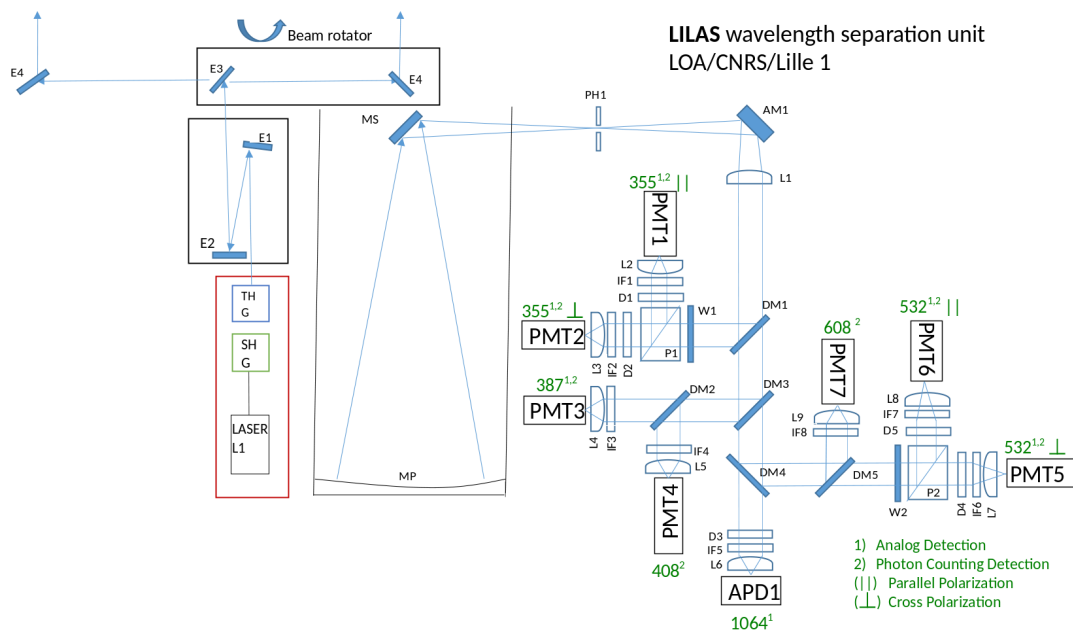


FIGURE 3.3: LILAS optical scheme, basic setup April 2014. LiDAR system is designed and assembled by LOA, PIC and CIMEL.

Freudenthaler, 2008). The main procedures have been applied to LILAS, associated data have been submitted to V. Freudenthaler, in charge of LiDAR quality assurance in EARLINET/ACTIS project. Results of these QA procedures are given in Fig. 3.4 and 3.5):

- Rayleigh fit is the most practical test that shows possible misalignment of laser beam and telescope field of view. In the far range, where no aerosols particles are expected and only molecules exist, the measured LiDAR signal should agrees with calculated or observed by radiosonde molecular (Rayleigh) profile (Fig. 3.4);

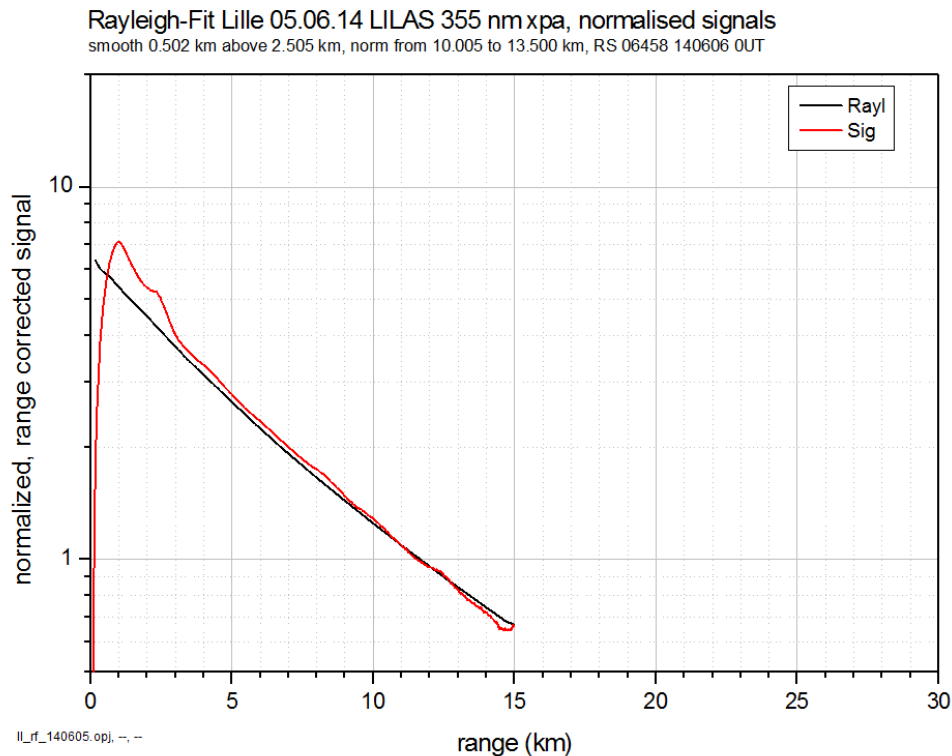


FIGURE 3.4: Rayleigh fit at wavelength 355 nm, analog channel, date of measurements 05.06.2014. Red line is measured and normalized LILAS range corrected signal, black line is precalculated and normalized Rayleigh backscatter. Normalization has been done in altitude range 10.0 km to 13.5 km. Good agreement between precalculated and measured signal indicate appropriate LiDAR alignment.

- "Telecover" test is another main test that helps align optical and opto-mechanical design of LiDAR system. The test consists of signals comparison that are came through the different parts of an aperture. If normalized signals do not show any differences out of the overlap range, telescope and receiver module are designed

and aligned correctly (Fig. 3.5);

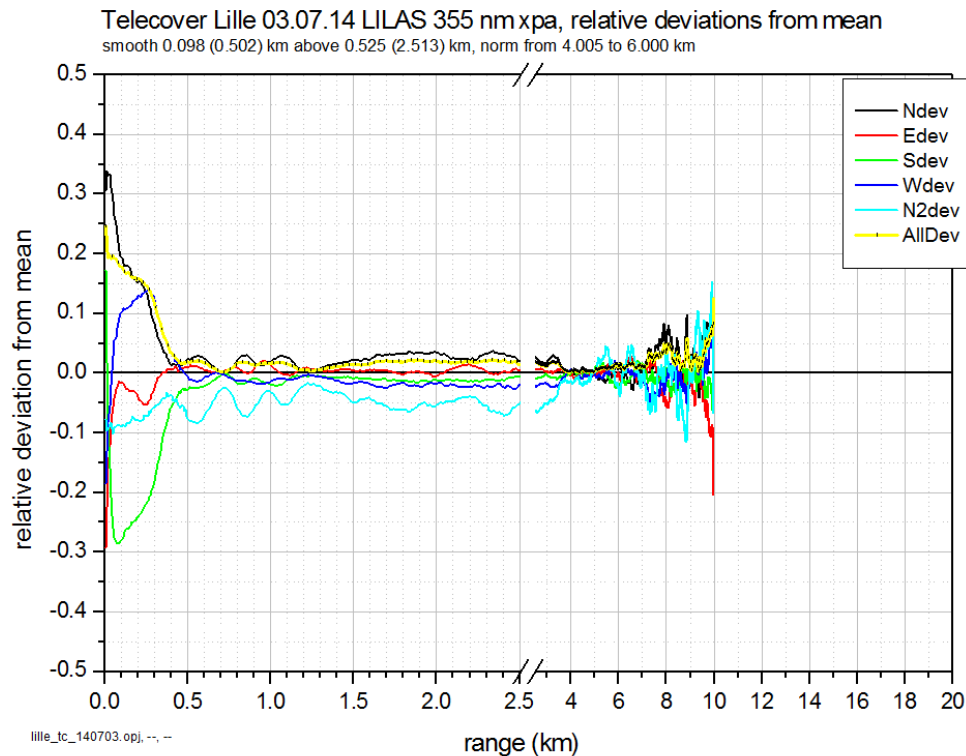


FIGURE 3.5: Telecover test. Relative deviation with open North (Ndev and N2dev), East (Edev), South (Sdev), West (Wdev) sectors of telescope from mean LiDAR signal. AllDev stand for mean of all deviations. Measurements were carried out in Lille 03.07.14, 355 nm analogue channel.

- The trigger delay test finds the delay between outgoing laser pulse and started point of data recording;
- Electro-magnetic interference and other low-frequency noises that can not be removed from spatial or temporal averaging are subtracted using so-called dark measurements, these measurements carried out with the fully covered telescope that avoid background light of the atmosphere. Electrical noise carried out each time before new measurements;
- Depolarization calibration has been firstly done at the beginning of SHADOW-2 campaign and was regularly performed during the campaign. Depolarization calibration is performed by rotating a polarizing filter placed before the pinhole by $\pm 45^\circ$. The calibration constant is calculated according to Freudenthaler et al., 2009:

$$V^{dp} = \frac{R_p + R_s}{T_p + T_s} \sqrt{\delta^*(+45^\circ) \delta^*(-45^\circ)} \quad (3.1)$$

where T_p , T_s , R_p , R_s are transmittance (T) and reflectance (R) of components of polarizing beam-splitter cube of parallel (p) and perpendicular (s) incident light; δ^* is the ratio (see Eq. 2.48) of transmitted (perpendicular incident light) to reflected (parallel incident light) signals for measurements with polarizing filter by $\pm 45^\circ$. Depending on atmospheric conditions, different sets of density filters had been used for various channels, as a result, δ^* and V^{dp} had been changed during the SHADOW-2 campaign.

LILAS passed all EARLINET tests and check ups except the depolarization calibration which is in progress. For instance, volume depolarization ratio of dust event in Dakar in 10 April 2015 is presented in Fig. 3.7 and 3.6.

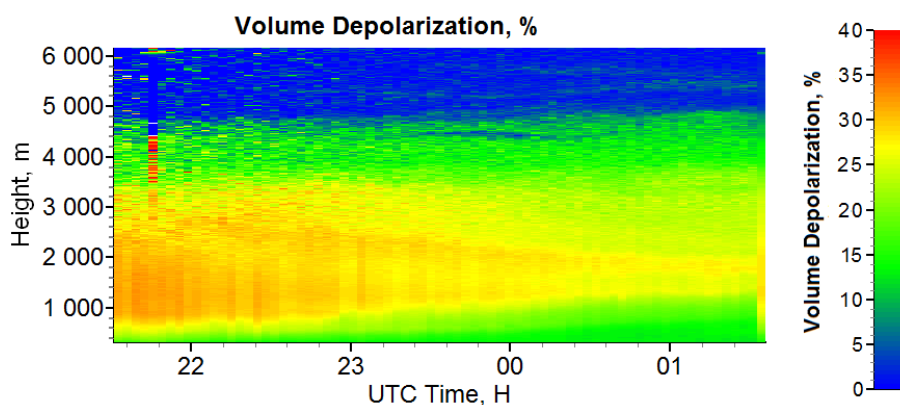


FIGURE 3.6: Quick look of Volume Depolarization Ratio (VDR). Dust event at Dakar site during night from 21:30 of 09 April to 01:30 of 10 April of 2015.

3.2.2 LILAS operation and database

LILAS is designed in a way to be stable instrument with possibility to be operated remotely. Operator can switch on and off LASER remotely, however, telecover test and depolarization calibration request an operator.

Measurements performed at Lille site carry out in the majority of cases when the results could be interesting in operator opinion. During this thesis, when LILAS was

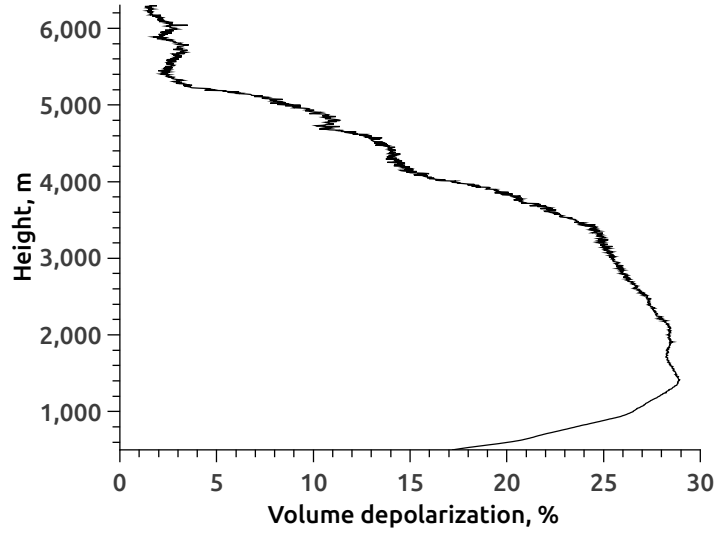


FIGURE 3.7: Profile of volume depolarization ratio. Dust event at Dakar site during the night from 21:30 of 09 April to 01:30 of 10 April of 2015. The profile represents averaged data from Fig. 3.6.

placed in Lille site, I have regularly performed day and night measurements. Instrument collimation and check ups were done regularly.

Raw LILAS measurements are automatically processed and stored into database alongside with raw data. Processed data commonly referred as "level1.0" consists of noise subtracted and range-corrected LiDAR signals. Automatic processing include the following steps:

- 1) Correction on trigger delay. All channels according to its analog or photocounting origin are corrected with respect to the trigger delay defined by Quality Assurance Procedure (Section 3.2.1).
- 2) Electrical noise subtraction. The electrical noise signal is detected by such condition: the ratio between averaged value of the signal in the far range (13–15 km, P') to the averaged value in the near range (1–3 km, P'') equal 1 ± 0.1 . Electrical noise measurements carried out with a fully covered telescope (Section 3.2.1), hence it is enough to check one of the available channels:

$$\frac{\overline{P'_{532nm}}}{\overline{P''_{532nm}}} \in [0.9, 1.1] \quad (3.2)$$

Program takes into account nearest electrical noise before the measured data.

- 3) LILAS use Licel transient recorder system which have a parallel analog and photon counting detection chains. The combination of both signals gives the high linearity of the analog signal for strong signals and the high sensitivity of the photon counting for weak optical signals. The integration of both detection mechanisms into a single device allows to avoid the ground loops and other problems that make the combination otherwise cumbersome. The main idea of the signal combination is that there is a range where both signals are valid and have a high signal to noise ratio. To combine (glue) both signals, the photon counting needs a dead time correction. Licel photon counter can be best described as follows:

$$S = \frac{N}{1 - N\tau_d} \quad (3.3)$$

where N - is the measured count rate, S - is the true counts, τ_d - is the system dead time. Dead time correction in a region lower 10MHz implies.

- 4) Background noise correction. Averaged signal in the region 80 – 120 km is considered as background noise (P_{bg} in the Eq. 2.39) and is subtracted from the full profile.
- 5) In the last step, each profile is multiplied by the square of altitude. This corrects measured LiDAR signal to the range depending measurement geometry (factor $G(R)$ in LiDAR equation, Eq. 2.41). LiDAR signals can be also corrected by the overlap function, but it demands special experiments which is not allowed for non-eye safe LiDARs.

LILAS range-corrected and noise subtracted signals are data level1.0, these data is available online on the web-site: http://www-loa.univ-lille1.fr/Instruments/lidar/calendriers/newcal_2014_lillelilas.php. Some test dataset have been submitted to EARLINET/ACTRIS database in 2016. For instance, a screenshot of web-site is presented in Fig. 3.8. For further analysis analog and photocounting data from the same channel can be glued.

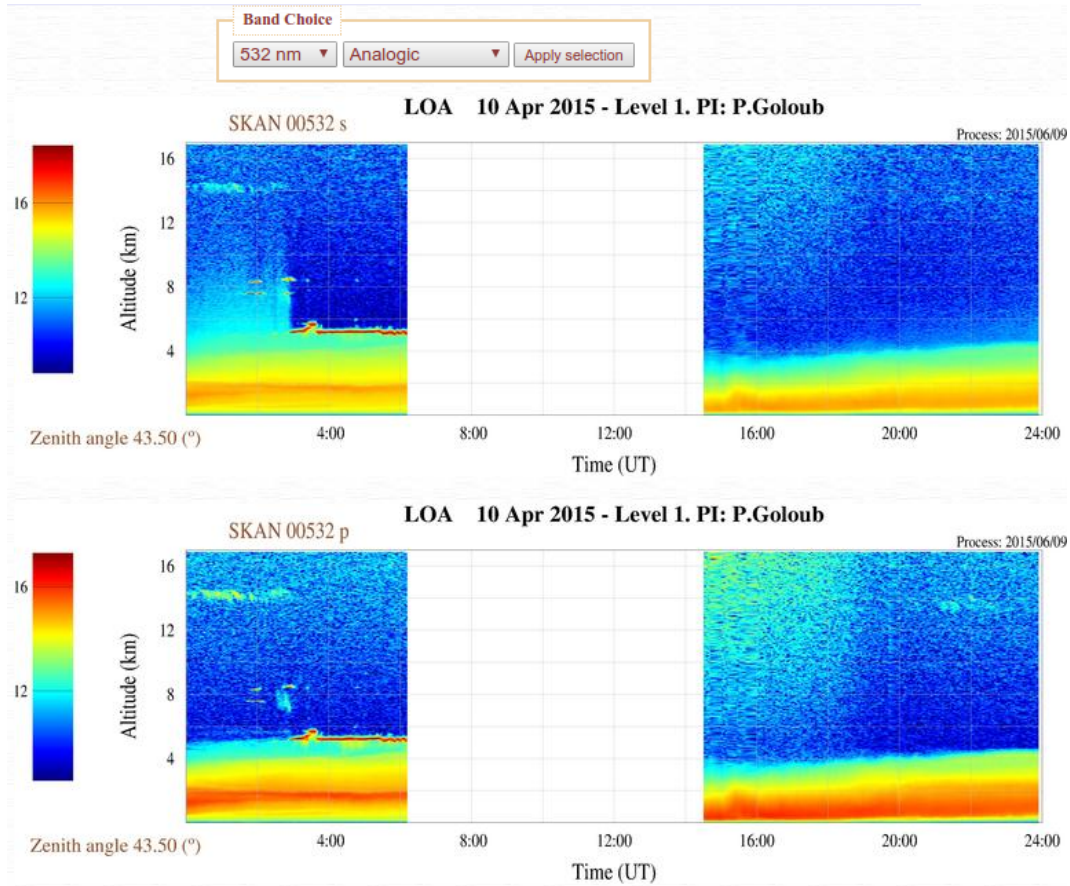


FIGURE 3.8: Range-corrected and noise subtracted LILAS signal (color, in arbitrary units) for 10 April 2015. Analog signal of 532 nm parallel (SKAN 00532 s) and perpendicular (SKAN 00532 p) channels are presented. There was no observation during day-time.

There were attempts to develop an automatic gluing procedure, but it was unsuccessful because some measurements have clouds. Nevertheless, gluing procedure was used for selected data before the analysis.

In the valid region of both signals between the lower toggle rate (typical 0.5 MHz) and the upper toggle rate (typical 10 MHz) for photocounting lidar signal (PC) and between 3 km (at this distance overlap has to be already equal 1) to 10 km (assumed that up to 10 km we have a high signal to noise ratio in an analog signal) of observational distance one seeks the linear regression coefficients to transfer the analog data into photon counting data:

$$\sum_{i=1}^n (PC(z_i) - AD'(z_i))^2 = \min \quad (3.4)$$

where PC - is photocounting lidar signal; AD' - is normalized analog signal to PC signal (transferred analog data), the summation is done inside the gluing region ($z_1 = z_{min}$, $z_n = z_{max}$, $n = 10$). In case of the inherently higher quality of the PC data inside valid region (window) AD data normalized to the PC data by cross-calibrated constant K (Whiteman, Melfi, and Ferrare, 1992; Zhang et al., 2014; Lange et al., 2012):

$$AD'(z) = AD(z) K \quad (3.5)$$

$$K = \frac{\overline{PC(z_i)}}{\overline{AD(z_i)}}; i = \overline{1, n} \quad (3.6)$$

The region with minimum of Eq. 3.4 can be found using moving window between toggle rates 0.5–10 MHz, window has 10 points of lidar signal ($n=10$). The region with minimum value of Eq. 3.4 is the gluing region. Glued signal (GL) defines:

- a) $GL = AD', z < z_1$ (below gluing region)
- b) $GL = \frac{AD'+PC}{2}, z_1 \leq z \leq z_n$ (inside gluing region)
- c) $GL = PC, z > z_n$ (above gluing region)

Also algorithm includes checking procedure that examines chosen window points: are they going one after another or not. If not, one or more of the points are out of 0.5-10 MHz, then the gluing can not be done inside this window and profile.

For example, the result of the procedure is presented in Fig. 3.9. As was mentioned above, this gluing procedure is used only for manually selected data which does not include clouds or other disturbances which make gluing impossible. Some enhancements should be done (cloud detection, etc.) for its future integration into the routine of data processing.

3.3 CIMEL photometer

CIMEL sun/sky-photometer has been proven as a suitable and stable instrument to obtain column integrated atmospheric aerosol properties. It is used in the AERONET

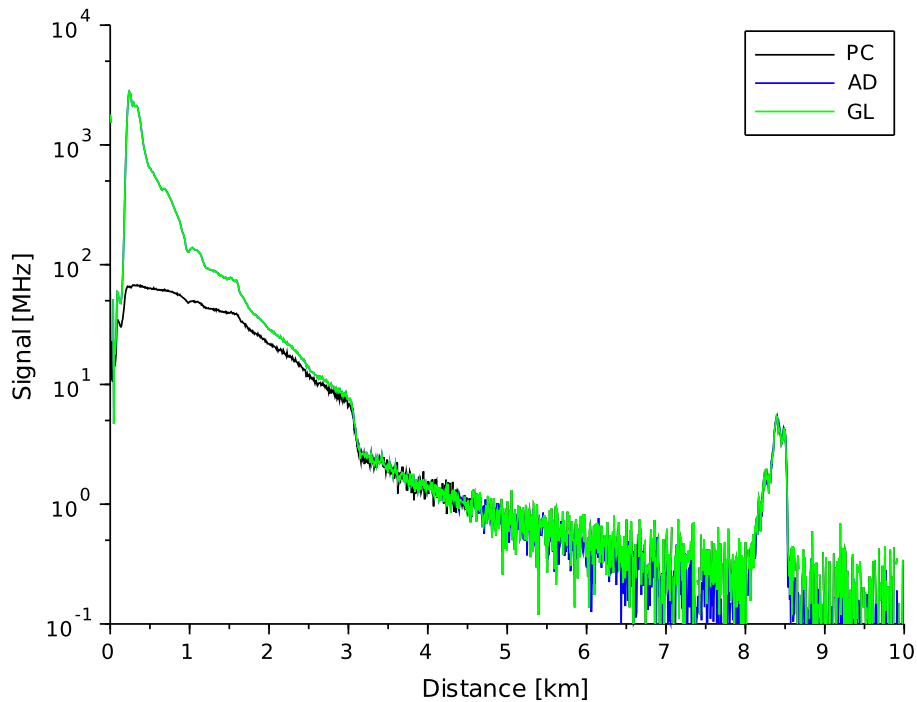


FIGURE 3.9: Signal gluing of 532 nm total channel, measurements were carried out on 26 March 2014 in Lille. AD, PC and GL are analog, photcounting and glued lidar signals, respectively. Glued signal equals to *PC* values above gluing region and transferred *AD* values below gluing region.

(Aerosol Robotic Network, <http://aeronet.gsfc.nasa.gov/>). A complete description of the instrument can be found in (Holben et al., 1998).

The sun/sky-photometer consists of an optical head with two collimators, a robotic arm, and an electronic box. The robotic arm is using for sun tracking and sky positioning. Instrument is automated, and it performs direct sun measurements every 15 minutes, collimators field of view are 1.2° . Typical channels of the instrument are 440, 675, 870 and 1020 nm, but there are modification with additional channels (340, 380, 440, 500, 675, 870, 940, 1020 and 1640 nm). Direct sun and diffuse sky measurements of photometer are using in AERONET inversion code to retrieve such aerosol optical and microphysical properties as aerosol optical depth (AOD), single scattering albedo (ω_0), size distribution ($N(r)$), complex refractive index (m), Angstrom exponent (λ), LiDAR ratio (LR), water vapor content, and others.

Both sites, Lille and Dakar, are equipped with lunar-photometer (Barreto et al., 2013).

It is the same CIMEL sun/sky-photometer, but with some improvements and features which enable photometer to measure the solar light irradiance reflected by the moon and attenuated by the atmosphere. It has eight nominal wavelengths (1640, 1020, 938, 937, 870, 675, 500 and 440 nm). Two channels, 380 and 340 nm, were not included due to the low incoming energy received from the moon in this spectral range. Hence, the instrument provides AOD, AE and water vapor for all clear nights for lunar phase, from half to full moon.

3.4 Radiosoundings

Water vapor and thermodynamic variability are important for atmospheric studies. For instance, particles can be coated by water and as a consequence, aerosol optical properties are changed. Radiosounding is the most common and accurate technique which provides water vapor, pressure and temperature profiles.

There are no radiosounding measurements at Lille and Dakar sites. But for data analysis, data of the nearest radiosounding stations has been selected. Data have been taken from database belonging to Department of Atmospheric Science, University of Wyoming (<http://weather.uwyo.edu/upperair/sounding.html>).

Beauvechain is located in 120 km from Lille in East direction. The number and abbreviation for this station in Wyoming database are 06458 and EBBE. Station placed in South-East direction from Brussels. Similarly to Lille site, it is influenced by urban and industry pollutions, marine aerosols, and rarely by mineral dust and aerosols from volcano eruptions.

Dakar has its own radiosounding observational station (number and abbreviation in Wyoming database are 61641 and GOOY respectively). It is the nearest station to the SHADOW-2 observational site, the distance between sites close to 70 km. Both stations are influenced by the marine particles from West direction, and the mineral dust from East direction.

3.5 Modelling tools

For data analysis, HYSPLIT and NMMB/BSC-Dust models have been used in this work. In synergy, they show the trajectories and the origins of the air-masses which arrived to the observational sites.

3.5.1 NMMB/BSC-Dust model

NMMB/BSC-Dust (Non-hydrostatic Multiscale Model) is a new online multiscale dust model which has been developed at the Barcelona Supercomputing Center (BSC) in collaboration with NOAA/National Centers for Environmental Prediction (NCEP), NASA Goddard Institute for Space Studies and the International Research Institute for Climate and Society (IRI). The model provides short to medium-range weather and dust forecast from regional to global scales. The developers are expecting that the model will improve scientific understanding of the dust cycle by bridging the gap among the multiple scales (Pérez et al., 2011; Haustein et al., 2012). The model tendency to overestimate the very low background dust concentration in the regions far away from the sources (Pérez et al., 2011). This is caused by overestimation of the smallest dust particles due to either inaccuracies in the size distribution of the emissions, vertical transport and/or removal. Nevertheless, this model reproduces fairly well aerosol optical depths and mineral dust vertical distribution according to Amiridis et al., 2009b.

In the work, this model has been used to identify the dust sources.

3.5.2 HYSPLIT model

The analysis of backward trajectories was performed by means of the HYSPLIT model (HYbrid Single-Particle Lagrangian Integrated Trajectory) (Draxler and Rolph, 2015; Rolph, 2015). The model has been developed in joint effort between NOAA (National Oceanic and Atmospheric Administration) and Australia's Bureau of Meteorology, but recent enhancements have been provided by a number of different contributors. The model can be used for analysis of complex deposition and dispersion of pollutants

and hazardous materials. HYSPLIT model can be downloaded and installed on PC or can be run interactively on the web (www.arl.noaa.gov/HYSPLIT). Meteorological data, which are used for the computation, can be introduced by the user or taken from Global Data Assimilation System (GDAS) database.

In this thesis, different backward trajectories have been considered. In case of local events (SHADOW-2 campaign), HYSPLIT model has not been used. In case of dust event over Lille, backward trajectory analysis had been considered. Together with forecasted dust event by NMMB/BSC-Dust, models confirm the source and the passage of the dust over Lille. GDAS database has been used as input meteorological data.

Chapter 4

Methodologies to retrieve aerosol properties

To improve knowledge on aerosol properties, it is necessary to know and use different methodologies and techniques. This chapter presents all methods that have been used/improved, in this work, to retrieve aerosol optical and microphysical properties. The presentation is divided in terms of methods from which aerosol properties were derived: according to sun/sky-photometer and/or LiDAR instruments. In such case, it is possible to find common aerosol properties retrieved by different methods or techniques. The main optical properties that were measured and retrieved are aerosol optical depth (AOD), Angstrom exponent (α), LiDAR ratio (LR), extinction (σ) and backscatter (β) coefficients, vertical distribution of volume concentration (V). The main microphysical properties studied in our work are complex refractive index (m) and effective radius (r_{eff}).

GARLLiC algorithm is the core of this work. For this reason, a large part of this chapter is dedicated to this algorithm and presents several enhancements proposed and implemented into GARLLiC algorithm.

4.1 Retrieval of optical properties

4.1.1 Method which uses sun/sky-photometer primary measurements

Direct sun-photometer measurements are used to obtain AOD and AE. Aerosol particles absorb and scatter sunlight in Earth's atmosphere, the processes can be presented by Beer-Lambert-Bouguer law:

$$E(\lambda, z) = E_0(\lambda) \exp[-\tau(\lambda, z) m] \quad (4.1)$$

where $E(\lambda, z)$ and $E_0(\lambda)$ - are monochromatic irradiance at wavelength λ on altitude z and on the top of Earth's atmosphere, $\tau(\lambda, z)$ - is optical depth from top of atmosphere to altitude z (see Eq. 2.12), m - relative air mass (see Eq. 2.13). Irradiance at altitude z measures by sun-photometer, energy on the top of atmosphere can be derived from the instrument calibration, and solar zenith angle is known, hence total optical depth can be found from Eq. 4.1. Then, AOD can be found as subtraction of total OD to molecular OD (Eq. 2.15).

Atmospheric measurements in several channels allow determination of Angstrom exponent (see Eq. 2.17):

$$\alpha = -\frac{\ln[\tau(\lambda_1) / \tau(\lambda_2)]}{\ln[\lambda_1 / \lambda_2]} \quad (4.2)$$

Usually used 440 and 870 nm wavelengths to compute α . However other couples of wavelengths can be used to be more consistent with LiDAR wavelengths.

Primary measurements also include sky spectral and angular radiances; these measurements are used for retrieval aerosol microphysical properties (see Section 4.2.1).

4.1.2 Methods using LiDAR data

a) Klett method

The general form of LiDAR equation could be found in Chapter 2.6 (Eq. 2.47). It includes two unknowns ($\sigma^{ext}(z)$ and $\beta_a(z)$), other extinction or backscatter coefficients (Eq. 2.43 and 2.46) can be neglected or are known. Stable analytical inversion for the elastically backscattered LiDAR returns have been developed by Klett (Klett, 1981; Klett, 1985). This method is based on a relationship between extinction and backscattered coefficients, called LiDAR ratio (Eq. 2.22 and 2.24):

$$LR_{aer}(\lambda, z) = \frac{\sigma_{aer}(\lambda, z)}{\beta_{aer}(\lambda, z)} \quad (4.3)$$

In general, aerosol LiDAR ratio is a range depending because extinction and backscatter coefficients depend on shape, size distribution, and chemical composition of particles, that, for sure, can vary with location in the atmosphere. On the opposite, the molecular LiDAR ratio, LR_{mol} ($\sigma_{mol} / \beta_{mol} = 8\pi/3sr$), is not range depending.

Under the assumption that LiDAR ratio is known, the equation for $\beta(z)$ can be solved by iterations from reference altitude, z_0 , down to altitude z :

$$\beta_{aer}(z) + \beta_{mol}(z) = \frac{RCS(z) \exp \left[-2 \int_{z_0}^z [LR_{aer}(z') - LR_{mol}] \beta_{mol}(z') dz' \right]}{\frac{RCS(z_0)}{\beta_{aer}(z_0) + \beta_{mol}(z_0)} - 2 \int_{z_0}^z LR_{aer}(z') RCS(z') T(z', z_0) dz'} \quad (4.4)$$

where $RCS(z)$ - is the range corrected LiDAR signal at altitude z ($RCS(z) = P(z, \lambda) \cdot z^2$), z_0 - reference range, and

$$T(z, z_0) = \exp \left[-2 \int_{z_0}^z [LR_{aer}(z') - LR_{mol}] \beta_{mol}(z') dz' \right] \quad (4.5)$$

The reference range should be chosen in the range of altitudes where β_{aer} is negligible in comparison to β_{mol} to reduce the uncertainties of solution.

Aerosol extinction profile can be obtained from LiDAR ratio equation. Hence, retrieval of β_{aer} and σ_{aer} rely on the a priori LR choice. This restriction increase uncertainty of σ_{aer} , especially when the types of aerosols are unknown (typical LR values of different aerosol types are presented in Table 4.1).

b) Raman method

The process of inelastic scattering has been described in Chapter 2.3, and LiDAR instruments based on this process have been presented in Chapter 2.6.3. Raman technique yields a system of two equations with two unknown parameters. With assumption that extinction coefficient depends on wavelength through Angstrom law (see Eq. 4.2), aerosol extinction coefficient can be directly written as (Weitkamp, 2005):

$$\sigma_{aer}(\lambda_{Li}, z) = \frac{\frac{d}{dz} \left[\ln \frac{N(z)}{z^2 P(z)} \right] - \sigma_{mol}(\lambda_{Li}, z) - \sigma_{mol}(\lambda_{Ra}, z)}{1 + \left(\frac{\lambda_{Li}}{\lambda_{Ra}} \right)^{\alpha(z)}} \quad (4.6)$$

where $P(z)$ is the power received at Raman wavelength λ_{Ra} from distance z , $N(z)$ is the molecular number density (known), $\sigma_{mol}(\lambda_{Li}, z)$ and $\sigma_{mol}(\lambda_{Ra}, z)$ are the molecular extinction coefficients at LiDAR and Raman wavelengths respectively, and $\alpha(z)$ is the Angstrom exponent. The aerosol backscatter coefficient (β_{aer}) can be calculated from the ratio of elastic signal $P(z, \lambda_{Li})$ to Raman signal $P(z, \lambda_{Ra})$ using a determined coefficient at a reference point $P(z_0, \lambda_{Ra}) / P(z_0, \lambda_{Li})$ where no aerosol particles are expected. The solution for the backscatter coefficient is:

$$\begin{aligned} \beta_{aer}(z, \lambda_{Li}) + \beta_{mol}(z, \lambda_{Li}) = & \\ & (\beta_{aer}(z_0, \lambda_{Li}) + \beta_{mol}(z_0, \lambda_{Li})) \frac{P(z_0, \lambda_{Ra}) P(z, \lambda_{Li})}{P(z_0, \lambda_{Li}) P(z, \lambda_{Ra})} \\ & \frac{N(z)}{N(z_0)} \frac{\exp \left[- \int_{z_0}^z (\sigma_{aer}(z', \lambda_{Ra}) + \sigma_{mol}(z', \lambda_{Ra})) dz' \right]}{\exp \left[- \int_{z_0}^z (\sigma_{aer}(z', \lambda_{Li}) + \sigma_{mol}(z', \lambda_{Li})) dz' \right]} \end{aligned} \quad (4.7)$$

Type of particles	Typical LR value [sr]
Marine particles	20–35
Saharan dust	50–80
Less absorbing urban particles	35–70
Absorbing particles from biomass burning	70–100

TABLE 4.1: Typical LR of different aerosol types at 532 nm wavelength determined with a Raman LiDAR. Table is taken from (Weikamp, 2005).

If the two channels are properly aligned, the overlap is canceled out by the ratio of LiDAR signals $P(z, \lambda_{Li})/P(z, \lambda_{Ra})$. Hence, the backscatter coefficient can be determined in ranges close to the LiDAR.

In comparison to Klett method, Raman σ and β coefficient profiles are defined separately and, as a consequence, the vertical profile of LR_{aer} can be found. As it was mentioned above, LR_{aer} can strongly vary with altitude, especially if several aerosol layers with different types of particles are presented in the atmosphere. Moreover, even if there is only one type of particles, LR can change with height because of the changes in relative humidity profile which influences on microphysical, chemical, and morphological properties of the particles. Typical LR of the main aerosol types are presented in Table 4.1.

4.1.3 Method combining sun-photometer and LiDAR measurements

The combination of column integrated sun-photometer and vertically resolved LiDAR measurements have been developed at LOA and called BASIC. It is based on Klett method (Mortier et al., 2013). BASIC algorithm is operated in routing manner, on LOA server for CIMEL LiDAR elastic measurements (http://www-loa.univ-lille1.fr/cgi-bin/lidar_dyn.cgi?12). The extinction profile in BASIC is derived following an iterative procedure based on a simple dichotomy where the LR can vary between 10 to 140 sr. The procedure ends when the integral of extinction profile is close to the AOD measured by the sun-photometer within $\Delta AOD=0.01$. BASIC uses only AOD measurements, hence it derives day and night-time extinction profiles. Additionally, the algorithm includes the detection of clouds and heights of boundary

layer. BASIC can also be used with a priori LR. BASIC is also used in routing mode at a national level (AERIS/ICARE, <http://www.icare.univ-lille1.fr/>).

4.2 Retrieval of microphysical properties

As shown in Chapter 4.1, aerosol optical properties can be derived directly from the sun-photometer or LiDAR data. Unfortunately, aerosol microphysical properties can not be derived directly from remote sensing measurements, inversion methods are used for this purpose. Inversion of primary spectral and angular measurements can be used to derive aerosol microphysical properties. This section briefly presents several methods which are used in the thesis.

4.2.1 Inversion of sun/sky-photometer data

The well-known inversion algorithm developed by Dubovik and King, 2000; Dubovik et al., 2011 is commonly used for retrieval aerosol microphysical properties. Additionally to the direct sun measurements, observations in principle plane or almucantar directions are needed for aerosol microphysical properties retrieval. Measurements with different azimuthal (φ_a) and the same zenith (θ_s) angles are called almucantar measurements (right panel b) in Fig. 4.1). Principle plane measurements are opposite to almucantar measurements, zenith angles (θ_p) are varying and azimuthal angle remains constant (left panel a) in Fig. 4.1).

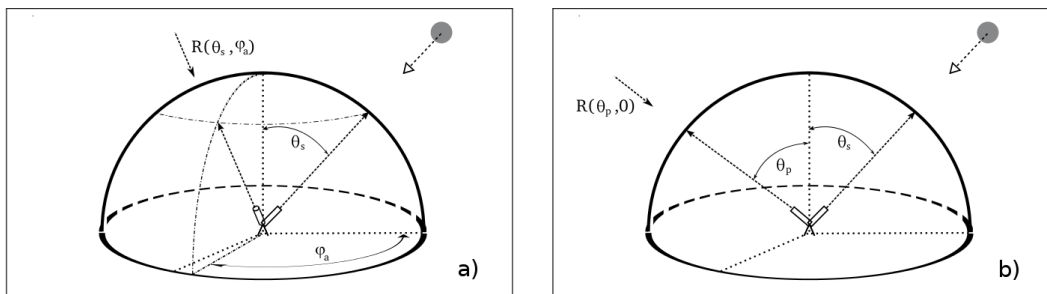


FIGURE 4.1: Two geometries used in sky radiance measurements: a)almucantar; b) principle plane. Both present direct measurements in the direction to sun. The figure is taken from (Lopatin, 2013).

The results of algorithm implementation have been proven in many different atmospheric conditions that allowed to obtain particles properties at various locations of

the world (Dubovik et al., 2002b). The model of randomly oriented spheroid particles have shown applicability for the retrieval microphysical properties of non-spherical particles (Dubovik et al., 2006). Additionally to optical properties such as AOD, AE, SSA, algorithm retrieves aerosol microphysical properties such as size distribution (SD), complex refractive index (CRI), effective radius (r_{eff}). The error of the retrieved size distribution ($dV(r)/d\ln(r)$) depends nonlinearly on particles radii and actual value of retrieved parameter (Dubovik et al., 2000; Dubovik et al., 2006; Dubovik et al., 2011). Errors do not exceed 10% for particles having the size in the range $0.1 \leq r \leq 7 \mu m$ (where size distribution usually has its maxima), and may increase up to 35% on the edges of distribution where values of SD goes to minima. Additional errors are caused by low sensitivity of aerosol scattering for the particles which have size in the ranges $0.005 \leq r \leq 0.1 \mu m$ and $7 \leq r \leq 15 \mu m$. Hence, the retrieval error increases to 80% – 100% for the particles having size ranges less than $0.1 \mu m$ or higher than $7 \mu m$. But high errors on the edges do not significantly influence the retrieval of the main aerosol properties such as concentration, median and effective radii. It can be explained by low values of size distribution on the edges. The accuracies of other main aerosol properties are (i) 0.05 – 0.07 for single scattering albedo, (ii) 0.05 for real part of the refractive index, and (iii) 80% – 100% for imaginary part of the refractive index (Muñoz, 2014).

4.2.2 Inversion of LiDAR data

As previously mentioned, there are a variety of methods designed to retrieve aerosol microphysical properties using LiDAR data. In general, they can be divided into three main groups (Weitkamp, 2005). The first group deals with the combination of LiDAR data and data of another instrument, one of such methods is a core of our work and it is presented in next Chapter 4.3.

In the second group of methods, optical properties such as σ and β are reconstructed by Mie-scattering calculations from multiwavelength lidar observations. Then obtained properties are compared with the results of an application of the Raman technique on actual measurements (Wandinger et al., 1995; Barnaba and Gobbi, 2001). In these methods, aerosol microphysical properties such as SD and CRI are assumed a

priori. Such methods are used only in cases of the atmospheric layer with one well-known type of particles. Polar stratospheric clouds, ejecta from volcanic eruptions, and stratospheric particles are such kind of particles. Due to the variety of particles and the rapid changes in tropospheric conditions, such methods are not used in lower atmosphere.

The third group of methods uses an assumption that the aerosol optical properties are connected with aerosol microphysical properties through the Fredholm integral equation of the first kind:

$$g_i(\lambda_k, z) = \int_0^{\infty} K_i(r, m, \lambda_k, s) V(r, z) dr + \varepsilon_i(\lambda_k, z) \quad (4.8)$$

where $g_i(\lambda_k, z)$ denotes backscatter or extinction coefficient at wavelength λ_k and at height z , $\varepsilon_i(\lambda_k, z)$ - data error for certain aerosol optical property, $K_i(r, m, \lambda_k, s)$ - kernel efficiency of certain aerosol optical property (backscatter or extinction) that depends on particles radius r , complex refractive index m , and shape of particles s , $V(r, z)$ - volume concentration of particles. The main problem, which has not been fully solved yet, is how the inversion method by itself can find the most suitable kernel representation in each individual data set. Some studies have been made based on modified version of Tikhonov method (Veselovskii et al., 2002; Veselovskii et al., 2004), called inversion with regularization (we will call it "Regularization" in the thesis). Both methods, Tikhonov method and Regularization algorithm form penalty terms from physical constraints such as positivity and smoothness of the derived size distribution, CRI in some range, etc. Then, the classical Tikhonov method accepts only one solution of inversion at the global minimum of the penalty function. Regularization algorithm averages several solutions of different inversions in the vicinity of the minimum penalty functions. By this, Regularization algorithm reaches its primary goal, stabilizes the underlying ill-posed problem.

4.2.3 Inversions based on synergy between sun/sky-photometer and LiDAR data

In such methods, the collocation of measurements in space and time is very essential. In situ instruments carried aboard aircraft or balloon, or passive remote sensing instruments, like sun/sky-photometer, can be used as a coincident measurement to LiDAR data. Several in situ measurements should be carried out along the LiDAR light to have coincident observations in space and time. Such experiments are expensive and complicated, but they can be very interesting for aerosol studies. The sun/sky-photometer measurements can provide the time coincident column integrated microphysical particle properties. The main disadvantage is that LiDAR and sun/sky-photometer instruments aim in different directions. However, the almucantar sky radiance measurements allow to check and therefore usage of the assumption about spatial homogeneity of aerosols (Chaikovsky et al., 2012; Lopatin et al., 2013; Biniotoglou et al., 2015; Raut and Chazette, 2007; Tsekeri et al., 2013).

The LIRIC (Lidar-Radiometer Inversion Code) (Chaikovsky et al., 2012; Chaikovsky et al., 2015; Wagner et al., 2013; Granados-Muñoz et al., 2014) algorithm is a successful attempt of retrieving height resolved optical and microphysical particle properties separately for fine and coarse aerosol modes. This algorithm uses AERONET inversion products, such as column volume concentration, volume-specific backscatter and extinction coefficients, as a priori information (Chaikovsky et al., 2012). The LiDAR spectral backscatter and extinction profiles are used to derive a vertical distribution of two optically distinct aerosol modes assuming that concentrations of fine and coarse aerosol modes can change vertically. The algorithm products are backscatter, extinction and volume concentration profiles, Angstrom exponent, LiDAR and depolarization ratios.

A deeper synergy of LiDAR and sun/sky-photometer data is achieved with the GARRLiC algorithm (Generalized Aerosol Retrieval from Radiometer and LiDAR Combined data) developed in LOA (Lopatin et al., 2013; Lopatin, 2013). GARRLiC simultaneously inverts coincident LiDAR and sun/sky-photometer radiometric data. The

other remarkable distinction between GARRLiC and LIRIC is the inversion of two distinct aerosol modes, which make it possible to retrieve aerosol optical and microphysical properties independently for both fine and coarse modes. It should be mentioned, that such differences in algorithms can profoundly impact on their results. GARRLiC is based on Dubovik inversion code (Dubovik and King, 2000; Dubovik et al., 2011), which is very flexible. It relies on multi-term least square method (LSM) which allows to do the inversion with various combinations of independent measurements. The inversion code has two modules "forward model" and "numerical inversion" which can be modified independently (see Fig. 4.2). Hence, for simulation of new characteristic, for instance LiDAR signal, "numerical inversion" module stays without modifications. Development of the LiDAR signal simulation have been done by Lopatin (Lopatin, 2013). In our work, we have proposed and implemented some developments in a forward model which directly deals with observations (see Chapter 4.3.2). The aim of the forward model is to properly model all the processes in Earth's atmosphere for providing accurate simulations of observations. A priori constraints and assumptions of measurement errors are defined by inversion settings which could be changed by a user. All these parameters are taken into account in numerical inversion.

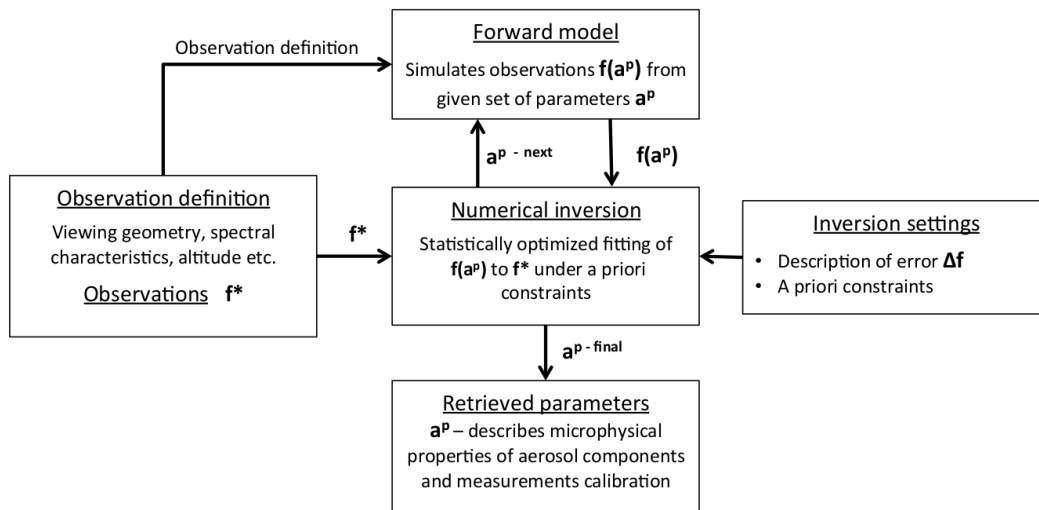


FIGURE 4.2: General structure of inversion code, taken from (Lopatin, 2013).

GARRLiC works with mono- and multi-wavelength LiDAR data (elastic channels).

The algorithm uses spectral information of multi-wavelength LiDAR data to distinguish the contribution of fine and coarse aerosol modes. That is why, in case of mono-wavelength LiDAR data, only one component for total aerosol amount (without separation on fine and coarse modes) are retrieved. This conforms to one mode inversion. In case of multi-wavelength LiDAR data, one or two mode inversion can be implemented (the number of retrieved modes sets up by user), in such cases common or separated into fine and coarse modes aerosol properties are retrieved. GARRLiC products that can be derived using one or two mode inversion are presented in Fig. 4.3. It should be noted, if there are multi-wavelength LiDAR data but event is characterized mainly by one type of aerosol, one mode inversion should be used. Other types of aerosols cause negligible influence on the retrieved aerosol properties.

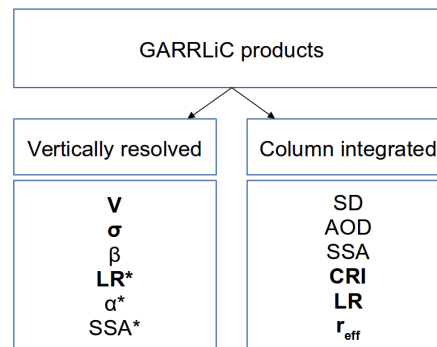


FIGURE 4.3: GARRLiC products derived using one (unmarked) or two (both, unmarked and marked *) mode inversions. Latter can be applied only to multi-wavelength LiDAR data. Bold font indicates common properties retrieved using GARRLiC, LIRIC, Raman and Regularization methods. Figure is taken from (Bovchaliuk et al., 2016).

GARRLiC algorithm uses sun/sky-photometer and LiDAR measurements simultaneously, it is a powerful tool for aerosol optical and microphysical properties retrieval. Such synergetic inversion improves retrieved aerosol properties (Lopatin, 2013), LiDAR backscattering observations improve the sensitivity to the columnar properties of aerosol, and sun/sky-photometer observations provide sufficient information about aerosol properties, such as amount or type of certain aerosol component required for the LiDAR retrievals without making any assumptions based on the climatological data. Nevertheless, some improvements can be done and have been already implemented during the thesis. They are presented further.

4.3 GARRLiC algorithm

4.3.1 General description

Similarly to LIRIC, GARRLiC independently provides information, the namely height profile of volume concentration, about two particle modes. But GARRLiC considers aerosol modes separately, as a results different aerosol microphysical properties might be retrieved for each mode. The concept of the modeling of two aerosol components in GARRLiC algorithm is presented in Fig. 4.4. The algorithm is the part of GRASP (Generalized Retrieval of Atmosphere and Surface Properties, developed by LOA (CNRS/Lille1) and now publically available at <http://www.grasp-sas.com/>) code. GRASP provides services in every area of remote sensing, especially in the observations of earth atmosphere and surface (Dubovik et al., 2014).

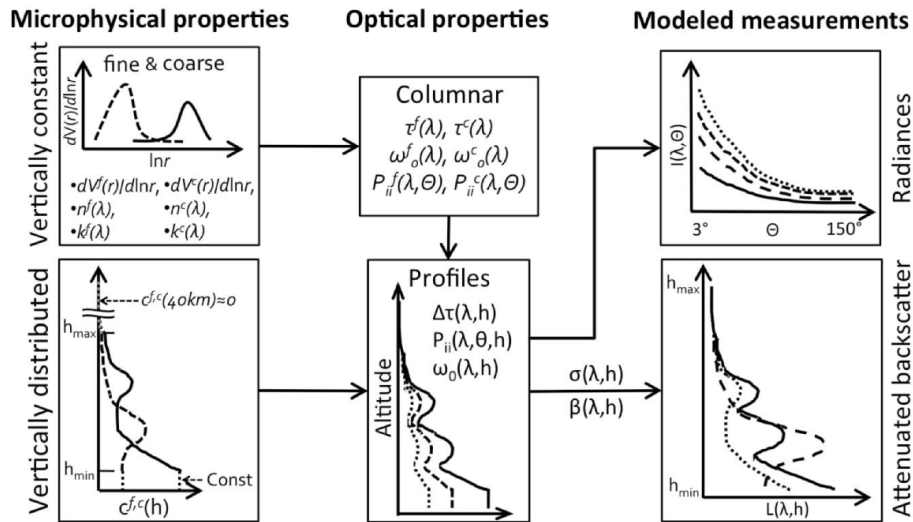


FIGURE 4.4: Modeling of two aerosol components in GARRLiC algorithm, taken from (Lopatin, 2013).

As it was mentioned above, an improvements in the code (Dubovik and King, 2000; Dubovik et al., 2006; Dubovik et al., 2011) have been introduced in the forward model. Sun/sky-photometer measurements accumulate optical properties of atmosphere column, their sensitivity to vertical distribution of aerosol properties remains negligible. Instead of that, LiDAR measurements are highly sensitive to the vertical distribution of aerosol properties. Hence, developed module provides profiles of aerosol vertical properties thanks to LiDAR sounding which are consistent with columnar integrated values provided by sun/sky-photometer measurements. In the modified algorithm

sun/sky-photometer observations are simulated by means of solving vector radiative transfer equation and elastic LiDAR observations are simulated by LiDAR equation. Fig. 4.5 shows a general scheme of the forward model of the GARRLiC algorithm.

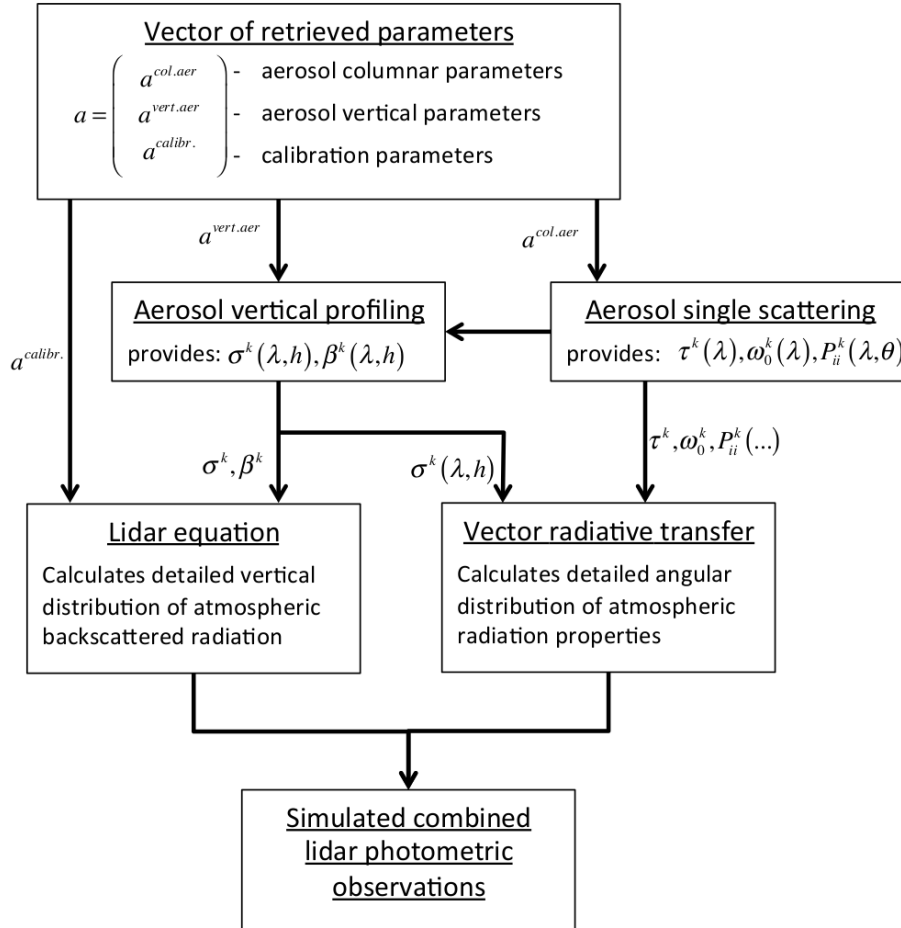


FIGURE 4.5: General scheme of GARRLiC algorithm, taken from (Lopatin, 2013).

Forward model

The modeling of aerosol columnar optical properties used in the study is based on Dubovik and King, 2000; Dubovik et al., 2006; Dubovik et al., 2011. GARRLiC models aerosols as a mixture of spherical and non-spherical particles. The spherical fraction is modeled as a polydisperse mixture of the spheres (Mishchenko, 2014), and the non-spherical fraction is modeled as a mixture of randomly oriented polydisperse spheroids by making use of T-matrix computation (Mishchenko et al., 1997; Dubovik et al., 2006). Complex refractive index and particle volume distribution for each aerosol component are assumed to be the same for spheres and spheroids. Also,

the fraction of spheres and spheroids and axis ratio of spheroids are modeled similar to both components. Hence, for simulation of the scattering and extinction optical thicknesses, one can use following equations:

$$\tau^{sca}(\lambda) P(\theta, \lambda) \approx \left[\sum K^{sca}(\theta, \lambda, n, k, \varepsilon_p) \omega(\varepsilon_p) \right] \nu \quad (4.9)$$

$$\tau^{ext}(\lambda) \approx \left[\sum K^{ext}(\lambda, n, k, \varepsilon_p) \omega(\varepsilon_p) \right] \nu \quad (4.10)$$

where τ^{ext} and τ^{sca} - are an optical thickness of extinction and scattering, $P(\theta, \lambda)$ - is phase function, ν - is a vector of the size distribution values. The elements of the matrices $K^{ext}(\dots)$ and $K^{sca}(\dots)$ are precomputed once with high accuracy by integrating the extinction and scattering cross sections of spheroids. The spheroids of all sizes p have the same distribution of aspect ratios ε_p , which is represented by the weighting function:

$$\sum_{\varepsilon_p} \omega(\varepsilon_p) = 1 \quad (4.11)$$

GARRLiC algorithm has successfully used the normalized attenuated backscatter profiles $L(\lambda, z)$ for modeling and comparison with actual data. This normalized attenuated backscatter profile is defined by the measured LiDAR signal divided by its averaged value at the reference point (z_{ref}) and multiplied by the attenuation due to the atmospheric molecules. Hence, in one hand, $L(\lambda, z)$ depends on the reliability of the measured signal at the reference point. To decrease uncertainties caused by non-optimal selection of reference point additional parameter $A(\lambda)$ had been introduced into retrieval algorithm (Lopatin, 2013; Chaikovsky et al., 2004). In other hand, this normalization procedure allows avoiding unknown system factors $K(\lambda)$ (see Eq. 2.39), which is undefined in most LiDAR systems. Therefore, to adequately represent LiDAR measurements GARRLiC algorithm successfully used the following equation (Lopatin, 2013):

$$L(\lambda, z) = A(\lambda) (\beta_{mol}(\lambda, z) + \beta_{aer}(\lambda, z)) \exp \left[2 \int_z^{z_{ref}} \sigma_{aer}(\lambda, z') dz' \right] \quad (4.12)$$

where $A(\lambda) = \beta_{mol}(\lambda, z_{ref}) / (\beta_{aer}(\lambda, z_{ref}) + \beta_{mol}(\lambda, z_{ref}))$ is so-called backscatter ratio. This parameter describes the uncertainty of the calibration procedure and allows accounting the presence of aerosol on the reference altitude (Russell, Swissler, and McCormick, 1979).

Such representation has some disadvantages:

- (i) Normalization procedure can cause additional errors if the selection of reference altitude is not optimal;
- (ii) Additional parameter, $A(\lambda)$, should be retrieved between the other aerosol characteristics increasing number of parameters to retrieve;
- (iii) Finding the reference point is generally a manual procedure which requires a user. This makes impossible to automatize the retrieval procedure for long term data set;
- (iv) The effects of gaseous absorption and scattering in GARRLiC are accounted by COSPAR International Reference Atmosphere model (<http://ccmc.gsfc.nasa.gov/modelweb/atmos/cospar1.html>), while user can use other atmospheric model for estimating molecular attenuation during the calibration procedure.

Enhancements which have been implemented into GARRLiC forward model to avoid these disadvantages are described in Section 4.3.2.

Aerosol vertical distribution of fine and coarse modes are simulated under the assumption that volume concentration, size distribution, complex refractive index and particle fraction of columnar aerosol properties are vertically independent. The backscatter and extinction coefficients can be written:

$$\beta(\lambda, z) = \frac{1}{4\pi} \sum_{k=1,2} \sigma_{aer}^k(\lambda, z) \omega_0^k(\lambda, z) P_{11}^k(180^\circ, \lambda) \quad (4.13)$$

$$\sigma_{aer}^k(\lambda, z) = \tau_{aer}^k(\lambda) c_{aer}^k(z) \quad (4.14)$$

where the vertical profiles of volume concentration $c_{aer}^k(z)$ is normalized to unity:

$$\int_0^{z_{max}} c_{aer}^k(z') dz' = 1 \quad (4.15)$$

Usually, LiDAR measurements have high vertical resolution (from 5 to 30 m), that is why, in order to avoid an excessively large number of the retrieved parameters and to decrease the inversion time, the number of altitudes used in retrieval is decreased to 60 points. Since air density decreases exponentially, the similar scale is expected for the variability of aerosols. That is why the logarithmically equidistant ($\Delta \ln(z) = Const$) altitude scale has been chosen for describing the aerosol concentration profiles in the algorithm. Moreover, such choice of the logarithmic height scale results in useful noise reduction. Decreasing in the number of altitudes in logarithmically equidistant order should be done before the inversion.

LiDAR measurements have some limitations due to overlap function at lower altitudes and low signal to noise ratio in upper altitudes. Hence, vertical profiles can be derived in some trustworthy altitude range which are presented into GARRLiC algorithm with LiDAR data. As a consequence, some assumptions should be made to proceed outside of this altitude range. Thus, GARRLiC assumes a linear decrease (in logarithmic height scale) of aerosol concentration from its value at highest elevation presented in LiDAR data to 0 at 40 km. Aerosols concentration below the lowest altitude presented in LiDAR data are assumed to be constant and equal to the value at lowest elevation estimated by the algorithm (see Fig. 4.6).

Numerical inversion

When the atmospheric characteristics are known, including optical and microphysical properties of atmospheric aerosols, as well as their vertical distribution, forward model could calculate the radiation field that is observed by both passive and active instruments. Such observations could be used to infer the optical and microphysical

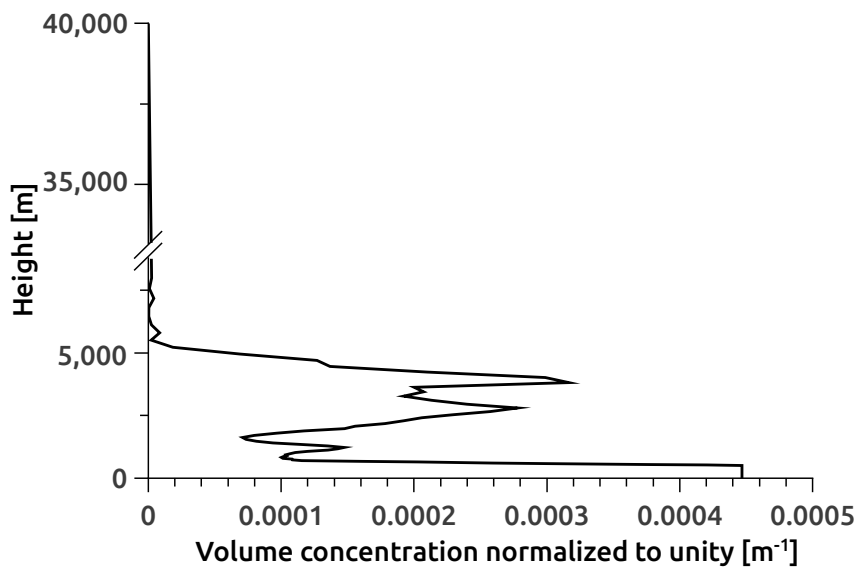


FIGURE 4.6: Representation of aerosol volume concentration above and below LiDAR data used by GARRLiC algorithm. Height presented in linear scale (not logarithmic), hence aerosol concentration decreases exponentially above maximum altitude presented by LiDAR data (here 8 km).

properties of aerosol particles in the atmosphere together with their vertical distribution.

As was mentioned above (Section 2.7), often the task can be accomplished by simple comparison of the measurements with the forward model computations for a wide range of aerosol parameters. This method is referred to so-called look-up tables. It obtains a solution by comparing measurements directly with theoretical calculations. Despite being stable and fast-and-easy in implementation, the look-up table solution is limited to a set of potentially admissible solutions that are included in the look-up table.

However, some methods are not limited to a predefined set of aerosol classes and instead search for the set of aerosol parameters. These methods optimize the error distribution of the retrieved parameters, providing the best fitting of the measurements through the continuous space of all possible solutions under statistically formulated criteria. These rigorous and more sophisticated methods consist in inverting a set of measurements to infer the input properties of the given forward model and usually referred to as numerical inversion.

Nonetheless, in practice, several different combinations of aerosol parameters often produce nearly the same radiation field. Therefore, the general solution is fundamentally non-unique or becomes so in the presence of measurement noise. As was mentioned above, such inversion problem is known as ill-posed. An ill-posed inversion could provide a satisfactory result once additional information is added to constrain the solution while representing the measurement field within the errors established for the measurements. Such information is referred as a priori assumptions, and usually is applied in the form of constraints of aerosol smoothness parameters. The values of a priori assumptions and smoothness constraints are included into input data set and, hence, can be changed by user.

In contrast to the majority of existing aerosol retrieval algorithms, the one used in this work is one of the first attempts to develop an aerosol retrieval algorithm using statistically optimized multi-variable fitting of multi-instrumental data. Detailed description of inversion methodology could be found in (Dubovik and King, 2000; Dubovik, 2004; Dubovik et al., 2008; Dubovik et al., 2011). And detailed description about GARRLiC algorithm can be found in (Lopatin et al., 2013; Lopatin, 2013).

4.3.2 Enhancements implemented into the GARRLiC algorithm

Molecular extinction and backscatter profiles

Aerosol concentration is among the primary aerosol properties since it defines both, the backscatter and extinction coefficients. In one hand, vertical distribution of aerosol concentration forms LiDAR signal, but in another hand, its columnar value forms sun/sky-photometer data. Hence, it makes sense to represent aerosol concentration profile as a vector normalized to unity (Eq. 4.15, Fig. 4.6). Integral of this vector equals unity and can easily conform to the column value.

Consequently, molecular extinction and backscatter profiles can be represented in a similar way. This has been implemented into the algorithm using model of the standard atmosphere (Krueger and Minzner, 1976). Thus, following equations can be added to Eq. 4.13– 4.15:

$$\beta_{mol}(\lambda, z) = \frac{3}{8\pi} \sigma_{mol}(\lambda, z) \quad (4.16)$$

$$\sigma_{mol}(\lambda, z) = \tau_{mol}(\lambda) c_{mol}(z) \quad (4.17)$$

$$\int_0^{\infty} c_{mol}(z') dz' = 1 \quad (4.18)$$

By making use of Eq. 4.13– 4.15 and 4.16– 4.18 the LiDAR equation in forward model (Eq. 4.12) were rewritten:

$$L(\lambda, z) = K(\lambda) (\beta_{aer}(z) + \beta_{mol}(z)) \exp \left[-2 \int_0^z (\sigma_{mol}(\lambda, z') + \sigma_{aer}(\lambda, z')) dz' \right] \quad (4.19)$$

Hence, aerosol and molecular extinction and backscatter profiles (Eq. 4.13–4.14 and 4.16–4.17) can be used in the forward model. All profiles are consistent with column integrated values of aerosol extinction (Eq. 2.12) and concentration (Eq. 4.15 and 4.18) which are used in forward model of radiative transfer. If such aerosol properties as concentration profile, AOD and LiDAR ratio are modeled properly, then LiDAR equation (Eq. 4.19) should be able to calculate proper LiDAR signal which agrees with measurements.

New normalization procedure

The only parameter which remains undefined is the LiDAR system factor $K(\lambda)$ (described in Section 2.6.3). This system factor remains constant with height, hence, the shape of the modeled signal coincident with an actual LiDAR signal. Thus, we can only compare the shapes of these signals. The proper comparison of simulated and measured signals can be done for normalized signal as well. If the case, Eq. 4.19 can be written:

$$L(\lambda, z) = \frac{(\beta_{aer}(\lambda, z) + \beta_{mol}(\lambda, z)) \exp \left[-2 \int_{z_1}^{z_2} (\sigma_{mol}(\lambda, z') + \sigma_{aer}(\lambda, z')) dz' \right]}{\int_{z_1}^{z_2} \left[(\beta_{aer}(\lambda, z) + \beta_{mol}(\lambda, z)) \exp \left[-2 \int_{z_1}^{z_2} (\sigma_{mol}(\lambda, z') + \sigma_{aer}(\lambda, z')) dz' \right] \right] dz'} \quad (4.20)$$

During such normalization, $K(\lambda)$ vanished and the shapes of signals remain unchanged. Hence, the normalization allows avoiding the calculation and retrieval of an additional parameter. Moreover, such normalization gives a possibility to automatize the retrieval procedure without checking and selecting the reference altitude. To check if this assumption is correct, retrieval of calibration constant had been left in inversion algorithm. Retrieved calibration constant was chosen to one so that the rightness of the method might be confirmed.

Conclusions and advantages

There are several advantages of such representation:

- The normalization allows avoiding the possible discrepancies of non-optimal reference point selection;
- New normalization procedure excludes additional parameter, $A(\lambda)$, to be retrieved. It reduces the number of parameters to retrieve, and hence, it slightly reduces time of the retrieval and may increase convergence of retrieved and observed parameters;
- Such normalization of LiDAR signal gives a possibility to automatize the retrieval procedure for long-term data retrieval;
- Integration of the atmospheric model into the algorithm gives a consistency with column integrated molecular properties inside the inversion code. Hence, it avoids possible discrepancies that might appear due to the use of different atmospheric models by a user and the implemented in the algorithm. Moreover, users should not precalculate and subtract molecular attenuation by their own. Latitude of an observational site (which already was in input data set) is used for molecular extinction and backscatter profiles calculation.

Consequently, implementation of molecular density profile into the algorithm and implementation of the normalization procedure result in the enhancement of GARRLiC algorithm. Such changes have been successfully implemented into the GARRLiC algorithm and uses for coincident LiDAR and sun/sky-photometer inversions.

Chapter 5

Application of GARRLiC to data of SHADOW-2 (Phase 1) campaign

As was mentioned previously mineral dust has global climate effect. Magnitude and sign of dust RF is strongly depends on a composition and types of particles mixture. Hence, the study of dust mixture and its influences on global radiative balance is very important.

The best way to study influences on RF by some of particles is to make observations in the vicinity to its origin where this type of particles constitutes the majority among the other types. Sahara region is one of the biggest source of dust on the Earth. On the south to the Sahara region (Sub-Saharan Africa and Tropical Africa) the forest wild fires occurs frequently during December – January. Hence, West Africa thanks to atmospheric circulation is the best place to observe dust and biomass burning aerosols. The SHADOW-2 (study of SaHAran Dust Over West Africa) campaign was held at the IRD (Institute for Research and Development) in Mbour, Senegal ($14^{\circ}N$, $17^{\circ}W$). It is performing a multiscale and multilaboratory study (7 laboratories with 18 instruments took part in the campaign) of aerosol properties and dynamics using a set of in situ and remote sensing instruments.

SHADOW-2 campaign consists of two phases. The first phase was focusing on the observation of dust particles (March – April 2015). The second phase, on the observation of biomass burning (December 2015 – January 2016) or biomass burning with dust (different layers or mixture) particles. I was involved during the SHADOW-2, Phase 1 campaign. During one month (from the middle of March to middle of April), I have

operated LILAS instrument. Hence, I have performed all Quality Assurance tests and changes into the system according to various dust loading. These observations are used in two publications. The first one (Bovchaliuk et al., 2016) is presented below and provides a comparison of retrieved aerosol properties using GARRLiC, LIRIC and Regularization algorithms. The second article (Veselovskii et al., 2016), presents retrieval of aerosol optical and physical properties using different Raman and Regularization techniques.

Figure 5.1 presents day averaged AOD values during the SHADOW-2, Phase 1 period. Arrows (orange) indicate dust events at 29 March and 10 April 2015 which are analyzed in Bovchaliuk et al., 2016.

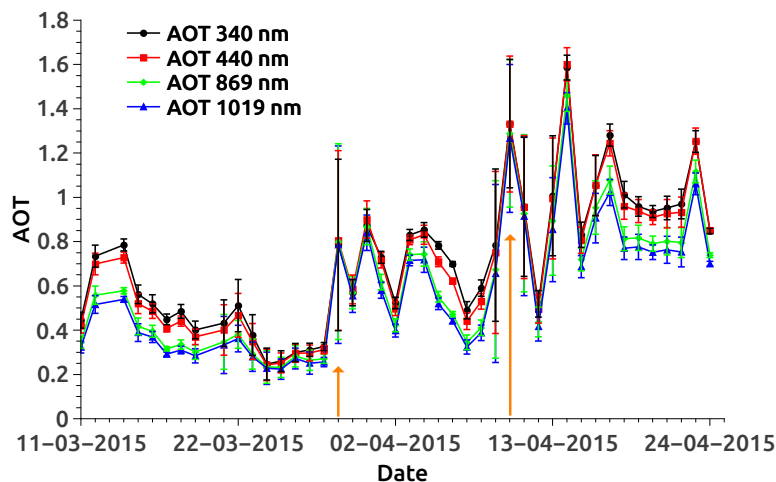


FIGURE 5.1: Day averaged aerosol optical AOD in four wavelengths (1020, 870, 440 and 340 nm) during SHADOW-2 Phase 1. Arrows (orange) indicates AOD values for dust events which are analyzed in Bovchaliuk et al., 2016.

5.1 Comparison between Raman, LIRIC and Regularization retrievals

As it was mentioned above, several methods, techniques, and algorithms can be used to obtain the optical and microphysical characteristics of aerosols. This paper briefly discusses GARRLiC, LIRIC, BASIC and Regularization methods and their results. Methods were applied to some relevant aerosol events during SHADOW-1 campaign (see publication below).



Comparison of aerosol properties retrieved using GARRLiC, LIRIC, and Raman algorithms applied to multi-wavelength lidar and sun/sky-photometer data

Valentyn Bovchaliuk¹, Philippe Goloub¹, Thierry Podvin¹, Igor Veselovskii², Didier Tanre¹, Anatoli Chaikovsky³, Oleg Dubovik¹, Augustin Mortier⁴, Anton Lopatin¹, Mikhail Korenskiy², and Stephane Victori⁵

¹Laboratoire d'Optique Atmosphérique, Lille1 University, Villeneuve d'Ascq, France

²Physics Instrumentation Center of the General Physics Institute, Troitsk, Moscow Region, Russia

³Institute of Physics, NAS of Belarus, Minsk, Belarus

⁴Norwegian Meteorological Institute, Oslo, Norway

⁵Cimel advanced monitoring, Paris, France

Correspondence to: Valentyn Bovchaliuk (bovchaliukv@gmail.com)

Received: 6 February 2016 – Published in Atmos. Meas. Tech. Discuss.: 9 March 2016

Revised: 3 July 2016 – Accepted: 5 July 2016 – Published: 28 July 2016

Abstract. Aerosol particles are important and highly variable components of the terrestrial atmosphere, and they affect both air quality and climate. In order to evaluate their multiple impacts, the most important requirement is to precisely measure their characteristics. Remote sensing technologies such as lidar (light detection and ranging) and sun/sky photometers are powerful tools for determining aerosol optical and microphysical properties. In our work, we applied several methods to joint or separate lidar and sun/sky-photometer data to retrieve aerosol properties. The Raman technique and inversion with regularization use only lidar data. The LIRIC (Lidar-Radiometer Inversion Code) and recently developed GARRLiC (Generalized Aerosol Retrieval from Radiometer and Lidar Combined data) inversion methods use joint lidar and sun/sky-photometer data. This paper presents a comparison and discussion of aerosol optical properties (extinction coefficient profiles and lidar ratios) and microphysical properties (volume concentrations, complex refractive index values, and effective radius values) retrieved using the aforementioned methods. The comparison showed inconsistencies in the retrieved lidar ratios. However, other aerosol properties were found to be generally in close agreement with the AERONET (Aerosol RObotic NETwork) products. In future studies, more cases should be analysed in order to clearly define the peculiarities in our results.

1 Introduction

In situ and remote sensing measurements are the two main approaches used for aerosol observations. The former involves measurements of particles using instruments at the survey points. The latter involves measuring aerosol properties from a distance without direct interaction with particles. Remote sensing methods can be categorized into active and passive depending on the kind of instrument used. Instruments belonging to the passive category measure the modified solar radiation after interactions with particles and terrestrial radiation. One of the most common instruments in this category, a sun/sky photometer, measures both direct and diffuse solar radiation. These data can be used in inversion algorithms (Dubovik and King, 2000; Dubovik et al., 2011) to retrieve several column-integrated aerosol properties such as the aerosol optical depth (AOD), single scattering albedo (SSA), particle size distribution (SD), effective radius (r_{eff}), and complex refractive index (CRI, including real (RRI) and imaginary (IRI) parts of refractive index). Instruments belonging to the active category of remote sensing measurement scattered radiation emitted by themselves; one of the most well-regarded and widely used instrument in this category is lidar (light detection and ranging). Lidar instruments are used for profiling atmospheric variables such as the temperature, pressure, humidity, wind speed and its direction, and the amount of trace gases and aerosols. The main

advantages of lidar measurements include high vertical resolution and applicability during nighttime and in cloudy environments. Current multi-wavelength lidar observations can provide comprehensive and quantitative information regarding aerosol properties (Böckmann et al., 2005; Veselovskii et al., 2015, 2016; Nicolae et al., 2013; Granados-Muñoz et al., 2014).

Several methods, techniques, and algorithms can be used to obtain the optical and microphysical characteristics of aerosols. These methods generally use different sets of data. For instance, AERONET (AERosol RObotic NETwork) inversion code uses only sun/sky-photometer data (Dubovik and King, 2000). Similarly, the Raman technique and regularization algorithm use only lidar data (Ansmann et al., 1990; Weitkamp, 2005; Veselovskii et al., 2002). The LIRIC (Lidar-Radiometer Inversion Code) and GARRLiC (Generalized Aerosol Retrieval from Radiometer and Lidar Combined data) algorithms, in contrast, use both the sun/sky-photometer and lidar data (Lopatin et al., 2013; Chaikovskiy et al., 2016). Because these methods use different datasets, they are applicable during different observational times. For instance, while the Raman technique is most suitable for nighttime observations, sun/sky photometers do not make measurements at that time. Further, the GARRLiC algorithm, which is included in the GRASP (Generalized Retrieval of Atmosphere and Surface Properties) inversion code (Dubovik et al., 2011), can separate the fine and coarse modes of aerosols, thus resulting in the retrieval of particle characteristics separately for both modes. While different methods retrieve different sets of aerosol characteristics, all of them are aimed at obtaining detailed results. The objective of our study is to discriminate and compare the common aerosol characteristics obtained through different methods.

Section 2 describes the observation sites where the measurements were carried out. This section also describes a new lidar system, called LILAS (Lille Lidar AtmosphereS), which was used at the observation sites. Section 3 presents the methods considered in our study and discusses their potential, applicability, and the common aerosol properties that were considered for comparison. Section 4 presents three dust cases that were selected and analysed by using the algorithms described in Sect. 3. The main conclusions and perspectives are given in the last section.

2 Observational sites and the lidar system

The lidar system LILAS used in this work belongs to Laboratoire d'Optique Atmosphérique (LOA). This system is operated at the campus of Lille University, France. The campus area is influenced mainly by urban and industrial pollutant emissions, marine aerosols, and mineral dust and aerosols from volcanic eruptions several times every year (Mortier et al., 2013). Other remote sensing and in situ instruments are also operational at this site. Among them is a lunar pho-

tometer for observing AOD and Ångström exponent (α) values on clear nights within the half moon to full moon lunar phases. LOA is a permanent lidar site. However, for the study of Saharan dust over West Africa (SHADOW2 campaign), LILAS was moved to M'Bour city (Dakar site) in Senegal at the beginning of January 2015. The Dakar site is influenced by mineral dust during March–April and biomass burning during December–January. The two main objectives of the campaign were (i) to record the physical and chemical properties of aerosols over the regions impacted by considerable amounts of dust particles and (ii) to study the aerosol dynamics. Seven laboratories with 18 instruments took part in the campaign.

The LILAS system was assembled and setup in December 2013, and observations started in January 2014. The system is composed of a laser (Spectra-physics, INDI-40) emitting at wavelengths of 1064, 532, and 355 nm (100 mJ/20 Hz), a Newton telescope, a beam rotator, and a receiving module. The beam rotator can be used for near- or far-range observations by changing the overlap function. Several receiving modules were added in April 2014, and the system now consists of five elastic channels (355 and 532 nm both parallel and perpendicular for analog and photo-counting; 1064 nm for total analog) and three Raman channels (387 nm for analog and photo-counting; 408 and 608 nm for photo-counting). During the SHADOW2 campaign, the vibrational Raman channel at 608 nm was changed to a rotational channel at 530 nm. This rotational Raman channel showed a good and stable performance (Veselovskii et al., 2015, 2016). The system can be remotely operated and is coupled with a radar (radio detection and ranging) for reasons such as automatic discontinuation control and airplane safety.

The Lille site became an observation station of the European Aerosol Research Lidar NETwork (EARLINET) in the summer of 2014. The main goal of the network is to provide a comprehensive, quantitative, and statistically significant database on aerosol distributions. The network has some special criteria for data quality assurance, such as a telecover test, a trigger delay, dark measurements, depolarization calibration, and regular check-ups of the Rayleigh fits (Freudenthaler, 2007, 2008, 2010; Freudenthaler et al., 2016). LILAS has passed all the EARLINET tests and check-ups except for depolarization calibration, which is currently in progress.

3 Retrieval algorithms

Depending on the lidar characteristics, different techniques can be used for obtaining optical and microphysical properties of aerosols. All the methods and algorithms that were used for data processing are introduced in this section.

Elastic-backscatter lidar is considered to be a classic form of lidar technology (Weitkamp, 2005). This technology is based on the measurement of elastically scattered light in the backward direction. The common method that derives

aerosol optical characteristics is the Klett method (Klett, 1981, 1985). This method is based on the relationship between the extinction and backscatter coefficients. The algorithm called BASIC (Mortier et al., 2013) based on the Klett method has been developed at LOA and is successfully implemented into routine for mono-wavelength lidar data. This algorithm retrieves an extinction coefficient profile ($\sigma_{\text{aer}}(z)$) following an iterative procedure based on a dichotomy where the lidar ratio (LR) can vary in the range from 10 to 140 sr. The procedure ends when the integral of the extinction profile is close to the AOD measured by a sun/sky photometer within $\Delta\text{AOD} = 0.01$ accuracy.

The Raman lidar technique is a widely known technique in the lidar community for obtaining aerosol optical properties (σ , β , LR) (Ansmann et al., 1990). This technique is based on the scattering of incident lidar light with photon energy shifts due to vibrational or rotational modes of the molecules. It is mostly used at nighttime when the signal-to-noise ratio is the highest, owing to the absence of sunlight scattered into the field of view of the lidar. Assuming that the aerosol extinction coefficient depends on the wavelength through α , the former can be found calculated as (Weitkamp, 2005)

$$\sigma_{\text{aer}}(\lambda_{\text{L}}, z) = \frac{\frac{d}{dz} \left[\ln \frac{N(z)}{z^2 P(z)} \right] - \sigma_{\text{mol}}(\lambda_{\text{L}}, z) - \sigma_{\text{mol}}(\lambda_{\text{R}}, z)}{1 + \left(\frac{\lambda_{\text{L}}}{\lambda_{\text{R}}} \right)^\alpha}, \quad (1)$$

where $P(z)$ is the power received at the Raman wavelength λ_{R} from distance z , $N(z)$ is the molecule number density, $\sigma_{\text{mol}}(\lambda_{\text{L}}, z)$ and $\sigma_{\text{mol}}(\lambda_{\text{R}}, z)$ are the extinction coefficients due to absorption and Rayleigh scattering by atmospheric molecules for emitting lidar and Raman wavelengths, respectively, and α is the Ångström exponent. The aerosol backscatter coefficient can be calculated from the ratio of the elastic signal to Raman signal by using a coefficient determined at a reference point where no aerosol is expected.

A variety of methods can be used to retrieve aerosol microphysical properties using lidar data. They can be divided into three main groups (Weitkamp, 2005). The methods belonging to the first group combine measurements from several instruments that provide enough information to retrieve aerosol microphysical properties. For such methods, the collocation of measurements by different instruments in space and time is necessary. The LIRIC algorithm belongs to this group; it successfully retrieves height-resolved aerosol optical and microphysical properties separately for fine and coarse modes (Chaikovsky et al., 2012, 2016; Wagner et al., 2013; Granados-Muñoz et al., 2014). The algorithm uses AERONET inversion products such as column volume concentration, volume-specific backscatter, and extinction coefficients as a priori information (Chaikovsky et al., 2016). The specific products include backscatter (β), extinction (σ), and volume concentration (V) profiles, Ångström ex-

ponent (α) values, and LR and depolarization (δ) ratios. A deeper synergy between the lidar and sun/sky-photometer data is achieved in the GARRLiC algorithm developed at LOA (Lopatin et al., 2013). GARRLiC inverts the coincident lidar and sun/sky-photometer radiometric data simultaneously. The other marked distinction between GARRLiC and LIRIC is the inversion of two distinct aerosol modes, which makes it possible to retrieve aerosol optical and microphysical properties independently for both the fine and coarse modes. Such differences in the algorithms can influence the results obtained by the two systems. The GARRLiC method is based on the Dubovik inversion code (Dubovik and King, 2000; Dubovik et al., 2011), which has been previously used for processing AERONET data. The synergistic retrieval is expected to improve aerosol retrieval properties; the lidar observations are expected to improve the observations of the columnar properties of aerosols in the backscattering direction, and sun/sky photometers provide information on aerosol properties, such as their amount or type, required for lidar retrievals without making assumptions based on climatological data.

GARRLiC has been designed to provide two independent vertical concentration profiles for the fine and coarse modes of aerosols, since in most cases, aerosols are believed to consist of two modes. However, it works for single mode inversions as well. In such cases, a single value for the total amount of particles is retrieved. The algorithm is quite flexible in this regard; single or double mode inversion can be chosen by the user. Further, single- or multi-wavelength lidar data can be used. In the case of multi-wavelength lidar data, aerosol properties can be retrieved for fine and coarse modes separately or together for the total amount of particles. In the case of single-wavelength lidar data, the aerosol properties can be retrieved only for the total amount of aerosols. Depending on the different configurations of single or double mode inversion employed and the use of single- or multi-wavelength lidar data, different sets of aerosol parameters can be retrieved (see Fig. 1). Spectral information from multiple wavelengths is used to distinguish the contribution of fine and coarse aerosol modes. It should be noted that aerosol events characterized mainly by one type of aerosols or a mixture of particles similar in size (aerosol types are not distinguished inside the mode of particles) should be retrieved by using the configuration of single mode inversion.

As for the second group of methods, optical properties (β and σ profiles) are calculated using Mie theory and are compared with the results obtained by using the Raman technique (Wandinger et al., 1995; Barnaba and Gobbi, 2001). In these methods, aerosol microphysical properties such as SD and CRI are assumed as a priori information. Such methods are used in case of atmospheric layers with single, well-known type of particles. For instance, such methods can characterize the particles of polar stratospheric clouds, volcanic ejecta, and some stratospheric particles. However, owing to the presence of a variety of particles and rapid changes in the atmo-

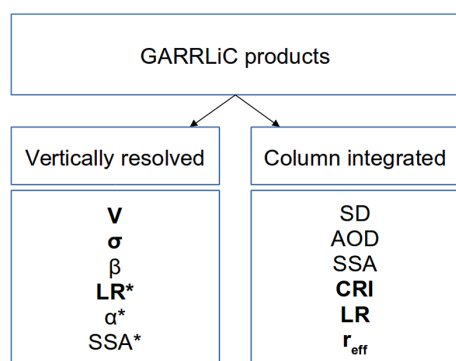


Figure 1. GARRLiC products derived by using single (unmarked) or double (both unmarked and marked *) mode inversion. The latter can be applied only to multi-wavelength lidar data. Common properties, which are compared in this work, retrieved using GARRLiC, LIRIC, and Raman and regularization are indicated by bold font.

spheric conditions, such methods are not applicable to the troposphere.

The third group consists of mathematical approaches that use β and σ coefficient profiles at multiple wavelengths (only lidar measurements). Such methods were developed from the methods of the second group, but they require a lower number of a priori parameters (Müller et al., 1999; Veselovskii et al., 2002, 2004; Shcherbakov, 2007). The algorithm called inversion with regularization developed by (Veselovskii et al., 2002, 2004, 2010b) has also been considered in this work. A simplified set of lidar data (three backscatter (355, 532, and 1064 nm) and two extinction (355 and 532 nm) coefficients – the so-called $3\beta + 2\sigma$ dataset) allows the retrieval of the main aerosol microphysical properties (Veselovskii et al., 2005). Aerosol optical properties that are required for the regularization algorithm can be derived using the Raman technique. The main aerosol microphysical products of the regularization algorithm are the CRI, r_{eff} , number, surface area, and volume concentrations (Veselovskii et al., 2002, 2010b).

These groups of retrieval methods use different types of measurements and, also, different amounts of information. For instance, while regularization uses the $3\beta + 2\sigma$ set of optical data, AERONET uses up to ~ 30 measurements (direct and diffuse almucantar measurements) at each wavelength. Hence, it is important to compare the particle properties retrieved with these methods for these different groups. If different algorithms retrieve similar aerosol properties, it will mean that they are in agreement and can complement each other for data processing during long-term day–night observations.

Aerosol characteristics that are common to LIRIC, GARRLiC, and regularization algorithms are σ , LR, CRI, V , and r_{eff} . The challenging issue here is that no perfectly coincident measurements exist that can be used by these algorithms. The standard Raman technique preferably uses lidar

measurements during nighttime, while the sun/sky photometers require sunlight. Consequently, for a comparison of the retrieved aerosol properties by using the GARRLiC/LIRIC and regularization algorithms, early morning or late evening data under stable atmospheric conditions should be selected. Three events fulfilling these requirements were selected and analysed.

4 Applications

Several dust events were selected from the LILAS measurements over the Lille and Dakar sites. These days had moderate (AOD $\simeq 0.5$ at 440 nm) to high (AOD $\simeq 1.5$ at 440 nm) aerosol loads. Back trajectories (Draxler and Rolph, 2015; Rolph, 2015) and the NMMB/BSC-Dust model (Non-hydrostatic Multiscale/Barcelona Supercomputing Centre Dust model (Pérez et al., 2011; Hausteine et al., 2012) confirmed the origin of mineral dust from Sahara and showed the source locations. In the case of local dust events, the back-trajectory analysis was not used. More details and results of the comparison of each event are presented below.

The AERONET products are presented herein for comparison. As it is used as a priori information for the LIRIC algorithm, the LRs retrieved by LIRIC are presented along with the AERONET characteristics (marked by ** in Tables 2 and 3). Mass concentration profiles were obtained simply by multiplying the volume concentration profiles, V , with the mass density of fine and coarse mode particles. The densities of the fine and coarse modes are 1.5 and 2.6 g cm⁻³, respectively (Biniotoglou et al., 2015; Ansmann et al., 2011, 2012; Hausteine et al., 2012). This density for the coarse mode is also considered in the NMMB/BSC-Dust model.

The GARRLiC and LIRIC algorithms produce uncertainties with the retrieved aerosol properties. For the GARRLiC algorithm, systematic and random errors are presented. For the LIRIC algorithm, only the dispersion of aerosol volume concentration profiles is presented. This work presents only the uncertainties regarding the directly retrieved aerosol properties. Uncertainties on the derived aerosol properties (σ , LR, SSA profiles) are not presented due to their high values as derived by GARRLiC (rough estimations were about 100 % and more). The uncertainties in the volume concentration profiles retrieved using the regularization algorithm are assumed to be about 20 % (Veselovskii et al., 2004, 2005, 2016).

As this work mainly deals with mineral dust sometimes mixed with marine aerosol particles, it will be useful to consider the particle properties obtained from previous studies. According to (Weitkamp, 2005), (Müller et al., 2005), (Müller et al., 2013), (Pitari et al., 2015), and (Dubovik et al., 2002), the typical values of r_{eff} for desert dust vary within the range of 1.2–2.4 μm , and r_{eff} for the coarse mode of sea salt is close to 2.7 μm (Dubovik et al., 2002). The SSA for dust particles increases from 0.80 to 0.99 in the ultraviolet–near-

infrared range (Collaud Coen et al., 2004; Dubovik et al., 2002). The SSA for marine aerosols is high, at ~ 0.98 , and the value remains stable at all wavelengths. The RRI varies from 1.5 to 1.6 for dust particles and is close to 1.36 for marine particles. The IRI decreases from 0.02 to 0.001 in the ultraviolet–near-infrared range for dust particles and is close to 0.001 for marine particles. For Saharan dust, the LR varies within the range of 50–80 sr at a wavelength of 532 nm, and it is significantly lower, at 20–35 sr, for marine particles (Weitkamp, 2005; Müller et al., 2007, 2010; Groß et al., 2011). The depolarization ratio is high, being close to 30–35 % for dust particles, whereas marine particles have a significantly lower δ , i.e. close to 5 % (Freudenthaler et al., 2009; Groß et al., 2011).

4.1 Analysis of a moderate dust event in Lille on 30 March 2014

The dust event detected over Lille on 30 March 2014 was characterized as heavy for Lille site in terms of the aerosol load (AOD 440 nm ≈ 0.52 ; $\alpha \approx 0.27$ for 440/870 nm). The back-trajectory analysis showed that aerosols, which were located in the altitude range of 3 to 6 km, had their origin in the Saharan region (Fig. 2), and aerosols located up to 2 km travelled from south and south-east France. According to lidar measurements, very thin and homogeneous cirrus clouds with negligible effect on AOD were present at 11 km. Cross-examination was done using almucantar sky radiance measurements in order to prevent cloud contamination. The relative deviation between the left/right sky radiance measurements in almucantar geometry was found to be less than 20 %. Cirrus clouds were identified by neither us nor AERONET criteria (Holben et al., 2006); the exact time of the sun/sky-photometer measurements was 07:42 UTC. The NMMB/BSC-Dust model (operated by the Barcelona Supercomputing Center, www.bsc.es/projects/earthscience/NMMB-BSC-DUST/) confirmed dust emissions over Algeria that travelled towards Lille (Fig. 3).

The configuration of LILAS was changed from three channels (355 nm parallel and perpendicular and 532 nm total) to eight channels (355 and 532 nm parallel and perpendicular; 387, 408, 608, and 1064 nm total) in April 2014. Hence, the Saharan dust event could not be analysed by the Raman and regularization algorithms. Unfortunately, depolarization calibration of 355 nm have not been done for the event. Hence, only data at 532 nm channel were used for analysis. LIRIC inversion had not been applied to this event. Consequently, only the GARRLiC and BASIC algorithms were considered in our analysis. Single mode GARRLiC inversions were considered due to only lidar signal at 532 nm. The lidar elevation angle during the measurements was 56° .

Aerosol properties retrieved by the GARRLiC and BASIC algorithms and AERONET products are presented in Table 1 and Figs. 4 and 5. The columnar-integrated GARRLiC SSA values increase with the wavelength, i.e. from

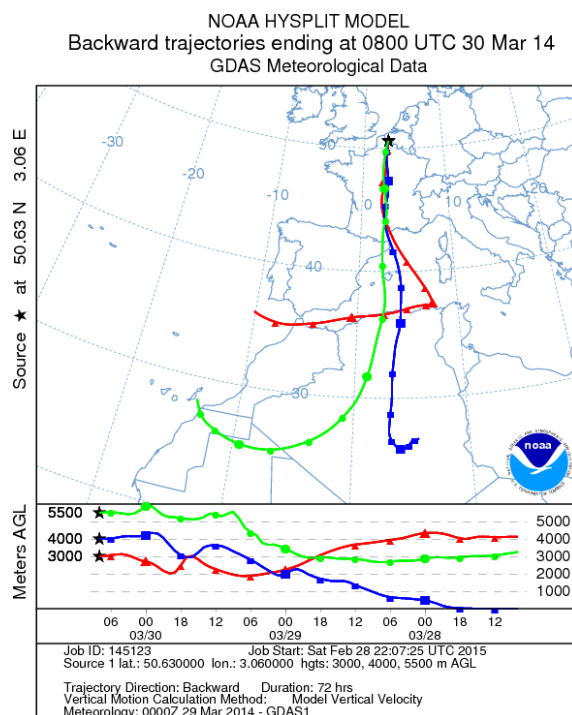


Figure 2. Backward trajectories of air masses observed over Lille during the morning of 30 March 2014.

0.94 ± 0.01 at 440 nm to 0.98 ± 0.01 at 1020 nm. The RRI is close to 1.50 ± 0.02 , the IRI decreases from 0.002 ± 0.001 to 0.001 ± 0.001 . The CRI values retrieved by GARRLiC are in agreement with the AERONET retrievals. The GARRLiC LR values are lower in comparison to the ones retrieved by AERONET at wavelengths of 440 and 532 nm, while they are almost equal at others. The BASIC LR value at 532 nm are close to the value interpolated by AERONET values. The effective radius for the coarse mode of particles is high and is close to $2.0 \mu\text{m}$, and the r_{eff} for the fine mode is close to the value of urban particles.

The size distribution (see Fig. 4) clearly shows the predominance of coarse mode particles with two maxima. The first one with lower radii likely indicates dust particles, and the second one with larger radii also indicates dust particles or can refer to the particles of thin cirrus clouds (Trouillet and Flamant, 1999; Heymsfield and Platt, 1984). The sphericity parameter retrieved by GARRLiC is in agreement with the one from AERONET, both being close to 1 %. The extinction profiles retrieved by BASIC and GARRLiC are close (Fig. 5).

The back-trajectory analysis indicates two layers. This mixture of dust and some fine particles results in lower LR and CRI and higher SSA (at 440 and 532 nm) values than for aerosols from mineral dust only (Balis et al., 2004; Giannakaki et al., 2010; Petzold et al., 2011). Consequently, if the higher layer consisted of mineral dust particles, it is possible to assume that lower aerosol layer with lower LR,

Table 1. Aerosol properties retrieved by GARRLiC, BASIC, and AERONET. The LR values marked by ** were linearly interpolated to lidar wavelength. The abbreviations f, c, and t correspond to fine, coarse, and total aerosol modes, respectively (AOD 440 nm \approx 0.52; $\alpha \approx$ 0.27 for 440/870 nm).

λ (nm)	GARRLiC					BASIC	AERONET		
	r_{eff} (μm)	Sph %	RRI	IRI	LR (sr)	LR (sr)	RRI	IRI	LR (sr)
440			1.50	0.002	53		1.48	0.002	57
532	f: 0.1		1.50	0.002	48	53			52**
675	c: 2.0	1 %	1.51	0.001	43		1.52	0.001	43
870	t: 0.9		1.50	0.001	45		1.51	0.001	43
1020			1.51	0.001	45		1.51	0.001	43

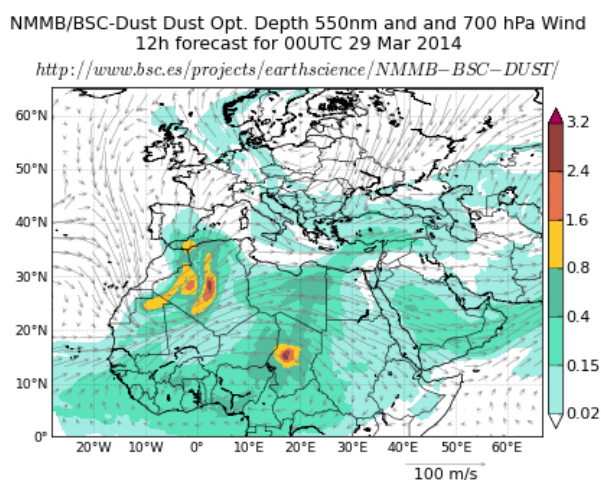


Figure 3. Dust event over Algeria on 29 March 2014.

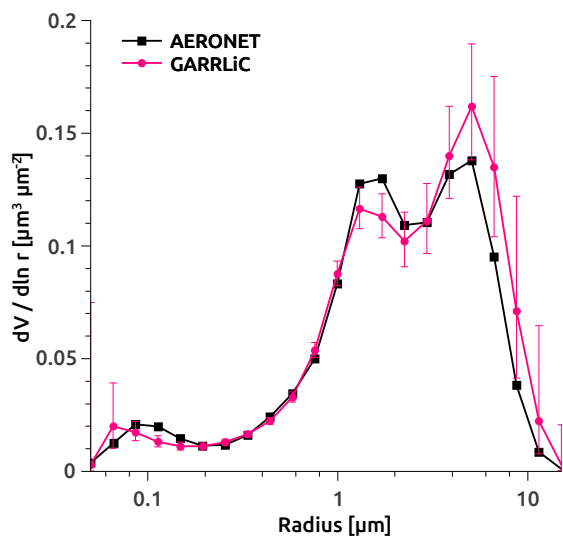


Figure 4. Volume size distribution retrieved by GARRLiC (pink) and AERONET (black) on 30 March 2014 (07:40 UTC) in Lille (AOD 440 nm \approx 0.52; $\alpha \approx$ 0.27 for 440/870 nm).

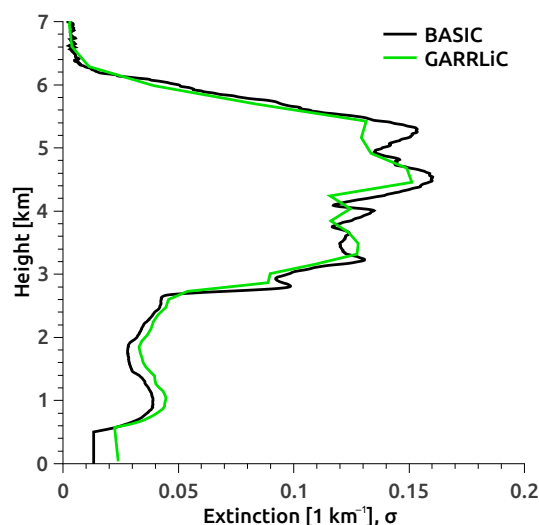


Figure 5. Aerosol extinction profiles at a wavelength 532 nm retrieved by the GARRLiC (green) and the BASIC (black) algorithms for dust event over Lille on 30 March 2014.

CRI, higher SSA and r_{eff} of fine mode close to 0.1 μm would consist of urban particles (Dubovik et al., 2002; Weitkamp, 2005). Unfortunately, no mass concentration profiles could be obtained by the NMMB/BSC-Dust model.

4.2 Analysis of a heavy dust event in Dakar on 29 March 2015

The second event considered in this work was also a dust event, but it occurred over the Dakar site during the SHADOW2 campaign. Three time ranges were selected for the analysis. Daytime data from 15:50 to 19:00 were selected for the Raman technique. For the GARRLiC and LIRIC algorithms, lidar signals were averaged for 20 min at the time of measurement by the sun/sky photometer (16:49 UTC). A third data range was selected for the regularization and Raman methods from 23:30 to 01:10 during nighttime measurements. All aerosols were found in the boundary layer for all time ranges. During the daytime measurements, the altitude of the boundary layer was 2.5 km, and it came down to

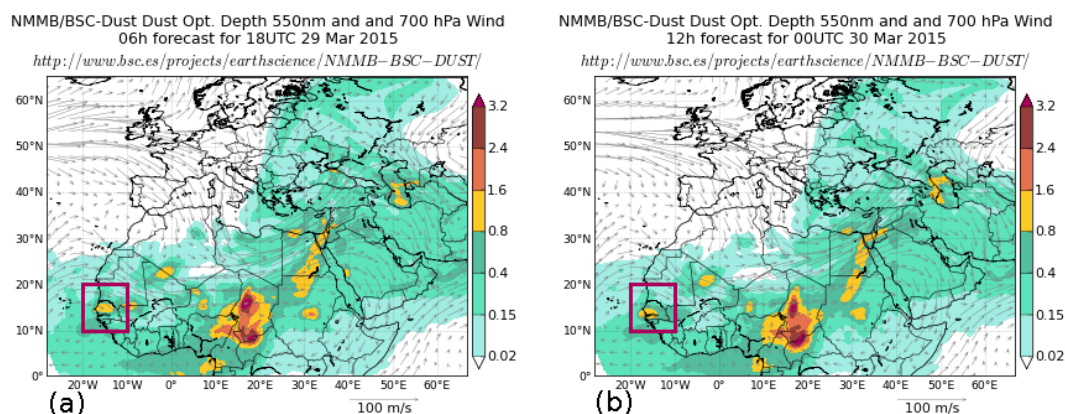


Figure 6. NMMB/BSC-Dust model over Africa and Europe on 29 March 2015. AOD values forecasted by the model ranged from 0.8 to 1.6 at 550 nm. (a) 18:00 UTC, 29 March; (b) 00:00 UTC, 30 March.

2 km at night. The daytime event was characterized by a high aerosol load (AOD 440 nm $\approx 1.35 \pm 0.20$; $\alpha \approx -0.04 \pm 0.01$ for 440/870 nm), and the nighttime event was characterized by a lower aerosol load (AOD 440 nm $\approx 0.83 \pm 0.03$; $\alpha \approx 0.08 \pm 0.02$ for 440/870 nm). The NMMB/BSC-Dust model showed a local dust event over the Dakar site with an AOD range of 0.8–1.6 at the 550 nm wavelength (Fig. 6) for both day- and nighttime measurements. A wind lidar instrument was installed on the site during the SHADOW2 campaign (Wang et al., 2014), and it captured vertically resolved wind speeds and the direction of wind at the site for up to 2 km. The lidar data showed the wind direction to be north–north-east with a speed of 5 to 10 m s⁻¹ in the full altitudinal range for the daytime measurements; the wind direction was north-east with a speed of 10 to 15 m s⁻¹ in the altitudinal range of up to 1.5 km, and lower speeds of 5 to 10 m s⁻¹ were present in upper altitudes for the nighttime measurements. Therefore, while presumably the atmospheric conditions in terms of aerosol types should have remained the same during the event, the aerosol load decreased over the day- to nighttime measurement time frame. Also, the presence of marine particles was not expected because of the lower wind speeds and their northwardly direction during the day.

The aerosol properties retrieved by the GARRLiC and regularization algorithms for the day- and nighttime measurements, respectively, are presented in Table 2.

Single mode GARRLiC inversions were considered and performed in this event because of the huge predominance of coarse mode particles. The effective radius value is high and close to 1.9 during the daytime and decreases to 1.1 μm at night. The RRI values are high, being close to 1.58 ± 0.02 during the daytime measurements; then, values become lower and close to 1.53 ± 0.05 at night. The IRI values decrease from 0.003 ± 0.002 to 0.002 ± 0.001 in the UV–near-infrared range during the daytime and are higher at all wavelengths and close to 0.010 ± 0.005 at night. For both the day and night cases, the Ångström exponent is close to 0. Re-

garding absorption, the SSA values obtained by GARRLiC increase from 0.87 ± 0.02 to 0.97 ± 0.01 in the UV–near-infrared range. The daytime LR values are similar at 532 nm, whereas the ones retrieved by GARRLiC are much lower. The LR values at 355 nm during the daytime measurements differ for all the algorithms, being close to 57, 82, and 37 sr for the Raman, LIRIC, and GARRLiC algorithms, respectively. The Raman LR values slightly increase from ~ 53 to ~ 58 sr at 532 nm, and it significantly increases from ~ 57 to ~ 70 sr at 355 nm over the day- to nighttime measurement time frame. Such a behaviour could be explained by the influence of marine aerosols during daytime. However, the depolarization ratio (Fig. 10) shows that there was at most very little contribution of marine aerosol during daytime. Hence, such a behaviour of retrieved aerosol properties points to inconsistency between the different methods.

It was observed that the IRI, SSA, SD, and r_{eff} retrieved by GARRLiC were in good agreement with AERONET products. However, RRI values and parameter of particle sphericity differed. While the AERONET RRI is equal to 1.53 and the sphericity is equal to 0 %, the RRI retrieved by GARRLiC is close to 1.58 and the sphericity is ~ 20 %. The differences in the LR values are presented in Table 2 and are discussed above.

Figure 7 shows that the SD values obtained from GARRLiC and AERONET are in good agreement. Figure 8 presents the aerosol volume concentrations, V , retrieved with the GARRLiC, LIRIC, and regularization algorithms. Because of the use of single mode inversion by GARRLiC, only the overall V profile was obtained; however, the LIRIC algorithm provided both fine and coarse mode volume concentrations. Because of a high background noise, the regularization algorithm was not applied to daytime measurements; only nighttime V is presented with this algorithm. The GARRLiC and LIRIC volume concentrations are in good agreement. Unfortunately, obtaining close V values using GARRLiC, LIRIC, and regularization algorithms between the day- and

Table 2. Aerosol properties during the dust event over the Dakar site on 29 March 2015. Here and further, the LR values marked by ** were retrieved by using the LIRIC algorithm. Only the values given for all the wavelengths refer to the column-integrated property. Day: AOD 440 nm $\approx 1.35 \pm 0.20$; $\alpha \approx -0.04 \pm 0.01$. Night: AOD 440 nm $\approx 0.83 \pm 0.03$; $\alpha \approx 0.08 \pm 0.02$.

λ (nm)	GARRLiC					AERONET	Raman (day)	Raman and regularization (night)			
	r_{eff} (μm)	Sph %	RRI	IRI	LR (sr)	LR (sr)	LR (sr)	r_{eff} (μm)	RRI	IRI	LR (sr)
355			1.59	0.003	37	82**	~ 57				~ 70
440			1.59	0.003	33	74					
532	f: 0.2		1.59	0.002	28	58**	~ 53				~ 58
675	c: 2.2	20 %	1.58	0.002	25	43		1.1	1.53	0.010	
870	t: 1.9		1.57	0.002	24	37					
1020			1.56	0.002	22	35					
1064			1.56	0.002	22	34**					

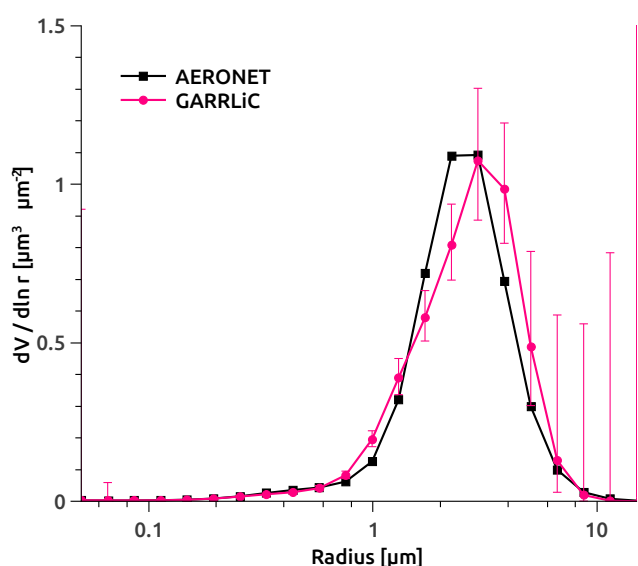


Figure 7. GARRLiC (pink) and AERONET (black) SD on 29 March 2015 (16:49 UTC) over the Dakar site (AOD 440 nm $\approx 1.35 \pm 0.20$; $\alpha \approx -0.04 \pm 0.01$).

nighttime is not possible because of a significant decrease in the AOD values. The relative uncertainty in V obtained from the regularization method was expected to be about 20 %; the GARRLiC and LIRIC uncertainties are plotted in Fig. 8.

The extinction profiles (Fig. 9) at all the wavelengths were found to be in reasonable agreement. The nighttime values of σ are lower in accordance with the lower AOD values. The top boundary of the dust layer decreases from 2.5 km during the day to 2 km at night. The GARRLiC extinction profiles are much smoother because lidar signals were reduced by averaging into 60 points during the data preparation phase. The daytime Raman LR values (Fig. 10) increase with altitude and, therefore, correct σ profiles; however, GARRLiC and LIRIC retrieved only the column-integrated LRs in this case (GARRLiC retrieved vertically resolved LRs in the case of fine and coarse modes inversion). The particle depolar-

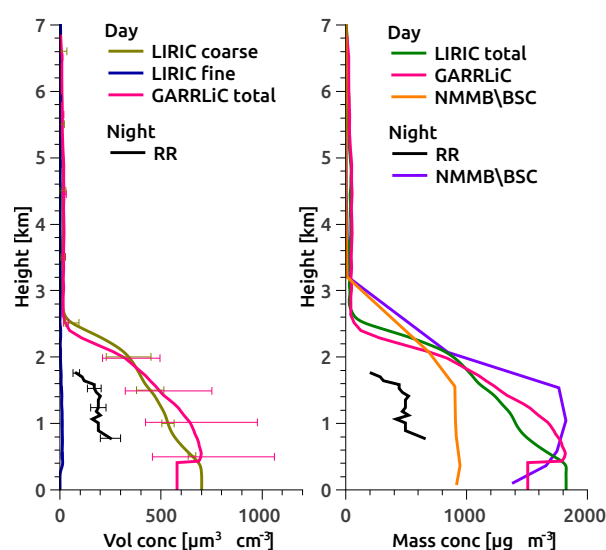


Figure 8. Volume (Vol conc) and mass (Mass conc) concentration profiles for an event over the Dakar site on 29 March 2015. The abbreviation RR corresponds to V retrieved by using Raman and regularization algorithms.

ization, presented in Fig. 10, is lower during daytime (close to 29 %) and higher at nighttime when no marine particles are expected (close to 34 %). These LRs and particle depolarization values are common for mineral dust, especially at nighttime. The r_{eff} profile retrieved by regularization is close to 1.1 μm at the 0.9–1.6 km altitudinal range, and higher values up to 1.4 μm were observed below 0.9 km, whereas lower values close to 0.8 were observed above 1.6 km. The regularization CRI profiles are stable at all altitudes; the averaged values are presented in Table 2 as column-integrated values. The α^{ext} profile for 355/532 nm is close to 0 at all altitudes.

For the comparison with NMMB/BSC-Dust model, the mass concentration profiles were obtained (Fig. 8). To keep the figure clear, uncertainties of mass concentration profiles are not presented. In the case of GARRLiC because of high

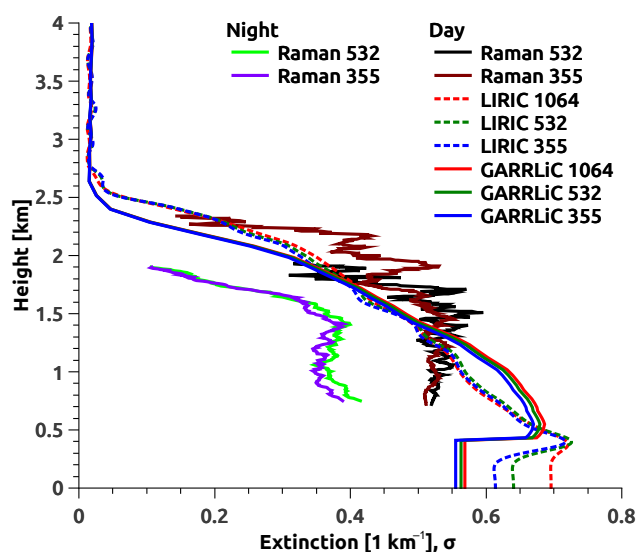


Figure 9. Raman, LIRIC, and GARRLiC extinction profiles during the day (AOD 440 nm $\approx 1.35 \pm 0.20$; $\alpha \approx -0.04 \pm 0.01$) and night (AOD 440 nm $\approx 0.83 \pm 0.03$; $\alpha \approx 0.08 \pm 0.02$) on 29 March 2015.

predominance of coarse aerosol mode, particle density was taken to be equal to 2.6 g cm^{-3} . In the case of LIRIC, both particle densities 1.5 and 2.6 g cm^{-3} were taken for fine and coarse aerosol modes respectively. To keep the figure clear and similar to other parameters, only total LIRIC values are presented in Fig. 8. The mass concentration profiles obtained by GARRLiC and LIRIC algorithms are $1280 \pm 500 \mu\text{g m}^{-3}$ and $1170 \pm 180 \mu\text{g m}^{-3}$ respectively at 1.5 km , which is slightly higher in comparison with the NMMB/BSC-Dust model result ($\sim 900 \mu\text{g m}^{-3}$). The nighttime mass concentration is close to $500 \pm 100 \mu\text{g m}^{-3}$, whereas the modelled value is close to $1700 \mu\text{g m}^{-3}$ at the same altitude of 1.5 km .

4.3 Analysis of a heavy dust event in Dakar on 10 April 2015

The third and the last dust event considered in our study was observed on 10 April 2015 over Dakar (11 days later). Three time ranges were selected for the analysis: the first two during daytime (15:00–19:00 for Raman and 16:01–16:19 for GARRLiC and LIRIC) and the third during nighttime (21:00–04:00 on 11 April 2015 for regularization). The atmospheric conditions were stable, but the height of the aerosol layer containing almost all the aerosols increased from 3 to 4.5 km from the day- to nighttime measurements. The daytime event was characterized by a high aerosol load (AOD 440 nm $\approx 1.53 \pm 0.04$; $\alpha \approx 0.02 \pm 0.01$ for 440/870 nm). Unfortunately, there were no lunar-photometer measurements because of the lunar phase. However, AOD derived by the integration of the σ profile obtained by the Raman method at 532 nm wavelength is equal to 0.83 . It should be noted that such an estimation of AOD does not

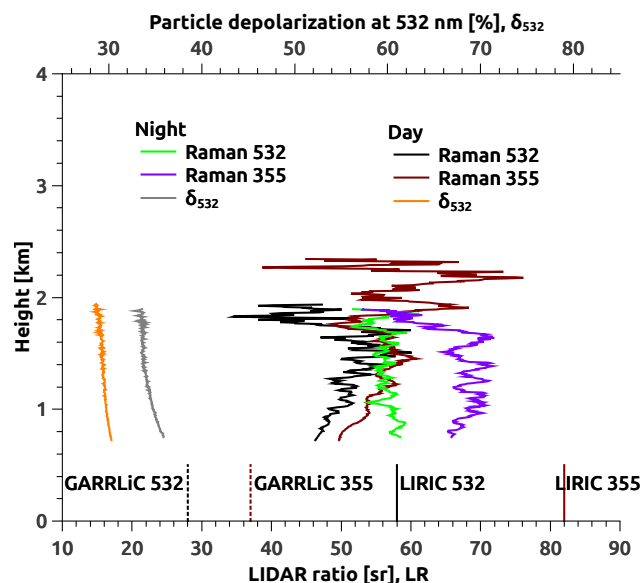


Figure 10. Lidar ratio and depolarization ratio during day- and nighttime measurements for an event on 29 March 2015 over the Dakar site. GARRLiC and LIRIC LR column-integrated values are shown at the beginning of the profiles.

include aerosols located in incomplete overlap zone of lidar. The NMMB/BSC-Dust model forecasted a dust event over the Dakar site with AOD values ranging from 0.8 to 1.6 at 550 nm for both day- and nighttime (Fig. 11). Unfortunately, no measurements could be obtained from the wind lidar. However, a sea breeze was observed at the ground level during daytime measurements. Back-trajectory analysis showed that during the daytime event, the sources of air masses that came to the observational site changed from north (coast of Mauritania) at 0.5 km to east (north-west of Mali) at 2.5 km (Fig. 12). Additionally, during the night, air masses were coming from the northeast direction (Sahara region) at all altitudes. The GARRLiC and Raman plus regularization aerosol retrievals for the day- and nighttime measurements are presented in Table 3.

GARRLiC single mode inversion was used because of the huge predominance of coarse mode particles. As in the previous event, daytime r_{eff} is high and equal to $2.0 \mu\text{m}$, and the value decreases to $0.9 \mu\text{m}$ at night. The daytime column-integrated RRI is close to 1.59 ± 0.02 and stays rather stable at nighttime (1.54 ± 0.06). The IRI slightly decreases during the daytime from 0.004 ± 0.002 to 0.002 ± 0.001 in the UV–near-infrared range and is close to 0.008 ± 0.004 at the nighttime. The GARRLiC SSA increases from 0.85 ± 0.03 to 0.95 ± 0.01 in UV–near-infrared range. The maximum of SD is shifted to higher radii (Fig. 13). However, in general, RRI, IRI, SSA, and SD retrieved by GARRLiC are quite comparable to AERONET values. However, r_{eff} and particle sphericity differ. AERONET r_{eff} is equal to $1.6 \mu\text{m}$ and sphericity

Table 3. Aerosol properties during the dust event over the Dakar site on 10 April 2015. The LR values marked by ** were retrieved by the LIRIC algorithm. Only the values given for all the wavelengths refer to the column-integrated property. Day: AOD 440 nm $\approx 1.53 \pm 0.04$; $\alpha \approx 0.02 \pm 0.01$. Night: AOD 532 nm ≈ 0.83 ; $\alpha \approx 0$ by Raman.

λ (nm)	GARRLiC					AERONET	Raman (day)	Raman and regularization (night)			
	r_{eff} (μm)	Sph %	RRI	IRI	LR (sr)	LR (sr)	LR (sr)	r_{eff} (μm)	RRI	IRI	LR (sr)
355			1.60	0.004	20	70**	~ 25				~ 59
440			1.60	0.003	17	62					
532	f: 0.2		1.60	0.003	14	49**	~ 23				~ 50
675	c: 2.4	57 %	1.60	0.002	13	39		0.9	1.54	0.008	
870	t: 2.0		1.59	0.002	12	32					
1020			1.58	0.002	13	31					
1064			1.58	0.002	13	30**					

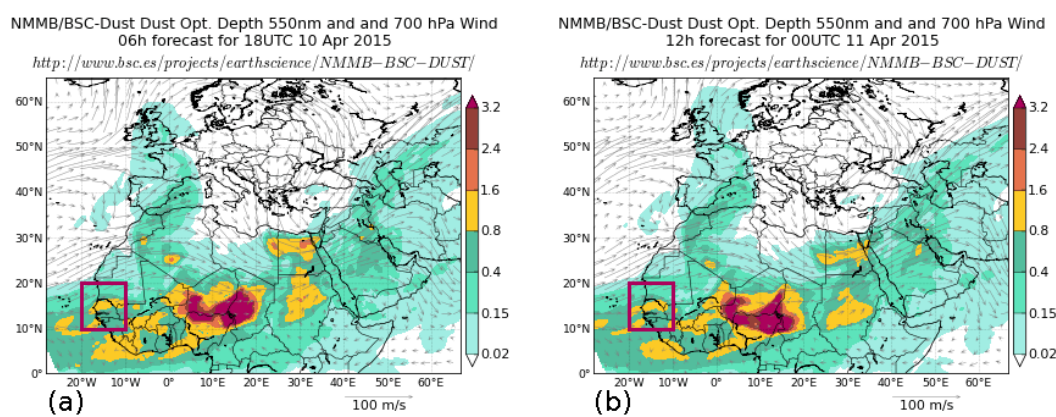


Figure 11. NMMB/BSC-Dust model results over Africa and Europe on 10 April 2015. AOD values forecasted by the model ranged from 0.8 to 1.6 at 550 nm. (a) 18:00 UTC, 10 April; (b) 00:00 UTC, 11 April.

$\sim 0\%$, while the GARRLiC algorithm retrieved $2.0\ \mu\text{m}$ for r_{eff} and 57 % of sphericity particles.

Volume concentration profiles are presented in Fig. 14. Because of different AOD values and altitudes of the boundary layer, day- and nighttime V obtained using different methods are not comparable. The LIRIC and GARRLiC daytime V are different, especially below 2 km, which can be explained by LIRIC usage of both 532 nm parallel and perpendicular signals whereas GARRLiC used total backscattered signal only. However, obtained uncertainties are high and data are overlapped. Extinction profiles (Fig. 15) at all wavelengths are close to each other in respect to the retrieval algorithm. Differences between LRs retrieved by the algorithms are very high, but, nevertheless, σ profiles of different algorithms do not have such high differences. The GARRLiC LRs for 355 and 532 nm are 20 ± 11 and 14 ± 21 respectively. The Raman LR values at 532 nm increase from ~ 23 to ~ 50 sr over the day- to nighttime measurement time frame, and LR at 355 nm also increases from ~ 25 to ~ 59 sr (Fig. 16). Such an increase in LR from day- to nighttime measurements can be explained by the contribution of marine particles during the daytime (i.e. sea-breeze effect). Particle depolarization is lower during daytime (29 %) than during nighttime (32 %).

The Raman α_{ext} profile at 355/532 nm is close to 0 and does not change with altitude (this is not shown in the figures). The profile of the effective radius retrieved with regularization decreases from 1.2 to $0.6\ \mu\text{m}$ at the altitude range of 1–4.5 km. Regularization RRI and IRI profiles remain stable through all altitudes, and column-integrated values, which are presented in Table 3, have been taken as averaged values.

The volume concentration profile at 2 km is much higher during the daytime measurements than the one obtained at night. For comparison with NMMB/BSC-Dust model results, the mass concentration profiles were obtained (Fig. 14). Similar to the previous event, the particle density was taken to be equal to $2.6\ \text{g cm}^{-3}$ according to the NMMB/BSC-Dust model for GARRLiC result. And total LIRIC mass concentration defined as sum of fine and coarse aerosol modes values. The obtained mass concentration profiles at 2 km are close to 1225 ± 400 and $1020 \pm 90\ \mu\text{g m}^{-3}$ for GARRLiC and LIRIC, respectively. This is at least 2 times higher in comparison with the value produced by the NMMB/BSC-Dust model ($\sim 550\ \mu\text{g m}^{-3}$). The calculated Raman nighttime mass concentration ($310 \pm 60\ \mu\text{g m}^{-3}$) shows good agreement with the NMMB/BSC-Dust model ($\sim 300\ \mu\text{g m}^{-3}$) at 2 km.

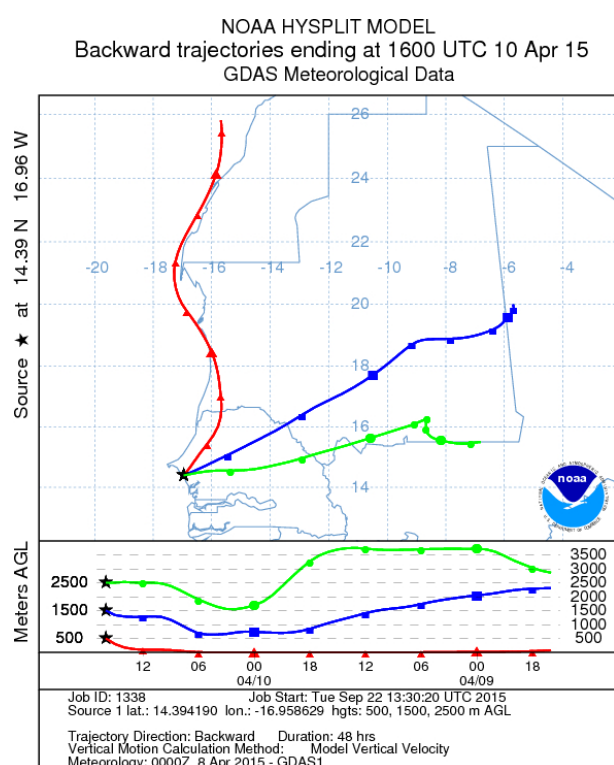


Figure 12. Backward trajectories of air masses for an event over the Dakar site on 10 April 2015.

Raman and GARRLiC daytime LR_s indicate very likely the measurements of marine particles, but at the same time the depolarization ratio indicates at mineral dust. The GARRLiC results are more consistent with mineral dust, but at the same time the retrieved sphericity (57 %) is too high for dust and LR values at all wavelengths are too low.

Such a complex event, which includes several types of particles with similar radii, can cause difficulties in retrieving, interpreting, and comparing the results. The GARRLiC and LIRIC height-resolved aerosol properties are incompatible with the NMMB/BSC-Dust V and Raman σ profiles. That is why, to avoid inconsistencies between the results of different methods, GARRLiC should be only implemented in cases (i) where a single aerosol type is present or (ii) when the investigated aerosols can be separated into two different types of fine and coarse modes.

5 Conclusions

As mentioned previously, the main objective of this article is to compare aerosol properties retrieved by different algorithms. This helps to know to what extent these algorithms can be used in a complementary way for long-term day–night aerosol observations and data processing.

Three dust events were selected from LILAS measurements. The first event over Lille on 30 March 2014 was char-

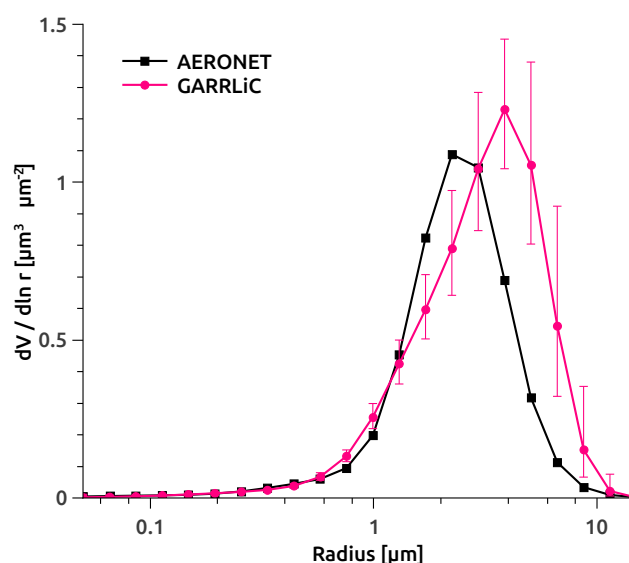


Figure 13. GARRLiC (pink) and AERONET (black) SD for 10 April 2015 (16:11 UTC) over the Dakar site (AOD 440 nm $\approx 1.53 \pm 0.04$; $\alpha \approx 0.02 \pm 0.01$).

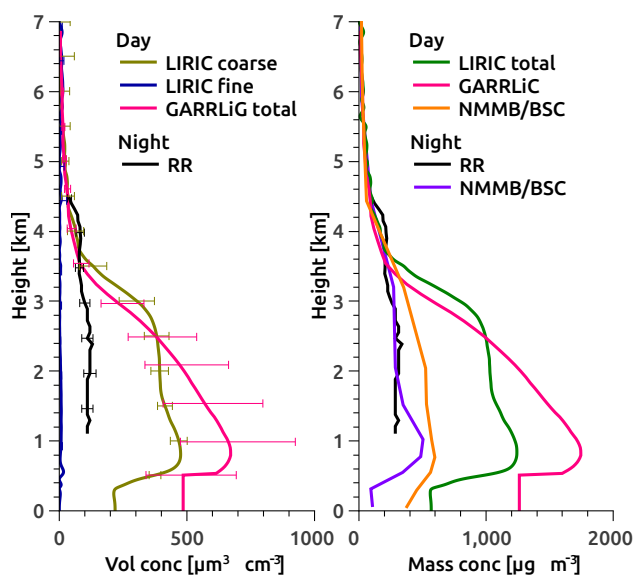


Figure 14. Volume (Vol conc) and mass (Mass conc) concentration profiles for an event over the Dakar site on 10 April 2015. The abbreviation RR corresponds to V retrieved by using Raman and regularization algorithms.

acterized by transported mineral dust particles from the Saharan region. Three different layers of aerosols were observed: (i) assumed urban particles up to 2.5 km, (ii) dust layer in the altitude range of 2.5 to 6 km, and (iii) cirrus clouds with a negligible AOD impact at heights of 11 to 12 km.

The second and third events over Dakar were characterized by a layer consisting of a dust and marine (small contribution) aerosol mixture during the daytime and only dust

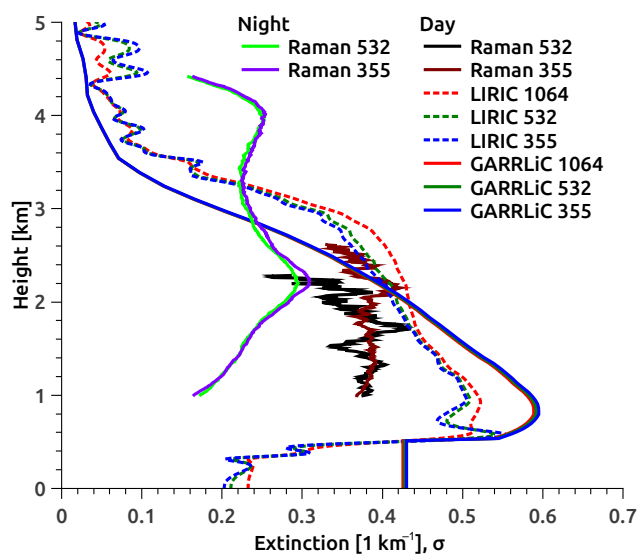


Figure 15. Raman, LIRIC, and GARRLiC extinction profiles during the day ($\text{AOD } 440 \text{ nm} \approx 1.53 \pm 0.04$; $\alpha \approx 0.02 \pm 0.01$) and night ($\text{AOD } 532 \text{ nm} \approx 0.83$; $\alpha \approx 0$ by Raman) on 10 April 2015.

particles during the nighttime. In both cases, AOD values decrease over the day- to nighttime measurement time frame, and, therefore, it was not possible to compare the day- and nighttime σ . GARRLiC, LIRIC, and Raman daytime σ profiles are in agreement on 29 March. However, σ profiles retrieved by the same algorithms on 10 April differ. The latter was a more complex event with different types of particles in the same size range. Development, such as introducing depolarization profile into the GARRLiC algorithm, should enhance the algorithm and make it possible to distinguish aerosols with different shapes inside one mode. In both dust cases, r_{eff} were found to be higher during daytime in comparison with the nighttime cases. Raman LR values increased over the day- to nighttime measurement time frame, which could be caused by the absent of marine particles at night. However, depolarization ratios were always indicative of dust particles. GARRLiC LR values were always lower than the ones obtained by LIRIC and Raman. Also, GARRLiC sphericity was always higher than the one obtained by AERONET. Also, the presence of marine particles should decrease RRI values during the day, but daytime RRI values were higher in comparison with the nighttime ones. However, daytime IRI values were lower in comparison with the ones obtained at night, which agrees with the presence of marine particles, which absorb less than dust particles. These features indicate the challenges in description of optical properties of non-spherical particles in backscattering, on top of possible inconsistencies between the retrieval algorithms used herein. The studies by (Müller et al., 2013), (Wiegner et al., 2009), and (Kokhanovsky, 2015) suggest that the difficulties with reproduction of the observations relate to inaccuracies in the spheroidal model in reproduction of scattering properties in

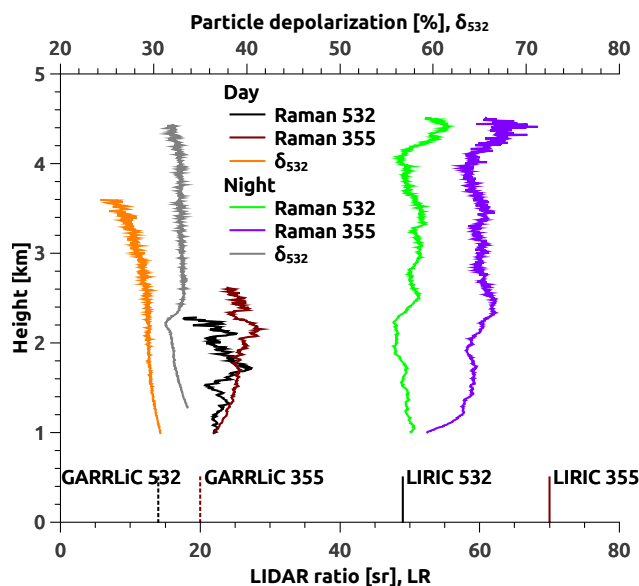


Figure 16. Lidar ratio and depolarization ratio during day- and nighttime measurements for an event on 10 April 2015 over the Dakar site. GARRLiC and LIRIC LR column-integrated values are shown at the beginning of the profiles.

backwards direction. However, those studies are focused on observations of desert dust particle depolarization that were not used in GARRLiC and LIRIC analysis of this study. At the same time, it is worth mentioning that recent research by (Veselovskii et al., 2016) has reported very encouraging agreement of spheroidal model with dust observations. More events should be analysed in order to distinguish the inconsistencies between the algorithms. The second phase of the SHADOW2 campaign will be taking place in December–January 2016.

In future studies, it will be interesting to select morning measurements excluding sea-breeze and marine particles. GARRLiC development (for instance, by incorporating the Raman technique and/or depolarization profile into the code) will make it possible to distinguish vertically resolved aerosol optical properties more accurately, i.e. improved extinction and volume concentration profiles. After such improvements, similar studies should be carried out and, again, the algorithm results should be compared to determine whether they are able to complement each other for long-term day–night measurements.

6 Data availability

AERONET data for Dakar and Lille instrumentation sites are available at <http://aeronet.gsfc.nasa.gov/>. Lidar data available at <http://www-loa.univ-lille1.fr/index.php/observation/lidar.html>.

The Supplement related to this article is available online at doi:10.5194/amt-9-3391-2016-supplement.

Acknowledgements. The research leading to these results has received funding from European Union's Horizon 2020 research and innovation programme under grant agreement no. 654109 within the ACTRIS project. The authors acknowledge Diaollo Aboubacry and Thierno Ndiaye from IRD (Institute pour la Recherche et le Développement) at Mbour, Dakar, Senegal, and the CaPPA project for the its support. The authors acknowledge Sara Basart and the BSC-CNS (Barcelona Supercomputing Center/Centro Nacional de Supercomputación) team for providing modelled dust concentration profiles.

Edited by: V. Amiridis

Reviewed by: three anonymous referees

References

- Ansmann, A., Riebesell, M., and Weitkamp, C.: Measurement of atmospheric aerosol extinction profiles with a Raman lidar, *Opt. Lett.*, 15, 746–748, doi:10.1364/OL.15.000746, 1990.
- Ansmann, A., Tesche, M., Seifert, P., Groß, S., Freudenthaler, V., Apituley, A., Wilson, K. M., Serikov, I., Linné, H., Heinold, B., Hiesch, A., Schnell, F., Schmidt, J., Mattis, I., Wandinger, U., and Wiegner, M.: Ash and fine-mode particle mass profiles from EARLINET-AERONET observations over central Europe after the eruptions of the Eyjafjallajökull volcano in 2010, *J. Geophys. Res.-Atmos.*, 116, d00U02, doi:10.1029/2010JD015567, 2011.
- Ansmann, A., Seifert, P., Tesche, M., and Wandinger, U.: Profiling of fine and coarse particle mass: case studies of Saharan dust and Eyjafjallajökull/Grimsvötn volcanic plumes, *Atmos. Chem. Phys.*, 12, 9399–9415, doi:10.5194/acp-12-9399-2012, 2012.
- Balis, D., Amiridis, V., Nickovic, S., Papayannis, A., and Zerefos, C.: Optical properties of Saharan dust layers as detected by a Raman lidar at Thessaloniki, Greece, *Geophys. Res. Lett.*, 31, doi:10.1029/2004GL019881, 2004.
- Barnaba, F. and Gobbi, G. P.: Lidar estimation of tropospheric aerosol extinction, surface area and volume: Maritime and desert-dust cases, *J. Geophys. Res.-Atmos.*, 106, 3005–3018, doi:10.1029/2000JD900492, 2001.
- Biniotoglou, I., Basart, S., Alados-Arboledas, L., Amiridis, V., Argyrouli, A., Baars, H., Baldasano, J. M., Balis, D., Belegante, L., Bravo-Aranda, J. A., Burlizzi, P., Carrasco, V., Chaikovsky, A., Comerón, A., D'Amico, G., Filioglou, M., Granados-Muñoz, M. J., Guerrero-Rascado, J. L., Ilic, L., Kokkalis, P., Maurizi, A., Mona, L., Monti, F., Muñoz-Porcar, C., Nicolae, D., Papayannis, A., Pappalardo, G., Pejanovic, G., Pereira, S. N., Perrone, M. R., Pietruczuk, A., Posyniak, M., Rocadenbosch, F., Rodríguez-Gómez, A., Sicard, M., Siomos, N., Szkop, A., Tera-dellas, E., Tsekeri, A., Vukovic, A., Wandinger, U., and Wagner, J.: A methodology for investigating dust model performance using synergistic EARLINET/AERONET dust concentration retrievals, *Atmos. Meas. Tech.*, 8, 3577–3600, doi:10.5194/amt-8-3577-2015, 2015.
- Böckmann, C., Mironova, I., Müller, D., Schneidenbach, L., and Nessler, R.: Microphysical aerosol parameters from multiwavelength lidar, *J. Opt. Soc. A*, 22, 518–528, 2005.
- Chaikovsky, A., Dubovik, O., Pappalardo, G., Wandinger, U., Apituley, A., Alados-Arboledas, L., Papayannis, A., and Pietruczuk, A.: Algorithm and Software for the retrieval of vertical aerosol properties using combined Lidar/Radiometer data: dissemination in AERLINET, 339–402, 26th International Laser Radar Conference, 2012, Porto Heli, Greece, 2012.
- Chaikovsky, A., Dubovik, O., Holben, B., Bril, A., Goloub, P., Tanré, D., Pappalardo, G., Wandinger, U., Chaikovskaya, L., Denisov, S., Grudo, J., Lopatin, A., Karol, Y., Lapyonok, T., Amiridis, V., Ansmann, A., Apituley, A., Alados-Arboledas, L., Biniotoglou, I., Boselli, A., D'Amico, G., Freudenthaler, V., Giles, D., Granados-Muñoz, M. J., Kokkalis, P., Nicolae, D., Oschepkov, S., Papayannis, A., Perrone, M. R., Pietruczuk, A., Rocadenbosch, F., Sicard, M., Slutsker, I., Talianu, C., De Tomasi, F., Tsekeri, A., Wagner, J., and Wang, X.: Lidar-Radiometer Inversion Code (LIRIC) for the retrieval of vertical aerosol properties from combined lidar/radiometer data: development and distribution in EARLINET, *Atmos. Meas. Tech.*, 9, 1181–1205, doi:10.5194/amt-9-1181-2016, 2016.
- Collaud Coen, M., Weingartner, E., Schaub, D., Hueglin, C., Corrigan, C., Henning, S., Schwikowski, M., and Baltensperger, U.: Saharan dust events at the Jungfraujoch: detection by wavelength dependence of the single scattering albedo and first climatology analysis, *Atmos. Chem. Phys.*, 4, 2465–2480, doi:10.5194/acp-4-2465-2004, 2004.
- Draxler, R. R. and Rolph, G. D.: HYSPLIT (HYbrid Single-Particle Lagrangian Integrated Trajectory) Model access via NOAA ARL READY Website, available at: <http://ready.arl.noaa.gov/HYSPLIT.php> (last access: July 2016), 2015.
- Dubovik, O. and King, M. D.: A flexible inversion algorithm for retrieval of aerosol optical properties from Sun and sky radiance measurements, *J. Geophys. Res.-Atmos.*, 105, 20673–20696, doi:10.1029/2000JD900282, 2000.
- Dubovik, O., Holben, B., Eck, T. F., Smirnov, A., Kaufman, Y. J., King, M. D., Tanré, D., and Slutsker, I.: Variability of Absorption and Optical Properties of Key Aerosol Types Observed in Worldwide Locations, *J. Atmos. Sci.*, 59, 590–608, doi:10.1175/1520-0469(2002)059<0590:VOAOP>2.0.CO;2, 2002.
- Dubovik, O., Herman, M., Holdak, A., Lapyonok, T., Tanré, D., Deuzé, J. L., Ducos, F., Sinyuk, A., and Lopatin, A.: Statistically optimized inversion algorithm for enhanced retrieval of aerosol properties from spectral multi-angle polarimetric satellite observations, *Atmos. Meas. Tech.*, 4, 975–1018, doi:10.5194/amt-4-975-2011, 2011.
- Freudenthaler, V.: EARLINET-ASOS NA3, Internal LIDAR checkup procedures, Tech. rep., available at: http://www.actris.net/Portals/97/Publications/quality%20standards/lidar/QA-InternalCheckups_version_121017b.pdf (last access: July 2016), 2007.
- Freudenthaler, V.: The telecover test: A quality assurance tool for the optical part of a LIDAR system, available at: http://epub.ub.uni-muenchen.de/12958/1/ILRC24-2008-S01P_30_Freudenthaler_Poster.pdf (last access: July 2016), 2008.
- Freudenthaler, V.: EARLINET Quality Assurance – NA3, available at: [http://www.actris.net/Portals/97/Publications/quality%](http://www.actris.net/Portals/97/Publications/quality%20standards/lidar/QA-InternalCheckups_version_121017b.pdf)

- 20standards/lidar/QA-InternalCheckups_version_121017b.pdf (last access: July 2016), 2010.
- Freudenthaler, V., Böckmann, C., Bösenberg, J., and Pappalardo, G.: European Aerosol Research LIDAR Network – advanced sustainable observation system (EARLINET-ASOS), Plans for quality assurance, available at: <http://www.meteo.physik.uni-muenchen.de/~st212fre/ILRC23/Freudenthaler.pdf>, last access: July 2016.
- Freudenthaler, V., Esselborn, M., Wiegner, M., Heese, B., Tesche, M., Ansmann, A., Müller, D., Althausen, D., Wirth, M., Fix, A., Ehret, G., Knippertz, P., Toledano, C., Gasteiger, J., Garhammer, M., and Seefeldner, M.: Depolarization ratio profiling at several wavelengths in pure Saharan dust during SAMUM 2006, *Tellus B*, 61, 165–179, doi:10.1111/j.1600-0889.2008.00396.x, 2009.
- Goloub, P. and Holben, B.: available at: http://aeronet.gsfc.nasa.gov/cgi-bin/type_one_station_opera_v2_new?site=Lille&nachal=2&level=3&place_code=10, last access: July 2016.
- Goloub, P., Podvin, T., Blarel, L., Veselovskii, I., and Tanre, D.: available at: http://www-loa.univ-lille1.fr/Instruments/lidar/calendriers/newcal_2015_shadows.php, last access: July 2016.
- Giannakaki, E., Balis, D. S., Amiridis, V., and Zerefos, C.: Optical properties of different aerosol types: seven years of combined Raman-elastic backscatter lidar measurements in Thessaloniki, Greece, *Atmos. Meas. Tech.*, 3, 569–578, doi:10.5194/amt-3-569-2010, 2010.
- Granados-Muñoz, M. J., Guerrero-Rascado, J. L., Bravo-Aranda, J. A., Navas-Guzmán, F., Valenzuela, A., Lyamani, H., Chaikovskiy, A., Wandinger, U., Ansmann, A., Dubovik, O., Grudo, J. O., and Alados-Arboledas, L.: Retrieving aerosol microphysical properties by Lidar-Radiometer Inversion Code (LIRIC) for different aerosol types, *J. Geophys. Res.-Atmos.*, 119, 4836–4858, doi:10.1002/2013JD021116, 2014.
- Groß, S., Tesche, M., Freudenthaler, V., Toledano, C., Wiegner, M., Ansmann, A., Althausen, D., and Seefeldner, M.: Characterization of Saharan dust, marine aerosols and mixtures of biomass-burning aerosols and dust by means of multi-wavelength depolarization and Raman lidar measurements during SAMUM 2, *Tellus B*, 63, 706–724, 2011.
- Haustein, K., Pérez, C., Baldasano, J. M., Jorba, O., Basart, S., Miller, R. L., Janjic, Z., Black, T., Nickovic, S., Todd, M. C., Washington, R., Müller, D., Tesche, M., Weinzierl, B., Esselborn, M., and Schladitz, A.: Atmospheric dust modeling from meso to global scales with the online NMMB/BSC-Dust model – Part 2: Experimental campaigns in Northern Africa, *Atmos. Chem. Phys.*, 12, 2933–2958, doi:10.5194/acp-12-2933-2012, 2012.
- Heymsfield, A. J. and Platt, C.: A parameterization of the particle size spectrum of ice clouds in terms of the ambient temperature and the ice water content, *J. Atmos. Sci.*, 41, 846–855, 1984.
- Holben, B. N., Eck, T. F., Slutsker, I., Smirnov, A., Sinyuk, A., Schafer, J., Giles, D., and Dubovik, O.: Aeronet's Version 2.0 quality assurance criteria, *Proc. SPIE*, 6408, 64080Q–64080Q–14, doi:10.1117/12.706524, 2006.
- Klett, J. D.: Stable analytical inversion solution for processing lidar returns, *Appl. Opt.*, 20, 211–220, doi:10.1364/AO.20.000211, 1981.
- Klett, J. D.: Lidar inversion with variable backscatter/extinction ratios, *Appl. Opt.*, 24, 1638–1643, doi:10.1364/AO.24.001638, 1985.
- Kokhanovsky, A. A.: *Light Scattering Reviews 9*, Praxis Publishing, 2015.
- Lopatin, A., Dubovik, O., Chaikovskiy, A., Goloub, P., Lapyonok, T., Tanré, D., and Litvinov, P.: Enhancement of aerosol characterization using synergy of lidar and sun-photometer coincident observations: the GARRLiC algorithm, *Atmos. Meas. Tech.*, 6, 2065–2088, doi:10.5194/amt-6-2065-2013, 2013.
- Mortier, A., Goloub, P., Podvin, T., Deroo, C., Chaikovskiy, A., Ajtai, N., Blarel, L., Tanre, D., and Derimian, Y.: Detection and characterization of volcanic ash plumes over Lille during the Eyjafjallajökull eruption, *Atmos. Chem. Phys.*, 13, 3705–3720, doi:10.5194/acp-13-3705-2013, 2013.
- Müller, D., Wandinger, U., and Ansmann, A.: Microphysical particle parameters from extinction and backscatter lidar data by inversion with regularization: theory, *Appl. Opt.*, 38, 2346–2357, doi:10.1364/AO.38.002346, 1999.
- Müller, D., Mattis, I., Wandinger, U., Ansmann, A., Althausen, D., and Stohl, A.: Raman lidar observations of aged Siberian and Canadian forest fire smoke in the free troposphere over Germany in 2003: Microphysical particle characterization, *J. Geophys. Res.-Atmos.*, 110, d17201, doi:10.1029/2004JD005756, 2005.
- Müller, D., Ansmann, A., Mattis, I., Tesche, M., Wandinger, U., Althausen, D., and Pisani, G.: Aerosol-type-dependent lidar ratios observed with Raman lidar, *J. Geophys. Res.-Atmos.*, 112, d16202, doi:10.1029/2006JD008292, 2007.
- Müller, D., Ansmann, A., Freudenthaler, V., Kandler, K., Toledano, C., Hiebsch, A., Gasteiger, J., Esselborn, M., Tesche, M., Heese, B., Althausen, D., Weinzierl, B., Petzold, A., and von Hoyningen-Huene, W.: Mineral dust observed with AERONET Sun photometer, Raman lidar, and in situ instruments during SAMUM 2006: Shape-dependent particle properties, *J. Geophys. Res.-Atmos.*, 115, d11207, doi:10.1029/2009JD012523, 2010.
- Müller, D., Veselovskii, I., Kolgotin, A., Tesche, M., Ansmann, A., and Dubovik, O.: Vertical profiles of pure dust and mixed smoke-dust plumes inferred from inversion of multiwavelength Raman/polarization lidar data and comparison to AERONET retrievals and in situ observations, *Appl. Opt.*, 52, 3178–3202, doi:10.1364/AO.52.003178, 2013.
- Nicolae, D., Nemuc, A., Müller, D., Talianu, C., Vasilescu, J., Belcigante, L., and Kolgotin, A.: Characterization of fresh and aged biomass burning events using multiwavelength Raman lidar and mass spectrometry, *J. Geophys. Res.-Atmos.*, 118, 2956–2965, 2013.
- Pérez, C., Haustein, K., Janjic, Z., Jorba, O., Huneus, N., Baldasano, J. M., Black, T., Basart, S., Nickovic, S., Miller, R. L., Perlwitz, J. P., Schulz, M., and Thomson, M.: Atmospheric dust modeling from meso to global scales with the online NMMB/BSC-Dust model – Part 1: Model description, annual simulations and evaluation, *Atmos. Chem. Phys.*, 11, 13001–13027, doi:10.5194/acp-11-13001-2011, 2011.
- Petzold, A., Veira, A., Mund, S., Esselborn, M., Kiemle, C., Weinzierl, B., Hamburger, T., Ehret, G., Lieke, K., and Kandler, K.: Mixing of mineral dust with urban pollution aerosol over Dakar (Senegal): impact on dust physico-chemical and radiative properties, *Tellus B*, 63, 619–634, 2011.
- Pitari, G., Di Genova, G., Coppari, E., De Luca, N., Di Carlo, P., Iarlori, M., and Rizi, V.: Desert dust transported over Europe: Lidar observations and model evaluation of the ra-

- diative impact, *J. Geophys. Res.-Atmos.*, 120, 2881–2898, doi:10.1002/2014JD022875, 2015.
- Rolph, G. D.: Real-time Environmental Applications and Display sYstem (READY) Website, available at: <http://ready.arl.noaa.gov> (last access: July 2016), 2015.
- Shcherbakov, V.: Regularized algorithm for Raman lidar data processing, *Appl. Opt.*, 46, 4879–4889, doi:10.1364/AO.46.004879, 2007.
- Trouillet, V. and Flamant, P. H.: Impact of cirrus cloud ice crystal shape and size on multiple scattering effects: application to spaceborne and airborne backscatter lidar measurements during LITE mission and E LITE campaign, *Geophys. Res. Lett.*, 26, 2203–2206, 1999.
- Veselovskii, I., Kolgotin, A., Griaznov, V., Müller, D., Wandinger, U., and Whiteman, D. N.: Inversion with regularization for the retrieval of tropospheric aerosol parameters from multiwavelength lidar sounding, *Appl. Opt.*, 41, 3685–3699, doi:10.1364/AO.41.003685, 2002.
- Veselovskii, I., Kolgotin, A., Griaznov, V., Müller, D., Franke, K., and Whiteman, D. N.: Inversion of multiwavelength Raman lidar data for retrieval of bimodal aerosol size distribution, *Appl. Opt.*, 43, 1180–1195, doi:10.1364/AO.43.001180, 2004.
- Veselovskii, I., Kolgotin, A., Müller, D., and Whiteman, D. N.: Information content of multiwavelength lidar data with respect to microphysical particle properties derived from eigenvalue analysis, *Appl. Opt.*, 44, 5292–5303, doi:10.1364/AO.44.005292, 2005.
- Veselovskii, I., Dubovik, O., Kolgotin, A., Lapyonok, T., Di Girolamo, P., Suma, D., Whiteman, D. N., Mishchenko, M., and Tanré, D.: Demonstration of Aerosol Property Profiling by Multiwavelength Lidar under Varying Relative Humidity Conditions, *J. Geophys. Res.*, 115, 1543–1557, doi:10.1029/2010JD014139, 2010a.
- Veselovskii, I., Dubovik, O., Kolgotin, A., Lapyonok, T., Di Girolamo, P., Summa, D., Whiteman, D. N., Mishchenko, M., and Tanré, D.: Application of randomly oriented spheroids for retrieval of dust particle parameters from multiwavelength lidar measurements, *J. Geophys. Res.-Atmos.*, 115, D21203, doi:10.1029/2010JD014139, 2010b.
- Veselovskii, I., Whiteman, D. N., Korenskiy, M., Suvorina, A., and Pérez-Ramírez, D.: Use of rotational Raman measurements in multiwavelength aerosol lidar for evaluation of particle backscattering and extinction, *Atmos. Meas. Tech.*, 8, 4111–4122, doi:10.5194/amt-8-4111-2015, 2015.
- Veselovskii, I., Goloub, P., Podvin, T., Bovchaliuk, V., Derimian, Y., Augustin, P., Fourmentin, M., Tanre, D., Korenskiy, M., Whiteman, D. N., Diallo, A., Ndiaye, T., Kolgotin, A., and Dubovik, O.: Retrieval of optical and physical properties of African dust from multiwavelength Raman lidar measurements during the SHADOW campaign in Senegal, *Atmos. Chem. Phys.*, 16, 7013–7028, doi:10.5194/acp-16-7013-2016, 2016.
- Wagner, J., Ansmann, A., Wandinger, U., Seifert, P., Schwarz, A., Tesche, M., Chaikovskiy, A., and Dubovik, O.: Evaluation of the Lidar/Radiometer Inversion Code (LIRIC) to determine microphysical properties of volcanic and desert dust, *Atmos. Meas. Tech.*, 6, 1707–1724, doi:10.5194/amt-6-1707-2013, 2013.
- Wandinger, U., Ansmann, A., Reichardt, J., and Deshler, T.: Determination of stratospheric aerosol microphysical properties from independent extinction and backscattering measurements with a Raman lidar, *Appl. Opt.*, 34, 8315–8329, doi:10.1364/AO.34.008315, 1995.
- Wang, Y., Sartelet, K. N., Bocquet, M., Chazette, P., Sicard, M., D’Amico, G., Léon, J. F., Alados-Arboledas, L., Amodeo, A., Augustin, P., Bach, J., Belegante, L., Binietoglou, I., Bush, X., Comerón, A., Delbarre, H., García-Vízcaino, D., Guerrero-Rascado, J. L., Hervo, M., Iarlori, M., Kokkalis, P., Lange, D., Molero, F., Montoux, N., Muñoz, A., Muñoz, C., Nicolae, D., Papayannis, A., Pappalardo, G., Preissler, J., Rizi, V., Rocadenbosch, F., Sellegri, K., Wagner, F., and Dulac, F.: Assimilation of lidar signals: application to aerosol forecasting in the western Mediterranean basin, *Atmos. Chem. Phys.*, 14, 12031–12053, doi:10.5194/acp-14-12031-2014, 2014.
- Weitkamp, C.: Lidar: range-resolved optical remote sensing of the atmosphere, Springer series in optical sciences, 2005.
- Wiegner, M., Gasteiger, J., Kandler, K., Weinzierl, B., Rasp, K., Esselborn, M., Freudenthaler, V., Heese, B., Toledano, C., Tesche, M., and Althausen, D.: Numerical simulations of optical properties of Saharan dust aerosols with emphasis on lidar applications, *Tellus B*, 61, 180–194, 2009.

5.2 Conclusions

The primary objective of the study was to compare aerosol properties retrieved using different algorithms to answer a simple question: can these algorithms be used in a complementary way for long-term day–night aerosol observations and data processing? In other words, do methods provide same results?

Three events have been selected and analyzed. First one over Lille on 30 March 2014 was characterized by transported mineral dust particles from the Saharan region. The second and third events over Dakar were characterized by a layer consisting of a dust and marine (small contribution) aerosol mixture during the day-time and only dust particles during the night-time. In general, comparisons have shown inconsistencies in the retrieved LiDAR ratios. However, other aerosol properties were found to be generally in close agreement with the AERONET products. Inconsistencies indicate the challenges in description of optical properties of non-spherical particles in backscattering (Müller et al., 2013; Wiegner et al., 2009; Kokhanovsky et al., 2015).

In general, GARRLiC development (for instance, by incorporating the Raman technique and/or depolarization profile into the code) will make it possible to distinguish vertically resolved aerosol optical properties more accurately, i.e. improved extinction and volume concentration profiles. After such improvements, similar studies could be done, and, hopefully, the algorithms can be used in a complementary way for long-term day–night aerosol observations and data processing.

Chapter 6

Water vapor mixing ratio profile.

Calibration and application

6.1 Water vapor and Raman LiDAR measurements

The relevance of water vapor observations and modelling were outlined in Chapter 2.5. This chapter presents the results and discussion of two calibration techniques which have been implemented for LILAS measurements.

All LiDAR studies dedicated to water vapor are based on ratio between 408 and 387 nm channels which directly represents water vapor mixing ratio (MR or $w(z)$, Eq. 2.35). Both channels are Raman, hence accumulation and/or averaging of LiDAR signal are frequently used for data analyses. In this work, we discuss two calibration techniques, both use accumulation and LiDAR signal averaging with moving mean procedure. The average with moving mean was applied in such altitude ranges:

- below 1 km height there are no averaging;
- between 1 and 2 km, 2 points ($\sim 11 m$) of LiDAR signals were used for moving mean window;
- between 2 and 4.5 km, 10 points ($\sim 55 m$) were used;
- between 4.5 and 6 km, 24 ($\sim 130 m$) points were used;
- between 6 and 8 km, 50 ($\sim 260 m$) points were used;
- between 8 and 10 km, 120 ($\sim 650 m$) points were used.

Above 10 km, data was not used for water vapor analyses because of weak signals above this altitude. Averaging procedure above 1 km is used by the circumstance that LiDAR observation mainly carried out in some angle ($\sim 47^\circ$) from zenith direction, hence, actual altitudes of measurements are lower, and averaging procedure helps to smooth LiDAR signal at higher altitudes.

Application to real data using obtained calibration constants (Section 6.2) are presented in Section 6.3.

6.2 LiDAR mixing ratio calibration

Herein two calibration techniques are presented. Intercomparison with radiosonde (RS) measurements is a well know method (Leblanc and McDermid, 2008; Navas-Guzmán et al., 2014) which can achieve high accuracy (according to Foth et al., 2015, the uncertainties are at the order of 5%) (Turner and Goldsmith, 1999; Madonna et al., 2011). Such high accuracy can be achieved for stable atmospheric condition (no RS wind drift or it is very slow) and if coincident observations in time and space provided by the instruments. In such cases LiDAR WVMR might be obtained by intercomparison with RS WVMR at predefined altitude ranges. Then, averaged value of calibration constant and its standard deviation can be defined from all values in predefined altitude ranges. In our case, distance between LiDAR and RS sites is close to 120 km for Lille measurements and 70 km for Dakar measurements, such normalization procedure can cause high inconsistencies in lower altitudes where major part of water vapor is located. Better results might be obtained by intercomparison between LILAS and RS mixing ratio in higher altitudes (for instance, from 6 km to 10 km). In such case, differences in lower altitudes caused by distance between observational sites are lower. Nevertheless, the results of such comparison were not satisfactory for the following reasons:

- High uncertainties can be due to small signal to noise ratio, which is frequent for higher altitudes;

- RS can be drifted by the wind in opposite direction to LILAS site, which increases inconsistencies between MR profiles of both instruments;
- MR values at higher altitudes are small, and, hence, defined calibration constant is sensitive to atmospheric variability, this can cause high uncertainties.

Events with good agreement in higher altitudes can be selected manually and analyzed. But, we are more interested in defining an approach routine, which would calculate calibration constant each time when consistent RS and LILAS measurements appear. The procedure for such routine is presented along with calibration method in Section 6.2.1.

The main problem of such type of calibration is caused by the distance between the observational sites of RS and LILAS. The second calibration technique is based on lunar-photometer data. Both, Lille and Dakar sites are equipped with lunar-photometer. It provides total precipitable water content (TPW) for all clear nights for the lunar phases, from half to full moon. The more accurate description is presented in Section 6.2.2.

6.2.1 Intercomparison with radiosonde measurements

The intercomparison was done for the entire of LILAS dataset. Data of the nearest radiosounding stations have been selected for the comparison. In case of Lille, Beauvechain radiosounding observational station in ~ 120 km from LILAS site was taken. In case of Dakar, Dakar station in ~ 70 km from the site was taken.

Comparison has been done under the assumption of equality of total water vapor content measured using radiosonde and LiDAR, variability of N_2 was neglected. Altitude range was selected in respect to have most water vapor content in the column. Hence, several assumptions regarding the altitude range in respect to LiDAR measurements were applied: (i) it should not be lower the altitude where incomplete overlap can be found and (ii) it should not be higher altitudes where low signal to noise ratio can cause high uncertainties. Hence, altitude range from $z_1 = 1$ to $z_2 = 6$ km were chosen. Calibration constant was calculated as follows:

$$C_1 = \frac{\int_{z_1}^{z_2} w^{RS}(z) dz}{\int_{z_1}^{z_2} w_{nc}^L(z) dz} \quad (6.1)$$

where C_1 is the calibration constant (hence it is a ratio of the same values it does not have a unit), w^{RS} is the water vapor mixing ratio measured by radiosonde and w_{nc}^L is the non-calibrated water vapor mixing ratio obtained from LiDAR signal ratio (Eq. 2.50). Integral of MR shows a total abundance of water vapor relative to nitrogen content in some altitude range. Hence, comparison of the same values at different locations we assume an equality of water vapor and N_2 content within predefined altitude range. Such procedure of calibration has shown satisfactory results for obtaining calibration coefficient. Defined C_1 has higher accuracy and temporal stability (Fig. 6.2) than methods discussed in Section 6.2.

More than one hundred (103) simultaneous events were found during two years of LILAS operations. Only 60 events were selected for the analysis, rest of them were rejected by following criteria:

- Midday measurements were rejected because of low LiDAR signal to noise ratio at upper altitudes (17 events);
- LiDAR signals were too noisy at the upper altitudes, mainly caused by the clouds or because of the flash lamp degradation. Criterion which used to identified such events is: signal to noise is less than 1 in the altitude range 5.5 – 6 km (14 events);
- Human/instrumental reason (no measurements from one of the channels, measurement angle were changed during the observations, etc.) (7 events);
- Some RS measurements started only above 3 km, such cases were rejected to avoid small integral values (4 events);

All these criteria have been integrated into computation routine. Therefore calibration coefficients were not calculated for the rejected events. Our results (MR profiles) with uncertainties were stored into files for further usage. Relative uncertainty of obtained C_1 consist from uncertainties of RS and LiDAR measurements. Relative uncertainty of LiDAR measurements was found as a ratio of accumulated value of MR standard deviation to integrated value of mixing ratio. Accumulation of standard deviation

was done at predefined altitude range (from $z_1 = 1$ to $z_2 = 6$ km, due to moving mean procedure) of MR profile. Unfortunately, RS data are provided without highlighted uncertainties, hence, the relative uncertainty of RS measurements is estimated as $\pm 5\%$ (Miloshevich et al., 2009). Total relative uncertainties of w^L profile are assumed equal to relative uncertainties of C_1 .

For instance, Figure 6.1 presents w^L obtained by intercomparison with radiosonde data. Total relative uncertainty equals 23%. Here and below, MR at ground level was calculated using meteorological measurements ($p(z)$, $T(z)$ and RH) at Dakar site according to Eq. 2.36–2.38.

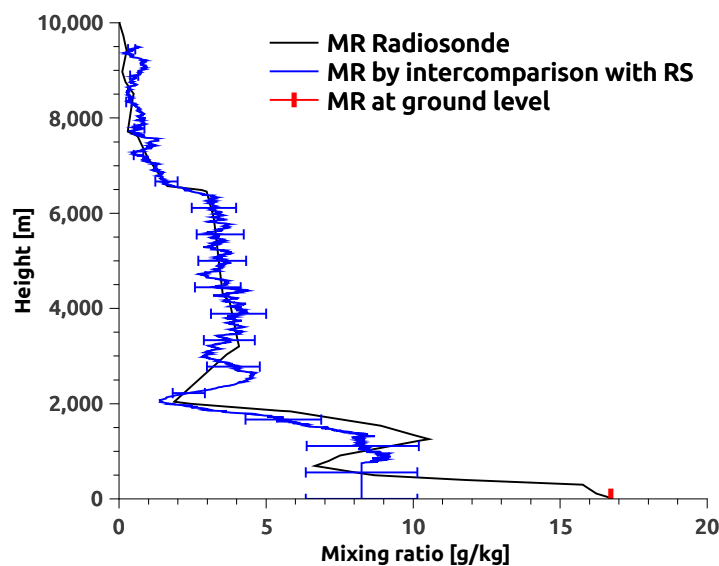


FIGURE 6.1: Mixing ratio profile obtained using intercomparison technique for midnight of 3 June 2015. Blue curve presents calibrated LILAS MR, black curve is radiosonde measurements.

Figure 6.2 presents temporal variability of calibration constants obtained by intercomparison with radiosonde measurements. During the SHADOW-2 campaign (Phase 2, December 2015 – January 2016) improvements in the receiving module for 387 and 408 nm channels were done, the exact period of enhancements is 16–23 of December 2015. 23th December was additionally excluded from the analysis. This moment is represented by black line in the Figure 6.2, dash-dotted lines indicate moments when LILAS was moved between observational sites Lille to Dakar and back. Obtained calibration constants have high uncertainty. It can be due to several reasons:

- Atmosphere spatial variability;

- Low radiosonde spatial resolution in some events might lead to over- or under-estimation of the obtained calibration constant.

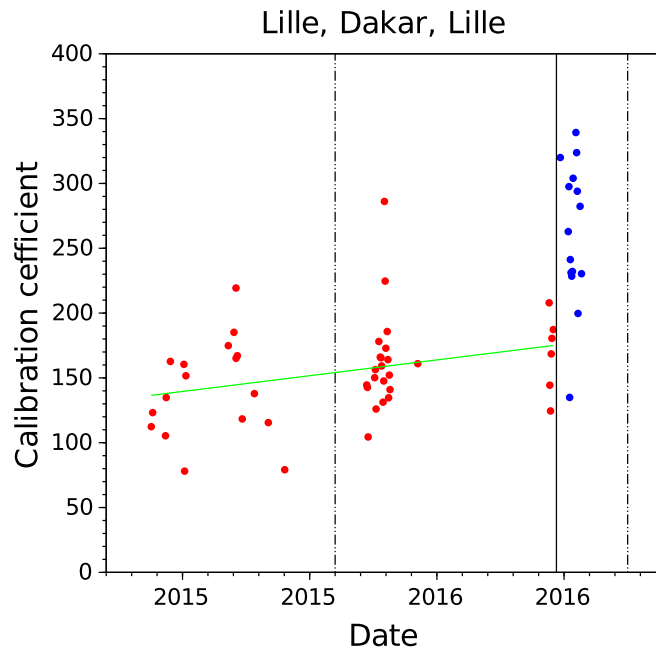


FIGURE 6.2: Calibration constants obtained using intercomparison technique. Dash-dotted lines indicate moments of LiDAR moves between observational sites Lille and Dakar and back. Black line indicates a moment of enhancements in receiving module, red and blue points show calibration constants obtained before and after the enhancements. Green line shows calibration constant drift with time.

Drift of calibration constant has been found for the first period of observations (up to 16 December 2015). The linear fit of the drift was found using a least square method. The equation for the fit can be written as: $C_1 = 25.660 \cdot x - 51555.565$, where x - is decimal year of an event. Residual standard deviation equal 36.577.

There are not enough measurements to repeat similar analysis after improving the receiving modules (23 December 2015 - nowadays). Calibration constant was found as averaged value and it is equal to 261.45 ± 54.80 .

Relative standard deviation of C_1 values equal 23% and 21% respectively for the first and second period of measurements.

6.2.2 Calibration by TWP using lunar-photometer measurements

As was mentioned above, both sites, Lille and Dakar, are equipped with lunar-photometers (LP) which provide TPW for clear nights for the lunar phases, from half to full moon.

Equation 2.34 can be rewritten as:

$$TPW = \frac{1}{g} \int_{z_1}^{z_2} \frac{w(z)}{1 + w(z)} dz \quad (6.2)$$

where $w(z)$ - is mixing ratio, g - is standard acceleration of free fall. As was mentioned above, non-calibrated MR can be directly obtained from the signal ratio of 408 and 387 nm channels. Hence, it can be rewritten:

$$TPW = \frac{C_2}{g} \int_{z_1}^{z_2} \frac{w_{nc}(z)}{1 + w_{nc}(z)} dz \quad (6.3)$$

where $w_{nc}(z)$ - not calibrated mixing ratio profile, C_2 - calibration constant which do not depend on altitudes and can be easily calculated using lunar-photometer TPW data:

$$C_2 = \frac{TPW \cdot g}{\int_{z_1}^{z_2} \frac{w_{nc}(z)}{1 + w_{nc}(z)} dz} \quad (6.4)$$

At the same time, integrands should be equal:

$$\frac{w(z)}{1 + w(z)} = C_2 \frac{w_{nc}(z)}{1 + w_{nc}(z)} \quad (6.5)$$

Now, one can obtain MR as a function of C_2 and w_{nc} as follows:

$$w(z) = \frac{C_2 w_{nc}(z)}{1 + (1 - C_2)w_{nc}} \quad (6.6)$$

The main advantage of this technique is that there are no uncertainties due to the inaccurate integration of radiosonde measurements caused by its low spatial resolution.

Also, in our case, LILAS and lunar-photometer are collocated, hence lower uncertainties could be observed due to the much lower atmosphere spatial variability. Nevertheless, measurements were carried out in a different direction and the incomplete overlap at lower altitudes was present in LiDAR observations. However, the former can be neglected. Overlap functions for both, 387 and 408 nm channels, assumed to be equal above 750 m. Below this altitude water vapor content were assumed to be constant and equal to its value at the altitude of 750 m. Also, water vapor content was neglected above 10km. Hence, altitude range from the surface to 10 km was taken into account for all events.

Temporal resolutions of lunar-photometer and LiDAR measurements are high, one hour averaged data were used for calibration. Hence, for the clear nights maximum 6-12 events can be found depending on a date of year (night duration) and duration of LiDAR observation (not for all nights measurements were carried out during whole nights). For this calibration technique, accumulation of LiDAR signal was decreased to one hour, in comparison to previous one. The same moving mean window procedure was used for the signal averaging. To be consistent with LILAS measurements, lunar-photometer data were averaged in the same time ranges (lunar-photometer provides up to 60 measurements per hour). Among 108 potential events, 71 were selected for calibration. Such criteria were used to reject inappropriate events:

- Events occurred during of the enhancements in receiving module (16-23 December) were excluded from the analysis (20 events);
- Noisy signal in upper altitudes, mainly because of clouds or with flash lamp degradation. Such events were identified by standard deviation of the non-calibrated MR. All events with standard deviation higher than 0.04 were skipped in behalf to keep uncertainties caused due to low signal to noise ratio lower (15 events);
- Human/instrumental reason (no measurements from one of the channels, measurement angle was changed during the observations, etc., 3 events).

It should be mentioned, that the level 1.5 data of lunar-photometer was used. Similarly to sun/sky-photometer observations, these measurements are cloud free. Also, it

should be mentioned, night AOD is produced by AERONET-Europe processing system.

Obtained constants can be divided into two groups. Constants of the first group are obtained during same nights, and the second group consists of constants obtained for different nights. Latter are obtained by averaging all of constants from the first group at each night. It should be mentioned, that calibration constants of the first group have similar undefined water vapor content inside the incomplete overlap function.

Figure 6.3 presents a temporal evolution of the constants (first group) obtained by making use of LP TWP calibration technique. A similar drift of the values were observed for the first period of observations. Linear fit obtained using least square method results in $C_2 = 0.039 \cdot x - 79.141$, residual standard deviation equals 0.013. Like in previous technique, x - is decimal year of an event. To avoid the influences from the number of events occurring during the different nights, the linear fit was obtained using calibration constants from the second group. For the second period of time, linear fit was not analyzed. Averaged calibration constant equals $C_2 = 0.227 \pm 0.037$.

The relative "uncertainties" of C_2 calibration constant result in relative uncertainties of LP and LiDAR measurements. Relative uncertainties of LP were calculated as a ratio of standard deviation of TPW data to its averaged value. The relative uncertainty of LiDAR measurements, like it was done in previous technique, was found as a ratio of accumulated value of standard deviations at selected altitudes (from $z_1 = 750 \text{ m}$ to $z_2 = 10 \text{ km}$, due to moving mean procedure) to integrated value of MR.

For instance, MR obtained using LP TWP calibration technique for 22th December 2015 is presented in Fig. 6.4. Event with high uncertainty (93%) caused by twilight (19:00–20:00 UTC) were chosen.

Relative standard deviation of C_2 values was found to be 10% and 16% respectively for the first and second period of measurements.

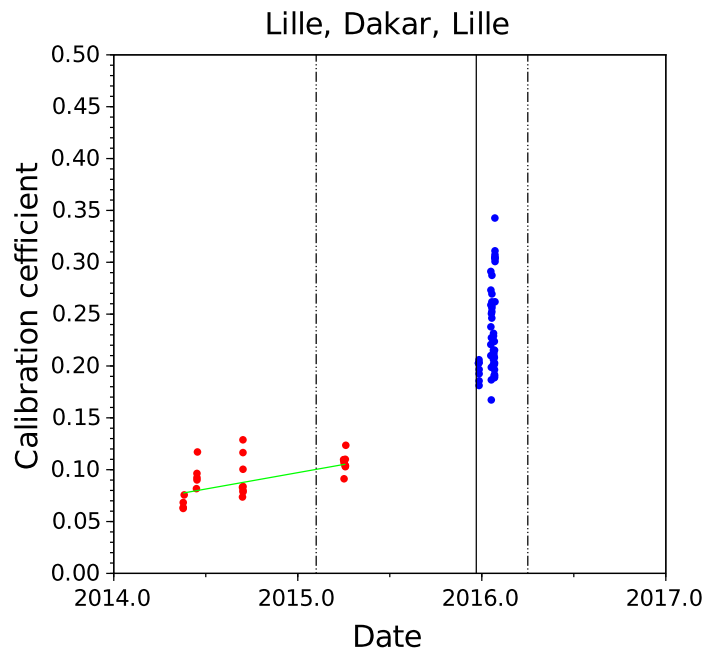


FIGURE 6.3: Calibration constants obtained using LP TPW calibration technique (first group, all C_2 for all nights are presented). Dash-dotted lines indicate moments of LiDAR moves between observational sites Lille to Dakar and back. Black line indicates a moment of enhancements in receiving module, red and blue points show calibration constants obtained before and after the enhancements, green line - linear fit of calibration shift.

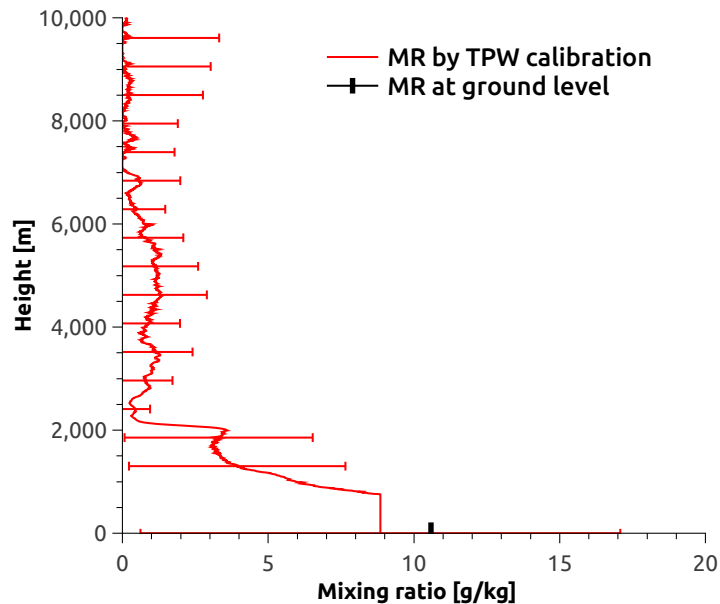


FIGURE 6.4: Mixing ratio profile obtained using LP TWP calibration technique. Observations were carried out during 19:00–20:00 UTC in Dakar, 22 December 2015.

6.2.3 Comparison of obtained calibration constants

Nine events were found to be coincident for both calibration techniques. In Table 6.1 main parameters for both techniques are presented. TPW values were chosen for representation since it can be easily obtained using w_{C_1} (Eq.6.2). Hence, Table 6.1 consists of TPW values obtained from radiosonde and lunar-photometer measurements and TPW calculated from calibrated mixing ratios.

Date	Radiosonding		
	$TPW_{RS} \text{ cm}$	C_1	$TPW_{LILAS} \text{ cm}$
2014.05.16	1.103	$115.7 \pm 18\%$	$1.207 \pm 19\%$
2014.05.18	1.812	$124.6 \pm 15\%$	$1.861 \pm 16\%$
2014.06.13	1.880	$162.7 \pm 25\%$	$1.930 \pm 27\%$
2015.12.25	2.377	$319.1 \pm 27\%$	$2.471 \pm 30\%$
2016.01.18	1.528	$325.6 \pm 20\%$	$1.533 \pm 21\%$
2016.01.19	1.370	$292.6 \pm 17\%$	$1.621 \pm 260\%$
2016.01.20	1.400	$211.1 \pm 35\%$	$1.517 \pm 40\%$
2016.01.23	1.721	$270.8 \pm 20\%$	$1.805 \pm 22\%$
2016.01.25	1.940	$233.2 \pm 22\%$	$3.042 \pm 25\%$
	Lunar-photometer		
	$TPW_{LP} \text{ cm}$	C_2	$TPW_{LILAS} \text{ cm}$
2014.05.16	$1.054 \pm 3\%$	$0.080 \pm 20\%$	$1.054 \pm 20\%$
2014.05.18	$1.626 \pm 5\%$	$0.090 \pm 16\%$	$1.626 \pm 16\%$
2014.06.13	$1.842 \pm 1\%$	$0.130 \pm 39\%$	$1.842 \pm 39\%$
2015.12.25	$2.290 \pm 4\%$	$0.212 \pm 36\%$	$2.290 \pm 36\%$
2016.01.18	$1.527 \pm 15\%$	$0.287 \pm 30\%$	$1.527 \pm 30\%$
2016.01.19	$1.460 \pm 3\%$	$0.273 \pm 20\%$	$1.460 \pm 20\%$
2016.01.20	$1.698 \pm 3\%$	$0.283 \pm 45\%$	$1.698 \pm 45\%$
2016.01.23	$1.756 \pm 2\%$	$0.232 \pm 14\%$	$1.756 \pm 14\%$
2016.01.25	$2.049 \pm 2\%$	$0.222 \pm 16\%$	$2.049 \pm 16\%$

TABLE 6.1: Calibration constants and TPW obtained using calibrated LILAS MR for both calibration techniques. Radiosonde and lunar-photometer TPW are presented for comparison reasons. Relative uncertainties are presented for all values except RS TPW where it is assumed the same and equals 5%.

High value of error on 19 January 2016 for LILAS TPW obtained using intercomparison calibration technique was caused by cloud at 8 km altitude. The cloud was above the site from 22:00 UTC 18 January to 01:00 UTC 19 January. LP TPW calibration technique took the nearest period of LP and LiDAR measurements without cloud (from 1:00 to 2:00 of 19 January). It should be reminded, signal to noise criteria (intercomparison technique) checks last 500 m of calibration altitude range (5.5–6 km). Hence, the cloud was not detected by this criterion and calibration constant was calculated

properly. But TPW calculation includes cloud region, and, hence, produces an error in 260%.

Obtained calibration constants using both calibration techniques have comparable errors. Nevertheless, advantages of LP TWP calibration technique are revealed in the variability of C_2 : standard deviation on C_2 variability are lower than for C_1 . And, as was mentioned above, greater distance between sites shows higher uncertainties. Distance between Lille and Beauvechain is close to 120 km, and decrease in relative uncertainties of C variability equals 14% while decrease in C relative uncertainties equals 5% for Dakar sites with 70 km distance between them.

For instance, Figure 6.5 presents mixing ratio profiles measured by radiosonde and obtained using both calibration techniques are presented.

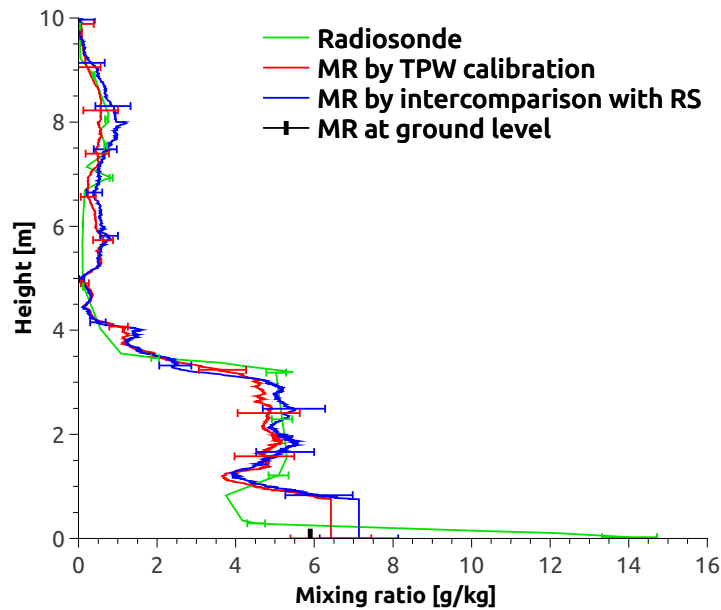


FIGURE 6.5: Mixing ratio profiles obtained by intercomparison with radiosonde (RS, blue) and using TPW measured by lunar-photometer (LP, red), 25 January 2016. Radiosonde mixing ratio presented by green.

6.3 Applications

6.3.1 Application to measurements over Lille site

One event was chosen to present LILAS MR measurements (Fig. 6.6). Three different layers were presented during the night-time measurements on 24–25 November 2014. The highest one started from 23:00 UTC and located between 3–4.5 km. It can be a continentalized maritime trade wind which according to backward trajectory analysis has an oceanic origin (Fig. 6.7). The second level, observed during all night and located between 1500–2200 m, consists of dry air masses which were transported from a Great Britain. This layer has low MR values which are close to ~ 0.1 g/kg. The third layer (below 1500 m) is considered as the boundary layer.

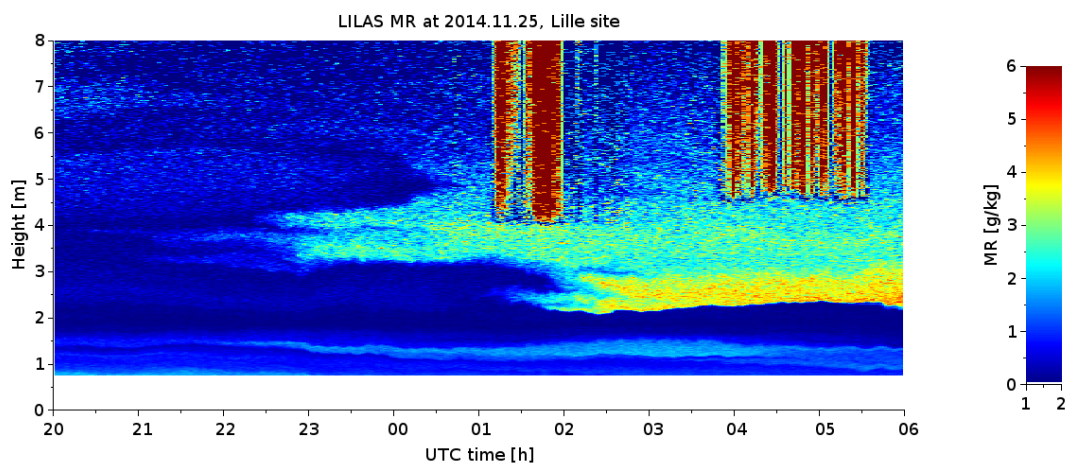


FIGURE 6.6: Height-temporal distribution of LILAS MR (by color) for period of time from 20:00 UTC 24 November to 05:00 UTC 25 November 2014. High values above 4.5 km altitude caused by the clouds.

MR profile is presented in Fig. 6.8, results are averaged over the 02:40–03:40 UTC 25 November 2014 temporal interval. Aerosol amount was very weak (AOD equals 0.1 at 440 nm), hence aerosol optical properties were not calculated.

Height-temporal distribution and averaged profile of MR were obtained using linearly fitted C_2 for 25 November 2014 data.

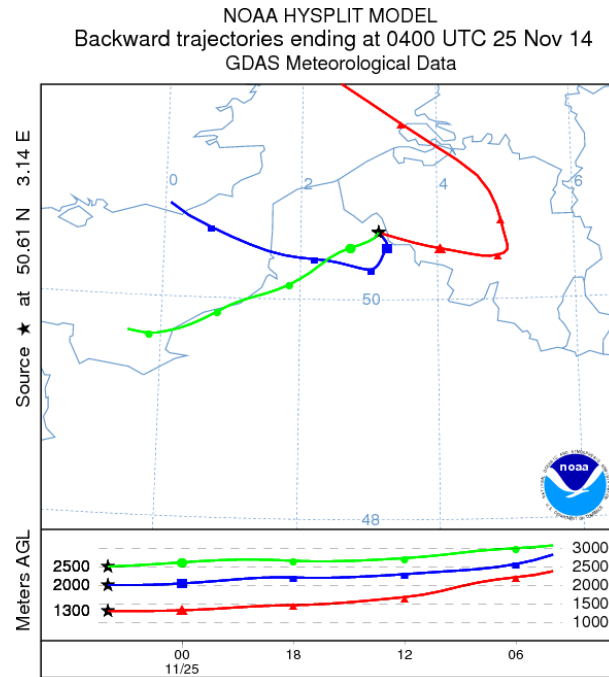


FIGURE 6.7: backward trajectories for the air mass in Lille at altitudes of 1300, 2000, and 2500 m on 25 November 2014 at 04:00 UTC.

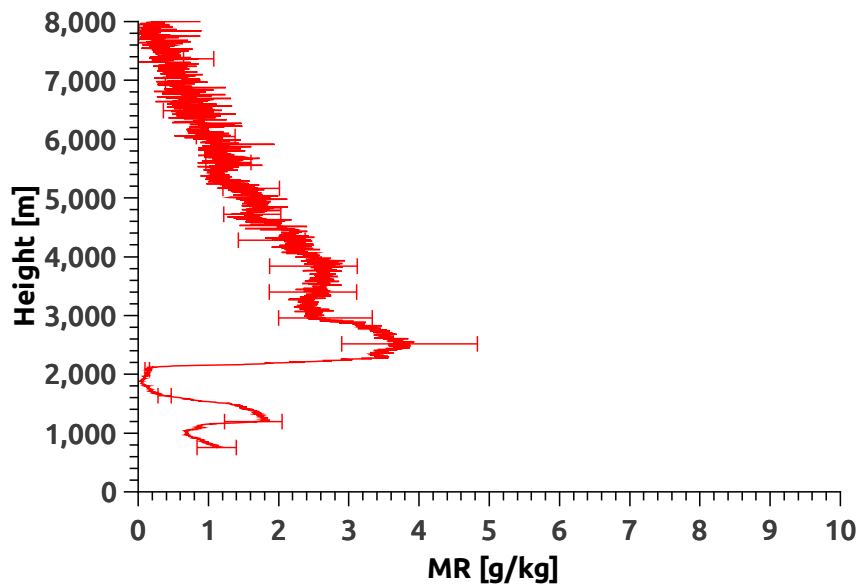


FIGURE 6.8: Vertical profile of water vapor mixing ratio on 25 November 2014. Results are averaged over the 02:40–03:40 UTC temporal interval.

6.3.2 Application to measurements over Dakar site

Many LILAS observational sessions have been done during the Phase 1, SHADOW-2 campaign. Two papers with the results of LILAS measurements have been already

published Bovchaliuk et al., 2016 and Veselovskii et al., 2016. The first article presents an analysis of the aerosol optical and microphysical properties and does not include water vapor analysis (it was presented in Section 5).

The second paper is considering optical and physical properties of the Saharan dust, and includes water vapor analysis. Detailed meteorological characteristics of an observational site is presented for the night 15–16 April 2015. Same night have been chosen in order to compare MR results obtained using intercomparison at higher altitudes (from the paper) with ones obtained using LP TWP calibration technique (described in Section 6.2.2).

For the period from 23:00 to 07:00 UTC on 15–16 April 2015 night, the height–temporal distribution of the extinction at 532 nm, particle depolarization, mixing ratio and LiDAR ratio are presented in Fig. 6.9. During the campaign, the wind field within the lower troposphere (< 5 km) was measured by an eye-safe scanning wind lidar (Windcube).

According to Veselovskii et al., 2016 four different layers were presented during this observational period:

- First one (indicated as Layer A in Fig. 6.9), located between 1 and 3 km (at 00:00 UTC), is associated with a slow northerly wind speed (< 5 ms^{-1}) in the lower part of the layer, and a slightly faster easterly wind speed (> 5 ms^{-1}) above 2 km. This layer was considered to be a continentalized maritime trade wind which is one of oceanic origin that has been progressively altered by continental trade (CT in Fig. 6.9). Backward trajectories are shown in Fig. 6.10. Therefore, this layer was characterized by a mixture of maritime and continental air;
- The second one, located between 0.4 and 0.8 km, rises at the beginning of the period up to 0.7–1 km by the end of the period. This layer is characterized by high aerosol loading and northeasterly winds. According to the backward trajectories, this air mass was transported from a continental area (Mali) and was mainly advected by a southeasterly continental wind. It is well seen starting from 03:00 UTC (layer B in Fig. 6.9)

- The third one, is a nocturnal low-level jet (LLJ). The jet core height is between 250 and 400 m with a maximum jet speed exceeding 15m.s^{-1} . The LLJ was observed throughout the night with a thickness that progressively increased with time, perhaps being the causative mechanism for the corresponding increase in height of the second layer;
- The discontinuity of the fourth layer which is approximately 0.2–0.3 m indicates to the boundary layer (Seibert et al., 2000). It is not shown, but it is characterized by high LiDAR signal values and by small northerly or northwesterly wind speed ($< 5\text{m.s}^{-1}$).

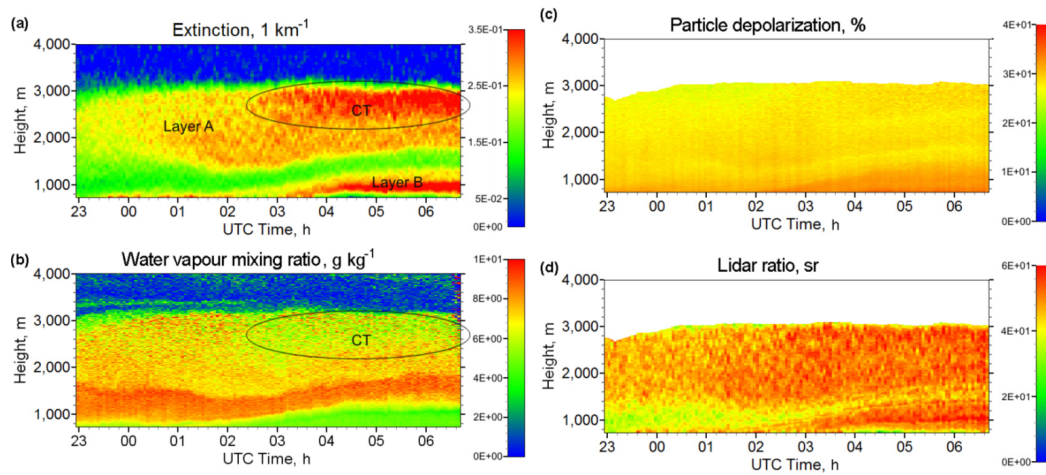


FIGURE 6.9: Height-temporal distribution of (a) AOT at 532 nm, (b) mixing ratio, (c) particle depolarization, and (d) LiDAR ratio over Dakar on 15–16 March 2015. Taken from Veselovskii et al., 2016.

Height-temporal distribution of mixing ratio were derived using intercomparison calibration technique at higher altitudes and in Fig. 6.11 MR using LP TWP calibration technique (C_1 were defined from linear fit) is presented. The particle extinction coefficient σ at 532 nm in layer A increases after 03:00 UTC while w is decreasing in all altitudes. This may indicate that continental air-mass advected by continental trade has become dominant. Particles associated with continental trade has LR at 532 nm close to 55 sr while for continental-maritime particles as observed during the first part of the observation period, it is lower (about 45 sr). Layer A has δ at 532 nm close to 30% and depolarization ratio increases up to 35% for layer B. Should be mentioned, that for the air masses which were considered as continentalized maritime the particle depolarization ratio is in excess of 25%, implying a significant amount of dust even in

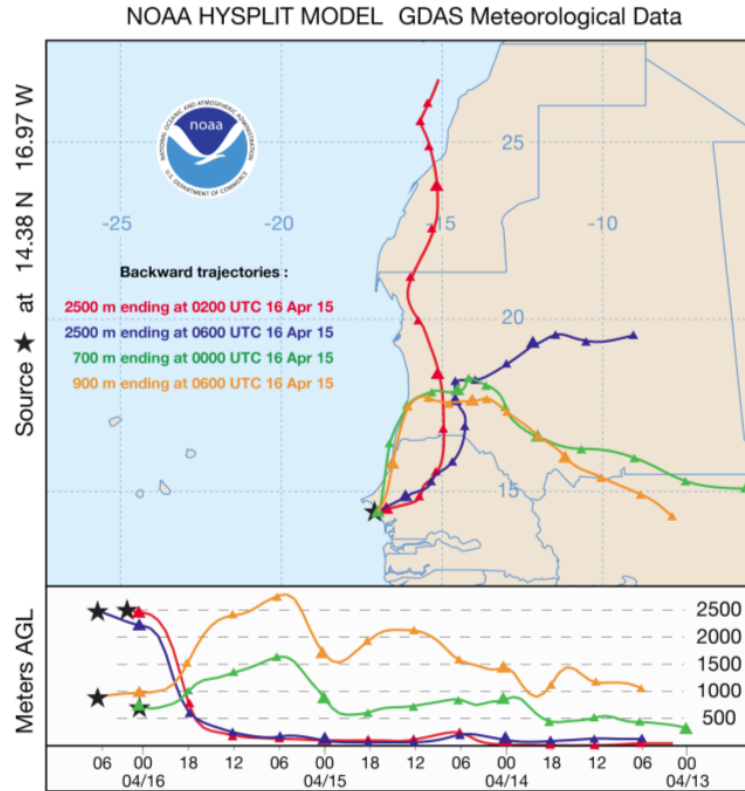


FIGURE 6.10: Back trajectories of the air masses ending in Mbour on 16 April 2015 at 2500 m (02:00 and 06:00 UTC), 700 m (00:00 UTC), and 900 m (06:00 UTC). The first two back trajectories correspond layer A from Fig. 6.9, while the last two back trajectories correspond layer B from the same figure. Taken from (Veselovskii et al., 2016).

this layer.

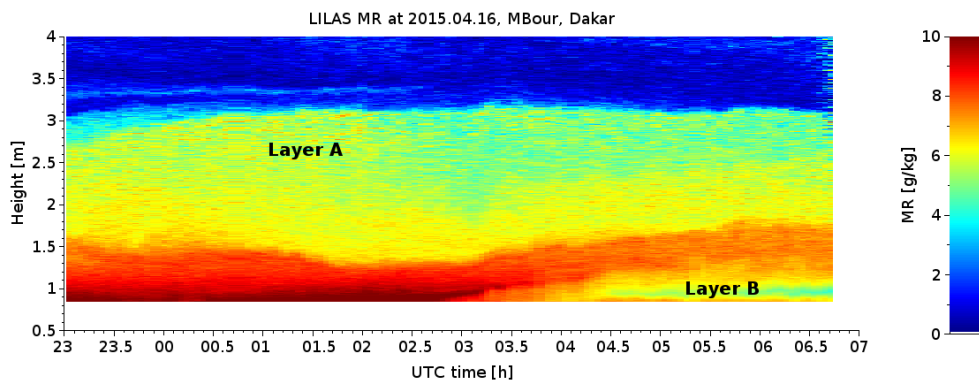


FIGURE 6.11: Height–temporal distribution of LILAS MR (by color) for period of time from 23:00 UTC 15 March to 06:30 UTC 16 March 2015. MR was obtained using linearly fitted value of C_2 for 16 March 2015. Scale of MR was selected the same as in Fig. 6.9.

MR vertical profile averaged over the period 05:00–06:00 UTC is presented in Fig. 6.12. It shows that layer B contains continental air mass (at 1 km MR close to 5 g kg^{-1}). MR

in Layer A is in range $5\text{--}8\text{ g kg}^{-1}$ with lower values ($5\text{--}6\text{ g kg}^{-1}$) at altitude range 2–3 km where continental trade was progressively altered into continentalized maritime trade, and with higher values ($7\text{--}8\text{ g kg}^{-1}$) at altitude range 1.2–1.8 km caused by mix of continental trade particles with marine particles.

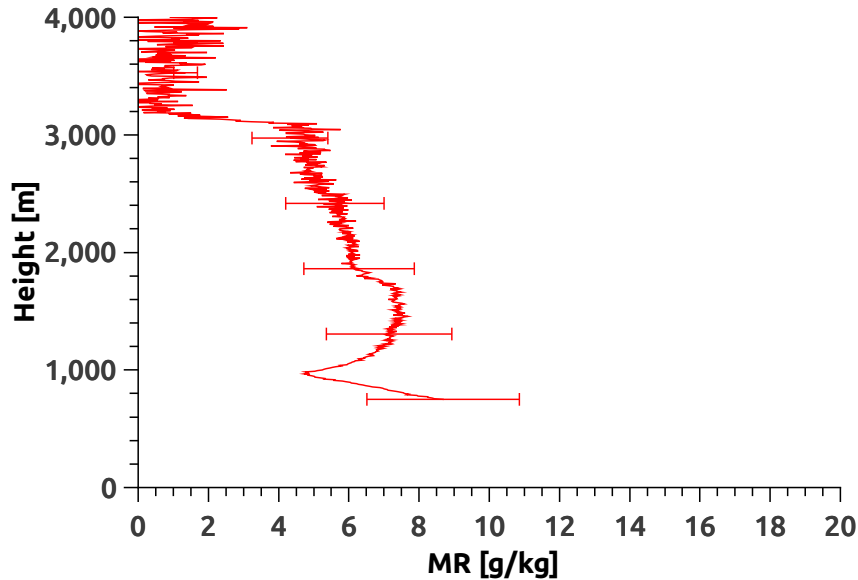


FIGURE 6.12: Vertical profile of water vapor mixing ratio on 16 April 2015. Results are averaged over the 05:00–06:00 UTC temporal interval.

6.4 Conclusions

Two calibration techniques were presented and analyzed. Both showed similar results and comparable uncertainties. The latter is mainly caused by the accumulative error due to larger altitude range which has been selected for deriving calibration constant. Nevertheless, lunar-photometer TPW calibration technique has advantages because both instruments are placed at the same sites. This evinced in lower variability of calibration constant. Hence, it will bring lower uncertainties (20–30%) for events within two or more calibration events. In such case interpolation of C_1 will have lower uncertainties. That is why calibration constant obtained using LP TPW calibration techniques were used in both cases in application section. Main disadvantages of such calibration method caused by the altitude restriction of LiDAR measurements. Neglecting the water vapor content above 10 km and using the assumption of equality of

water vapor below 0.75 km can bring under- or overestimation of MR profile. Additional measurements of MR in incomplete overlap range should be made to enhance this calibration technique. For instance, MR at ground level can be added to the calibration technique to define more accurately MR profile.

Application section has shown that water vapor can be used as a convenient tracer to separate dry continental air masses from oceanic air masses. The latter one is characterized by higher vapor content which is distinctly seen in both examples.

Chapter 7

Conclusions and perspectives

This work is contributing to the improvement of our knowledge of aerosols properties, especially their vertical distribution, thanks to an innovating synergetic approach combining primary measurements of sun/sky-photometer and multi-wavelength Raman LiDAR. Our efforts are part of ambitious European (ACTRIS), national (CaPPA) and regional (CPER CLIMIBIO) activities. In this thesis, efforts have covered several complementary aspects summarized hereinafter.

First of all, instrumental efforts have been devoted to the characterization of LILAS (the new French multi-wavelength Raman polarized LiDAR) set up at the Lille atmospheric platform. Since 2005, LOA is developing expertise in micro-LiDAR (CAML) technologies in cooperation with CIMEL SME. This single wavelength micro-LiDAR is routinely operated, however, the amount of height-resolved information is limited to the vertical distribution of aerosols extinction coefficient and effective LiDAR ratio. Thanks to a fruitful cooperation between Physics Instrumentation Center of General Physics Institute (Russia), CIMEL (Paris) and LOA (Lille), a multi-wavelength Raman polarized LiDAR has been designed and built. This new system is offering an important step forwards to investigate regional aerosols more precisely. Additionally, LILAS being transportable, can joint field campaigns like during SHADOW-2, in Africa. An important contribution has been focused on the data quality assurance. Thanks to EARLINET/ACTRIS protocols and recommendations (Lille is now part of that network and recently started data submission) and thanks to networking activities performed within ACTRIS-1/2, we improved the instrument characterization, data quality and data pre-processing and preparation. In 2016, rotational Raman

channel has been introduced (Veselovskii et al., 2015). This modification is improving Raman signals and the associated retrievals during night-time and day-time as illustrated during the SHADOW-2 campaign. During the thesis, several improvements of LILAS technical environment have been introduced, especially several devices were set up to enable remote control of LILAS when the operator is not in the laboratory. This was requested to maximize the amount of observations.

A second effort was made on the observation side, with the frequent operation of LILAS in various atmospheric situations both in Lille and Dakar sites. During the thesis, we operated LILAS continuously during more than one month at IRD Center, Senegal, in various atmospheric situations. Despite the difficult local conditions (warm, dust, humidity, insects, etc) we have obtained a very valuable data set, partly analyzed by Bovchaliuk et al., 2016; Veselovskii et al., 2016.

This new observational capability is extremely valuable for Haut-de-France region since this region is affected by local pollution but also by transported anthropogenic (Belgium, The Netherlands, Germany, Poland, even Canada) and natural aerosols (Sahara, Canada, Southern Europe). The observation effort has therefore also contributed to ORAURE/ATMOS/ACTRIS-FR database located at AERIS/ICARE Data Processing Center. LILAS is a unique operational system devoted to tropospheric aerosols, water vapor and cirrus observations. SIRTa observation, close to Paris, is developing a similar system that would start the operational phase in 2017.

Finally, important efforts have been made in the aerosol retrieval with the improvement and use of GARRLiC/GRASP algorithm. On the algorithmic side, several improvements were introduced into GARRLiC retrieval preparation procedure. For example, a normalization procedure simplifying the data preparation and enabling more automation of the retrieval has been addressed and defined. Several aerosols events detected both at Lille and Dakar sites have been analyzed and published (Bovchaliuk et al., 2016; Veselovskii et al., 2016). Comparisons of aerosol optical and microphysical properties retrieved by different algorithms (LIRIC, GARRLiC, BASIC, Raman+Regularization) have been performed and analyzed. Aerosol column integrated properties were found to be generally in close agreement with AERONET standard

products. However, some differences were found for derived LiDAR ratio and complex refractive index. These issues are widely discussed within the scientific community and may be linked to the limit of the spheroidal model to explain the scattering properties in the backward direction. Development of the forward model for particles scattering in backward direction is needed, especially for the polarized light which is widely used for non-spherical particle detection and characterization.

Since the interpretation of retrieved aerosol properties and their time evolution can be linked to the atmospheric humidity, the retrieval of water vapor mixing ratio profile is quite relevant and has therefore been addressed in our work. Water vapor can be used as a convenient tracer to separate dry continental air masses from oceanic air masses. The latter is characterized by higher vapor content that was distinctly seen from the LILAS data (use of 408 nm water vapor Raman channel). Two different techniques were used to calibrate LILAS. The first standard technique is the direct comparison with close in time and space radiosounding. In our work, we propose a new method that has been tested and first results are presented. Since Raman channel used for water vapor mixing ratio profiling are more accurate during the night, this second method is based on the Total Precipitable Water content obtained by lunar-photometer measurements. Both calibration techniques give similar results with similar associated uncertainties. The main advantage of the lunar approach is that both instrument, are collocated in space and time whereas radiosoundings are rare and expensive.

In terms of perspectives, several important issues must be outlined.

A fraction of the SHADOW-2 campaign data has been analyzed and not all parameters measured by LILAS were considered. For example, spectral depolarization is not considered yet in the inversion scheme. GARRLiC is expected to provide added value parameters such as absorption coefficient profile. Some results have already been obtained by several groups using GRASP/GARRLiC in the framework of ACTRIS JRA-1 activity, but deeper investigation and validation are requested (see PhD thesis, Q.Y. Hu, LOA, in progress).

At both Lille and Dakar sites, additional in situ ground-based measurement are routinely performed (scattering coefficient from nephelometer, absorption coefficient from

aethalometer, size distribution from GRIMM or similar granulometer, ACSM (aerosols chemical speciation), high spectral resolution infrared spectrometer (CHRIS), air quality standard measurements (PM_x). The corresponding boundary “conditions” could be considered in a future version of GRASP/GARRLiC version so as to better describe aerosol properties in the boundary layer with such LiDAR (see PhD thesis, Q.Y. Hu, LOA, in progress).

Up to now, GARRLiC inversion is performed at one given time. The retrieval concept can involve simultaneous inversion of measurements performed at different times, including night-time where only spectral AOD could be obtained in the best case. First attempts have been performed in the framework of ACTRIS-2/JRA-1 (Lopatin et al., 2016, in progress).

In this thesis, we report only the GARRLiC retrievals performed with the LILAS elastic channel (355, 532, 1064 nm). However, single wavelength LiDAR signal and sun/sky-photometer data can also be simultaneously inverted. Now, about 10 years of continuous collocated photometer/LiDAR data in Lille and Dakar can be reprocessed using GRASP/GARRLiC data. Both BASIC and GARRLiC approach could even be compared more extensively in both sites (SHADOW-2 campaign). Since GARRLiC can also be considered for night-time retrievals, the possibility to include Raman channels in the GARRLiC approach is currently under investigation. The forward model has to be enhanced to include Raman signal simulation (A. Lopatin, Q.Y. Hu, work in progress). Regarding aerosol chemical properties, several studies are under investigation (PhD thesis, Lei Li, LOA, in progress). An enhanced forward model included in the GRASP/GARRLiC inversion is currently under development and evaluation. To describe the chemical composition, the inputs of this model are no more aerosols refractive index (real and imaginary) but fractions of a set of predefined aerosol types (BC, BrC, Water, Dust, Iron). In this case, the retrieval is expected to provide the fraction of these elementary aerosol compounds. This work is under progress.

Although our work was mostly focusing on aerosols retrievals, frequent cirrus layers occur. Clearly, the system such as LILAS has a potential for studying aerosols properties in the vicinity of clouds (low level and high level clouds). Relevant observations have been performed during SHADOW-2 campaign (aerosols properties (mostly

dust), water vapor and ice crystals) and a paper is under preparation (Veselovskii et al., 2017).

Finally, we would like to outline the importance of designing a processing system which is able to inverse multi-source data jointly, it could based on GRASP developments. Such an operational system coupled to EARLINET SCC (Single Calculus Chain) software will be extremely valuable for a wide community. This is one of the central concept/project that France is promoting for the future ACTRIS-Research Infrastructure. Additionally, ESA is willing to support the initiative, since current advances in atmospheric composition measurements from space require access to independent, high-quality, global atmospheric composition ground-based data for the validation of the upcoming European EO missions and payloads S3, S5p, ADM-Aeolus, EarthCARE, S4, S5, MERLIN, GOME-2c, 3MI. Additionally, the flexible inversion concept of GRASP approach can involve both satellite and ground-based co-located data, which will open a new area of very promising multi-source aerosol retrievals. It will enhance present studies on joint ground-based and airborne retrievals (Amiridis et al., 2012; Amiridis et al., 2015). Also, it is possible to adapt and use GRASP/GARRLIC to reprocess CALIOP data together with PARASOL/MODIS data.

Bibliography

- Adam, John A. (2015). "Scattering of electromagnetic plane waves in radially inhomogeneous media: ray theory, exact solutions and connections with potential scattering theory". In: *Light Scattering Reviews 9: Light Scattering and Radiative Transfer*. Ed. by Alexander A. Kokhanovsky. Berlin, Heidelberg: Springer Berlin Heidelberg, pp. 101–130. ISBN: 978-3-642-37985-7.
- Albrecht, Bruce A (1989). "Aerosols, cloud microphysics, and fractional cloudiness". In: *Science* 245.4923, pp. 1227–1230.
- Amiridis, V et al. (2005). "Four-year aerosol observations with a Raman lidar at Thessaloniki, Greece, in the framework of European Aerosol Research Lidar Network (EARLINET)". In: *Journal of Geophysical Research: Atmospheres* 110.D21.
- Amiridis, V. et al. (2009a). "Optical characteristics of biomass burning aerosols over Southeastern Europe determined from UV-Raman lidar measurements". In: *Atmospheric Chemistry and Physics* 9.7, pp. 2431–2440. DOI: 10.5194/acp-9-2431-2009. URL: <http://www.atmos-chem-phys.net/9/2431/2009/>.
- Amiridis, V. et al. (2009b). "The potential of the synergistic use of passive and active remote sensing measurements for the validation of a regional dust model". In: *Annales Geophysicae* 27.8, pp. 3155–3164. DOI: 10.5194/angeo-27-3155-2009. URL: <http://www.ann-geophys.net/27/3155/2009/>.
- Amiridis, V. et al. (2012). "Impact of the 2009 Attica wild fires on the air quality in urban Athens". In: *Atmospheric Environment* 46, pp. 536–544. ISSN: 1352-2310. DOI: <http://dx.doi.org/10.1016/j.atmosenv.2011.07.056>. URL: <http://www.sciencedirect.com/science/article/pii/S1352231011008004>.
- Amiridis, V. et al. (2015). "LIVAS: a 3-D multi-wavelength aerosol/cloud database based on CALIPSO and EARLINET". In: *Atmospheric Chemistry and Physics* 15.13, pp. 7127–7153. DOI: 10.5194/acp-15-7127-2015. URL: <http://www.atmos-chem-phys.net/15/7127/2015/>.

- Amiridis, Vassilis et al. (2011). "Characterization of the aerosol type using simultaneous measurements of the lidar ratio and estimations of the single scattering albedo". In: *Atmospheric Research* 101.1, pp. 46–53.
- Ancellet, G. et al. (2016). "Long-range transport and mixing of aerosol sources during the 2013 North American biomass burning episode: analysis of multiple lidar observations in the western Mediterranean basin". In: *Atmospheric Chemistry and Physics* 16.7, pp. 4725–4742. DOI: 10.5194/acp-16-4725-2016. URL: <http://www.atmos-chem-phys.net/16/4725/2016/>.
- Andreae, Meinrat O. and Paul J. Crutzen (1997). "Atmospheric Aerosols: Biogeochemical Sources and Role in Atmospheric Chemistry". In: *Science* 276.5315, pp. 1052–1058. DOI: 10.1126/science.276.5315.1052. eprint: <http://www.sciencemag.org/content/276/5315/1052.full.pdf>. URL: <http://www.sciencemag.org/content/276/5315/1052.abstract>.
- Ångström, Anders (1964). "The parameters of atmospheric turbidity". In: *Tellus* 16.1, pp. 64–75.
- Ansmann, Albert, Maren Riebesell, and Claus Weitkamp (1990). "Measurement of atmospheric aerosol extinction profiles with a Raman lidar". In: *Opt. Lett.* 15.13, pp. 746–748. DOI: 10.1364/OL.15.000746. URL: <http://ol.osa.org/abstract.cfm?URI=ol-15-13-746>.
- Babenko, Victor A, Ludmila G Astafyeva, and Vladimir N Kuz'min (2003). *Electromagnetic scattering in disperse media: inhomogeneous and anisotropic particles*. Springer Science & Business Media.
- Barnaba, Francesca and Gian Paolo Gobbi (2001). "Lidar estimation of tropospheric aerosol extinction, surface area and volume: Maritime and desert-dust cases". In: *Journal of Geophysical Research: Atmospheres* 106.D3, pp. 3005–3018. ISSN: 2156-2202. DOI: 10.1029/2000JD900492. URL: <http://dx.doi.org/10.1029/2000JD900492>.
- Barreto, A et al. (2013). "A new method for nocturnal aerosol measurements with a lunar photometer prototype". In: *Atmospheric Measurement Techniques* 6.3, pp. 585–598.

- Biniotoglou, I. et al. (2015). "A methodology for investigating dust model performance using synergistic EARLINET/AERONET dust concentration retrievals". In: *Atmospheric Measurement Techniques* 8.9, pp. 3577–3600. DOI: 10.5194/amt-8-3577-2015. URL: <http://www.atmos-meas-tech.net/8/3577/2015/>.
- Bohren, Craig F and Donald R Huffman (2008). *Absorption and scattering of light by small particles*. John Wiley & Sons.
- Boichu, M et al. (2015). "Temporal variations of flux and altitude of sulfur dioxide emissions during volcanic eruptions: implications for long-range dispersal of volcanic clouds". In: *Atmospheric Chemistry and Physics Discussions* 15.4, pp. 5031–5077.
- Bond, Tami C et al. (2007). "Historical emissions of black and organic carbon aerosol from energy-related combustion, 1850–2000". In: *Global Biogeochemical Cycles* 21.2.
- Bösenberg, J et al. (2007). "Plan for the implementation of the GAW Aerosol Lidar Observation Network (GALION)". In: *WMO/TD 1443*, p. 178.
- Boucher, Olivier (1999). "Air traffic may increase cirrus cloudiness". In: *Nature* 397.6714, pp. 30–31.
- Bovchaliuk, V. et al. (2016). "Comparison of aerosol properties retrieved using GARRLiC, LIRIC, and Raman algorithms applied to multi-wavelength lidar and sun/sky-photometer data". In: *Atmospheric Measurement Techniques* 9.7, pp. 3391–3405. DOI: 10.5194/amt-9-3391-2016. URL: <http://www.atmos-meas-tech.net/9/3391/2016/>.
- Brasseur, Guy, John J Orlando, Geoffrey S Tyndall, et al. (1999). *Atmospheric chemistry and global change*. Oxford University Press.
- Bruneau, D. et al. (2015). "355-nm high spectral resolution airborne lidar LNG: system description and first results". In: *Appl. Opt.* 54.29, pp. 8776–8785. DOI: 10.1364/AO.54.008776. URL: <http://ao.osa.org/abstract.cfm?URI=ao-54-29-8776>.
- Chaikovsky, A et al. (2004). "CIMEL and multiwavelength lidar measurements for troposphere aerosol altitude distributions investigation, long-range transfer monitoring and regional ecological problems solution: field validation of retrieval techniques". In: *Optica Pura y Aplicada* 37, pp. 3241–3246.

- Chaikovsky, A. et al. (2012). "Algorithm and Software for the retrieval of vertical aerosol properties using combined Lidar/Radiometer data: dissemination in AERLINET". In: 26th International Laser Radar Conference, 2012, Porto Heli, Greece, pp. 339–402.
- Chaikovsky, A. et al. (2015). "Lidar-Radiometer Inversion Code (LIRIC) for the retrieval of vertical aerosol properties from combined lidar/radiometer data: development and distribution in EARLINET". In: *Atmospheric Measurement Techniques Discussions* 8.12, pp. 12759–12822. DOI: 10.5194/amt-d-8-12759-2015. URL: <http://www.atmos-meas-tech-discuss.net/8/12759/2015/>.
- Charlson, Robert J et al. (1992). "Climate forcing by anthropogenic aerosols". In: *Science* 255.5043, pp. 423–430.
- Claquin, T et al. (1998). "Uncertainties in assessing radiative forcing by mineral dust". In: *Tellus B* 50.5, pp. 491–505.
- Coakley Jr., James A. and Ping Yang (2014). *Atmospheric Radiation*. Wiley-VCH. ISBN: 978-3-527-68144-0.
- Draxler, R. R. and G. D. Rolph (2015). *HYSPLIT (HYbrid Single-Particle Lagrangian Integrated Trajectory) Model access via NOAA ARL READY Website*. URL: <http://ready.arl.noaa.gov/HYSPLIT.php>.
- Dubovik, O et al. (2000). "Accuracy assessments of aerosol optical properties retrieved from Aerosol Robotic Network(AERONET) Sun and sky radiance measurements". In: *Journal of Geophysical Research* 105.D8, pp. 9791–9806.
- Dubovik, O et al. (2002a). "Non-spherical aerosol retrieval method employing light scattering by spheroids". In: *Geophysical Research Letters* 29.10, pp. 54–1.
- Dubovik, O. et al. (2002b). "Variability of Absorption and Optical Properties of Key Aerosol Types Observed in Worldwide Locations". In: *J. Atmos. Sci.* 59, pp. 590–608. URL: [http://dx.doi.org/10.1175/1520-0469\(2002\)059<0590:VOAAOP>2.0.CO;2](http://dx.doi.org/10.1175/1520-0469(2002)059<0590:VOAAOP>2.0.CO;2).
- Dubovik, O et al. (2008). "Retrieving global aerosol sources from satellites using inverse modeling". In: *Atmospheric Chemistry and Physics* 8.2, pp. 209–250.
- Dubovik, O. et al. (2011). "Statistically optimized inversion algorithm for enhanced retrieval of aerosol properties from spectral multi-angle polarimetric satellite observations". In: *Atmospheric Measurement Techniques* 4.5, pp. 975–1018. DOI: 10.5194/

- amt-4-975-2011. URL: <http://www.atmos-meas-tech.net/4/975/2011/>.
- Dubovik, Oleg (2004). "Optimization of numerical inversion in photopolarimetric remote sensing". In: *Photopolarimetry in remote sensing*. Springer, pp. 65–106.
- Dubovik, Oleg and Michael D. King (2000). "A flexible inversion algorithm for retrieval of aerosol optical properties from Sun and sky radiance measurements". In: *Journal of Geophysical Research: Atmospheres* 105.D16, pp. 20673–20696. ISSN: 2156-2202. DOI: 10.1029/2000JD900282. URL: <http://dx.doi.org/10.1029/2000JD900282>.
- Dubovik, Oleg et al. (2006). "Application of spheroid models to account for aerosol particle nonsphericity in remote sensing of desert dust". In: *Journal of Geophysical Research: Atmospheres (1984–2012)* 111.D11.
- Dubovik, Oleg et al. (2014). "GRASP: a versatile algorithm for characterizing the atmosphere". In: *SPIE: Newsroom*.
- Eck, Thomas F et al. (2010). "Climatological aspects of the optical properties of fine/coarse mode aerosol mixtures". In: *Journal of Geophysical Research: Atmospheres (1984–2012)* 115.D19.
- Ferrare, RA et al. (1995). "A comparison of water vapor measurements made by Raman lidar and radiosondes". In: *Journal of Atmospheric and Oceanic Technology* 12.6, pp. 1177–1195.
- Foth, A et al. (2015). "Water vapour profiles from Raman lidar automatically calibrated by microwave radiometer data during HOPE". In: *Atmospheric Chemistry and Physics* 15.14, pp. 7753–7763.
- Freudenthaler, V. (2007). *EARLINET-ASOS NA3, Internal LIDAR checkup procedures*. Tech. rep. The institution that published. URL: http://www.actris.net/Portals/97/Publications/quality%20standards/lidar/QA-InternalCheckups_version_121017b.pdf.
- (2008). "The telecover test: A quality assurance tool for the optical part of a LIDAR system". In: URL: http://epub.ub.uni-muenchen.de/12958/1/ILRC24-2008-S01P_30_Freudenthaler_Poster.pdf.
- (2010). "EARLINET Quality Assurance - NA3". In: URL: https://www.earlinet.org/index.php?eID=tx_nawsecured1&u=0&g=0&t=1450983137&

hash=9c63dd3c8f560d112afce6e39d235a3bf7c590a4&file=fileadmin/_migrated/content_uploads/Quality_assurance_program__Volker_Freudenthaler_.pdf.

Freudenthaler, V. et al. "European Aerosol Research LIDAR Network - advanced sustainable observation system (EARLINET-ASOS). Plans for quality assurance". URL: <http://www.meteo.physik.uni-muenchen.de/~st212fre/ILRC23/Freudenthaler.pdf>.

Freudenthaler, V. et al. (2009). "Depolarization ratio profiling at several wavelengths in pure Saharan dust during SAMUM 2006". In: *Tellus B* 61, pp. 165–179. DOI: 10.1111/j.1600-0889.2008.00396.x.

Gao, Bo-Cai and Alexander FH Goetz (1990). "Determination of total column water vapor in the atmosphere at high spatial resolution from AVIRIS data using spectral curve fitting and band ratioing techniques". In: *Imaging Spectroscopy of the Terrestrial Environment*. International Society for Optics and Photonics, pp. 138–149.

Granados-Muñoz, M. J. et al. (2014). "Retrieving aerosol microphysical properties by Lidar-Radiometer Inversion Code (LIRIC) for different aerosol types". In: *Journal of Geophysical Research: Atmospheres* 119.8. 2013JD021116, pp. 4836–4858. ISSN: 2169-8996. DOI: 10.1002/2013JD021116. URL: <http://dx.doi.org/10.1002/2013JD021116>.

Groß, Silke et al. (2011). "Characterization of Saharan dust, marine aerosols and mixtures of biomass-burning aerosols and dust by means of multi-wavelength depolarization and Raman lidar measurements during SAMUM 2". In: *Tellus B* 63.4. ISSN: 1600-0889. URL: <http://www.tellusb.net/index.php/tellusb/article/view/16369>.

Guerrero-Rascado, J. L. et al. (2014). "Towards an instrumental harmonization in the framework of LALINET: dataset of technical specifications". In: *Proc. SPIE* 9246. DOI: 10.1117/12.2066873.

Hänel, Gottfried (1976). "The properties of atmospheric aerosol particles as functions of the relative humidity at thermodynamic equilibrium with the surrounding moist air". In: *Adv. Geophys* 19.1, pp. 73–188.

Haustein, K. et al. (2012). "Atmospheric dust modeling from meso to global scales with the online NMMB/BSC-Dust model. Part 2: Experimental campaigns in Northern

- Africa". In: *Atmospheric Chemistry and Physics* 12.6, pp. 2933–2958. DOI: 10.5194/acp-12-2933-2012. URL: <http://www.atmos-chem-phys.net/12/2933/2012/>.
- Haywood, James and Olivier Boucher (2000). "Estimates of the direct and indirect radiative forcing due to tropospheric aerosols: A review". In: *REVIEWS OF GEOPHYSICS-RICHMOND VIRGINIA THEN WASHINGTON* 38.4, pp. 513–543.
- Heintzenberg, Jost (1994). "Properties of the log-normal particle size distribution". In: *Aerosol Science and Technology* 21.1, pp. 46–48.
- Holben, BN et al. (1998). "AERONET – A federated instrument network and data archive for aerosol characterization". In: *Remote sensing of environment* 66.1, pp. 1–16.
- Hulst, Hendrik Christoffel and HC Van De Hulst (1957). *Light scattering by small particles*. Courier Corporation.
- IPCC (2007). *Climate Change 2007 - The Physical Science Basis: Working Group I Contribution to the Fourth Assessment Report of the IPCC*. Ed. by S. Solomon et al. Cambridge, UK and New York, NY, USA: Cambridge University Press. ISBN: 0521880092. URL: <http://www.worldcat.org/isbn/0521880092>.
- (2013). *Climate Change 2013: The Physical Science Basis. Contribution of Working Group I to the Fifth Assessment Report of the Intergovernmental Panel on Climate Change*. Ed. by T. F. Stocker et al. Cambridge University Press, p. 1535. ISBN: 9781107661820. URL: <http://www.worldcat.org/isbn/9781107661820>.
- Johnson, BT, KP Shine, and PM Forster (2004). "The semi-direct aerosol effect: Impact of absorbing aerosols on marine stratocumulus". In: *Quarterly Journal of the Royal Meteorological Society* 130.599, pp. 1407–1422.
- Joseph, M (1999). "Long-term measurements of the transport of African mineral dust to the southeastern United States: Implications for regional air quality". In:
- Josset, Damien et al. (2011). "CALIPSO lidar ratio retrieval over the ocean". In: *Opt. Express* 19.19, pp. 18696–18706. DOI: 10.1364/OE.19.018696. URL: <http://www.opticsexpress.org/abstract.cfm?URI=oe-19-19-18696>.
- Kasten, Fritz and Andrew T Young (1989). "Revised optical air mass tables and approximation formula". In: *Applied optics* 28.22, pp. 4735–4738.

- Kaufman, Yoram J, Didier Tanré, and Olivier Boucher (2002). "A satellite view of aerosols in the climate system". In: *Nature* 419.6903, pp. 215–223.
- Kienle, T. et al. (1990). "Satellite surveillance of volcanic ash plumes, application to aircraft safety". In: *Eos, Transactions American Geophysical Union* 71.7, pp. 266–266. ISSN: 2324-9250. DOI: 10.1029/90EO00046. URL: <http://dx.doi.org/10.1029/90EO00046>.
- Klett, James D. (1981). "Stable analytical inversion solution for processing lidar returns". In: *Appl. Opt.* 20.2, pp. 211–220. DOI: 10.1364/AO.20.000211. URL: <http://ao.osa.org/abstract.cfm?URI=ao-20-2-211>.
- (1985). "Lidar inversion with variable backscatter/extinction ratios". In: *Appl. Opt.* 24.11, pp. 1638–1643. DOI: 10.1364/AO.24.001638. URL: <http://ao.osa.org/abstract.cfm?URI=ao-24-11-1638>.
- Koch, D and AD Del Genio (2010). "Black carbon semi-direct effects on cloud cover: review and synthesis". In: *Atmospheric Chemistry and Physics* 10.16, pp. 7685–7696.
- Kokhanovsky, AA et al. (2015). "Space-based remote sensing of atmospheric aerosols: The multi-angle spectro-polarimetric frontier". In: *Earth-Science Reviews* 145, pp. 85–116.
- Krueger, Arlin J and Raymond A Minzner (1976). "A mid-latitude ozone model for the 1976 US Standard Atmosphere". In: *Journal of Geophysical Research* 81.24, pp. 4477–4481.
- Lange, Diego et al. (2012). "Optimized data-gluing method for mixed analog/photon-counting lidar signals". In: *Revista Boliviana de Física* 20.20, pp. 4–6.
- Leblanc, Thierry and I Stuart McDermid (2008). "Accuracy of Raman lidar water vapor calibration and its applicability to long-term measurements". In: *Applied optics* 47.30, pp. 5592–5603.
- Lenoble, J., L. Remer, and D. Tanré (2013). *Aerosol Remote Sensing*. Springer-Praxis. ISBN: 9783642177255.
- Lenoble, Jacqueline (1993). "Atmospheric radiative transfer". In: *Studies in Geophysical Optics and Remote Sensing, Hampton, VA: A. Deepak Pub., | c1993* 1.
- Lohmann, Ulrike and Johann Feichter (2005). "Global indirect aerosol effects: a review". In: *Atmospheric Chemistry and Physics* 5.3, pp. 715–737.

- Lohmann, Ulrike, Bernd Kärcher, and Claudia Timmreck (2003). "Impact of the Mount Pinatubo eruption on cirrus clouds formed by homogeneous freezing in the ECHAM4 GCM". In: *Journal of Geophysical Research: Atmospheres* (1984–2012) 108.D18.
- Lopatin, A. et al. (2013). "Enhancement of aerosol characterization using synergy of lidar and sun-photometer coincident observations: the GARRLiC algorithm". In: *Atmospheric Measurement Techniques* 6.8, pp. 2065–2088. DOI: 10.5194/amt-6-2065-2013. URL: <http://www.atmos-meas-tech.net/6/2065/2013/>.
- Lopatin, Anton (2013). "Enhanced remote sensing of atmospheric aerosol by joint inversion of active and passive remote sensing observations". PhD thesis. Université des Sciences et Technologies de Lille.
- Madonna, F et al. (2011). "CIAO: the CNR-IMAA advanced observatory for atmospheric research". In: *Atmospheric Measurement Techniques* 4.6, pp. 1191–1208.
- Marconi, M et al. (2014). "Saharan dust aerosol over the central Mediterranean Sea: PM 10 chemical composition and concentration versus optical columnar measurements". In: *Atmospheric Chemistry and Physics* 14.4, pp. 2039–2054.
- Meloni, Daniela et al. (2005). "Influence of the vertical profile of Saharan dust on the visible direct radiative forcing". In: *Journal of Quantitative Spectroscopy and Radiative Transfer* 93.4, pp. 397–413.
- Miloshevich, Larry M et al. (2009). "Accuracy assessment and correction of Vaisala RS92 radiosonde water vapor measurements". In: *Journal of Geophysical Research: Atmospheres* 114.D11.
- Mishchenko, Michael I (2014). *Electromagnetic scattering by particles and particle groups: an introduction*. Cambridge University Press.
- Mishchenko, Michael I et al. (1997). "Modeling phase functions for dustlike tropospheric aerosols using a shape mixture of randomly oriented polydisperse spheroids". In: *Journal of Geophysical Research: Atmospheres* (1984–2012) 102.D14, pp. 16831–16847.
- Moosmüller, H, RK Chakrabarty, and WP Arnott (2009). "Aerosol light absorption and its measurement: A review". In: *Journal of Quantitative Spectroscopy and Radiative Transfer* 110.11, pp. 844–878.
- Mortier, A. et al. (2013). "Detection and characterization of volcanic ash plumes over Lille during the Eyjafjallajökull eruption". In: *Atmospheric Chemistry and Physics*

- 13.7, pp. 3705–3720. DOI: 10.5194/acp-13-3705-2013. URL: <http://www.atmos-chem-phys.net/13/3705/2013/>.
- Muhs, Daniel R et al. (2007). “Geochemical evidence for African dust inputs to soils of western Atlantic islands: Barbados, the Bahamas, and Florida”. In: *Journal of Geophysical Research: Earth Surface* 112.F2.
- Müller, D. et al. (2007). “Aerosol-type-dependent lidar ratios observed with Raman lidar”. In: *Journal of Geophysical Research: Atmospheres* 112.D16. D16202, n/a–n/a. ISSN: 2156-2202. DOI: 10.1029/2006JD008292. URL: <http://dx.doi.org/10.1029/2006JD008292>.
- Müller, D. et al. (2010). “Mineral dust observed with AERONET Sun photometer, Raman lidar, and in situ instruments during SAMUM 2006: Shape-dependent particle properties”. In: *Journal of Geophysical Research: Atmospheres* 115.D11. D11207, n/a–n/a. ISSN: 2156-2202. DOI: 10.1029/2009JD012523. URL: <http://dx.doi.org/10.1029/2009JD012523>.
- Müller, Detlef, Ulla Wandinger, and Albert Ansmann (1999). “Microphysical particle parameters from extinction and backscatter lidar data by inversion with regularization: theory”. In: *Appl. Opt.* 38.12, pp. 2346–2357. DOI: 10.1364/AO.38.002346. URL: <http://ao.osa.org/abstract.cfm?URI=ao-38-12-2346>.
- Müller, Detlef et al. (2013). “Vertical profiles of pure dust and mixed smoke–dust plumes inferred from inversion of multiwavelength Raman/polarization lidar data and comparison to AERONET retrievals and in situ observations”. In: *Appl. Opt.* 52.14, pp. 3178–3202. DOI: 10.1364/AO.52.003178. URL: <http://ao.osa.org/abstract.cfm?URI=ao-52-14-3178>.
- Muñoz, María José Granados (2014). “Characterizing the atmospheric aerosol by active and passive remote sensing: microphysical properties and hygroscopic growth effects”. PhD thesis. Universidad de Granada.
- Murayama, Toshiyuki et al. (2001). “Ground-based network observation of Asian dust events of April 1998 in east Asia”. In: *Journal of Geophysical Research: Atmospheres* 106.D16, pp. 18345–18359. ISSN: 2156-2202. DOI: 10.1029/2000JD900554. URL: <http://dx.doi.org/10.1029/2000JD900554>.

- Navas-Guzmán, Francisco et al. (2014). "Tropospheric water vapour and relative humidity profiles from lidar and microwave radiometry". In: *Atmospheric Measurement Techniques* 7.5, pp. 1201–1211.
- Olmo, F.J. et al. (2006). "Preliminary results of a non-spherical aerosol method for the retrieval of the atmospheric aerosol optical properties". In: *Journal of Quantitative Spectroscopy and Radiative Transfer* 100.1-3. {VIII} Conference on Electromagnetic and Light Scattering by Nonspherical Particles VIII Conference on Electromagnetic and Light Scattering by Nonspherical Particles, pp. 305–314. ISSN: 0022-4073. DOI: <http://dx.doi.org/10.1016/j.jqsrt.2005.11.047>. URL: <http://www.sciencedirect.com/science/article/pii/S002240730500395X>.
- Pappalardo, G. et al. (2014). "EARLINET: towards an advanced sustainable European aerosol lidar network". In: *Atmospheric Measurement Techniques* 7.8, pp. 2389–2409. DOI: 10.5194/amt-7-2389-2014. URL: <http://www.atmos-meas-tech.net/7/2389/2014/>.
- Pelon, Jacques et al. (2011). "L'apport des nouvelles missions spatiales à sondeurs actifs : Résultats récents de CALIPSO, CloudSat et l'A-Train". In: *La Météorologie* 75, pp. 15–22. URL: <https://hal.archives-ouvertes.fr/hal-00675203>.
- Pelon, Jacques et al. (2013). *LIDAR and RADAR Observations*. Wiley-VCH Verlag GmbH and Co. KGaA, pp. 457–526. ISBN: 9783527653218. DOI: 10.1002/9783527653218.ch9. URL: <http://dx.doi.org/10.1002/9783527653218.ch9>.
- Pérez, C. et al. (2011). "Atmospheric dust modeling from meso to global scales with the online NMMB/BSC-Dust model – Part 1: Model description, annual simulations and evaluation". In: *Atmospheric Chemistry and Physics Discussions* 11.6, pp. 17551–17620. DOI: 10.5194/acpd-11-17551-2011. URL: <http://www.atmos-chem-phys-discuss.net/11/17551/2011/>.
- Pincus, Robert and Marcia B Baker (1994). "Effect of precipitation on the albedo susceptibility of clouds in the marine boundary layer". In: *Nature* 372.6503, pp. 250–252.
- Prospero, J. M. (1996). "Saharan Dust Transport Over the North Atlantic Ocean and Mediterranean: An Overview". In: *The Impact of Desert Dust Across the Mediterranean*. Ed. by Stefano Guerzoni and Roy Chester. Springer Netherlands, pp. 133–151. ISBN:

- 978-94-017-3354-0. DOI: 10.1007/978-94-017-3354-0_13. URL: http://dx.doi.org/10.1007/978-94-017-3354-0_13.
- Raut, J-C and P Chazette (2007). "Retrieval of aerosol complex refractive index from a synergy between lidar, sunphotometer and in situ measurements during LISAIR experiment". In: *Atmospheric Chemistry and Physics* 7.11, pp. 2797–2815.
- Reichardt, Jens et al. (1996). "Combined Raman lidar for aerosol, ozone, and moisture measurements". In: *Optical Engineering* 35.5, pp. 1457–1465.
- Reichardt, Jens et al. (2000). "Rotational vibrational–rotational Raman differential absorption lidar for atmospheric ozone measurements: methodology and experiment". In: *Applied optics* 39.33, pp. 6072–6079.
- Rocken, Christian et al. (1995). "GPS/STORM-GPS sensing of atmospheric water vapor for meteorology". In: *Journal of Atmospheric and Oceanic Technology* 12.3, pp. 468–478.
- Rolph, G. D. (2015). *Real-time Environmental Applications and Display sYstem (READY) Website*. URL: <http://ready.arl.noaa.gov>.
- Russell, Philip B, Thomas J Swisler, and M Patrick McCormick (1979). "Methodology for error analysis and simulation of lidar aerosol measurements". In: *Applied optics* 18.22, pp. 3783–3797.
- Samset, BH et al. (2013). "Black carbon vertical profiles strongly affect its radiative forcing uncertainty". In: *Atmospheric Chemistry and Physics* 13, pp. 2423–2434.
- Schläpfer, Daniel et al. (1998). "Atmospheric precorrected differential absorption technique to retrieve columnar water vapor". In: *Remote Sensing of Environment* 65.3, pp. 353–366.
- Schmid, B et al. (1996). "Comparison of modeled and empirical approaches for retrieving columnar water vapor from solar transmittance measurements in the 0.94- μm region". In: *Journal of Geophysical Research: Atmospheres (1984–2012)* 101.D5, pp. 9345–9358.
- Seibert, Petra et al. (2000). "Review and intercomparison of operational methods for the determination of the mixing height". In: *Atmospheric environment* 34.7, pp. 1001–1027.
- Seinfeld, John H. and Spyros N. Pandis (2006). *Atmospheric Chemistry and Physics: From Air Pollution to Climate Change*. Wiley. ISBN: 9780471720188.

- Shcherbakov, Valery (2007). "Regularized algorithm for Raman lidar data processing". In: *Appl. Opt.* 46.22, pp. 4879–4889. DOI: 10.1364/AO.46.004879. URL: <http://ao.osa.org/abstract.cfm?URI=ao-46-22-4879>.
- Shipley, Scott T et al. (1983). "High spectral resolution lidar to measure optical scattering properties of atmospheric aerosols. 1: Theory and instrumentation". In: *Applied optics* 22.23, pp. 3716–3724.
- Sokolik, IN et al. (2001). "Introduction to special section: Outstanding problems in quantifying the radiative impacts of mineral dust". In: *Journal of Geophysical Research: Atmospheres (1984–2012)* 106.D16, pp. 18015–18027.
- Stocker, TF et al. (2013). *IPCC, 2013: summary for policymakers in climate change 2013: the physical science basis, contribution of working group I to the fifth assessment report of the intergovernmental panel on climate change*.
- Takamura, T, T Nakajima, et al. (2004). "Overview of SKYNET and its activities". In: *Opt. Pura Apl* 37.3, pp. 3303–3308.
- Tanré, D et al. (2003). "Measurement and modeling of the Saharan dust radiative impact: Overview of the Saharan Dust Experiment (SHADE)". In: *Journal of Geophysical Research: Atmospheres (1984–2012)* 108.D18.
- Tsekeri, A et al. (2013). "Application of a synergetic lidar and sunphotometer algorithm for the characterization of a dust event over Athens, Greece". In: *British Journal of Environment and Climate Change* 3.4, p. 531.
- Turner, David D and JEM Goldsmith (1999). "Twenty-four-hour Raman lidar water vapor measurements during the Atmospheric Radiation Measurement Program's 1996 and 1997 water vapor intensive observation periods". In: *Journal of Atmospheric and Oceanic Technology* 16.8, pp. 1062–1076.
- Twomey, S (1974). "Pollution and the planetary albedo". In: *Atmospheric Environment (1967)* 8.12, pp. 1251–1256.
- Twomey, Sean (1977). "The influence of pollution on the shortwave albedo of clouds". In: *Journal of the atmospheric sciences* 34.7, pp. 1149–1152.
- Uthe, Edward E (1982). "Particle size evaluations using multiwavelength extinction measurements". In: *Applied optics* 21.3, pp. 454–459.

- Veselovskii, I et al. (2012). "Linear estimation of particle bulk parameters from multi-wavelength lidar measurements". In: *Atmospheric Measurement Techniques* 5.5, pp. 1135–1145.
- Veselovskii, I et al. (2015). "Use of rotational Raman measurements in multiwavelength aerosol lidar for evaluation of particle backscattering and extinction". In: *Atmospheric Measurement Techniques* 8.10, pp. 4111–4122.
- Veselovskii, I et al. (2016). "Retrieval of optical and physical properties of African dust from multiwavelength Raman lidar measurements during the SHADOW campaign in Senegal". In: *Atmospheric Chemistry and Physics* 16.11, p. 7013.
- Veselovskii, Igor et al. (2002). "Inversion with regularization for the retrieval of tropospheric aerosol parameters from multiwavelength lidar sounding". In: *Appl. Opt.* 41.18, pp. 3685–3699. DOI: 10.1364/AO.41.003685. URL: <http://ao.osa.org/abstract.cfm?URI=ao-41-18-3685>.
- Veselovskii, Igor et al. (2004). "Inversion of multiwavelength Raman lidar data for retrieval of bimodal aerosol size distribution". In: *Appl. Opt.* 43.5, pp. 1180–1195. DOI: 10.1364/AO.43.001180. URL: <http://ao.osa.org/abstract.cfm?URI=ao-43-5-1180>.
- Veselovskii, Igor et al. (2010). "Application of randomly oriented spheroids for retrieval of dust particle parameters from multiwavelength lidar measurements". In: *Journal of Geophysical Research: Atmospheres (1984–2012)* 115.D21.
- Wagner, J. et al. (2013). "Evaluation of the Lidar/Radiometer Inversion Code (LIRIC) to determine microphysical properties of volcanic and desert dust". In: *Atmospheric Measurement Techniques* 6.7, pp. 1707–1724. DOI: 10.5194/amt-6-1707-2013. URL: <http://www.atmos-meas-tech.net/6/1707/2013/>.
- Wandinger, Ulla et al. (1995). "Determination of stratospheric aerosol microphysical properties from independent extinction and backscattering measurements with a Raman lidar". In: *Appl. Opt.* 34.36, pp. 8315–8329. DOI: 10.1364/AO.34.008315. URL: <http://ao.osa.org/abstract.cfm?URI=ao-34-36-8315>.
- Washington, Richard et al. (2003). "Dust-storm source areas determined by the total ozone monitoring spectrometer and surface observations". In: *Annals of the Association of American Geographers* 93.2, pp. 297–313.

- Weitkamp, Claus (2005). *Lidar: range-resolved optical remote sensing of the atmosphere*. Springer series in optical sciences. ISBN: 9780387251011.
- The Nasa Micro-Pulse Lidar Network (MPLNET): co-location of lidars with AERONET sun-photometers and related Earth Science applications* (2005).
- Welton, Ellsworth J. et al. (2001). "Global monitoring of clouds and aerosols using a network of micropulse lidar systems". In: *Proc. SPIE* 4153, pp. 151–158. DOI: 10.1117/12.417040. URL: <http://dx.doi.org/10.1117/12.417040>.
- Whiteman, DN, SH Melfi, and RA Ferrare (1992). "Raman lidar system for the measurement of water vapor and aerosols in the Earth's atmosphere". In: *Applied Optics* 31.16, pp. 3068–3082.
- Wiegner, M et al. (2009). "Numerical simulations of optical properties of Saharan dust aerosols with emphasis on lidar applications". In: *Tellus B* 61.1, pp. 180–194.
- Winker, David M, Jacques R Pelon, and M Patrick McCormick (2003). "The CALIPSO mission: Spaceborne lidar for observation of aerosols and clouds". In: *Third International Asia-Pacific Environmental Remote Sensing Remote Sensing of the Atmosphere, Ocean, Environment, and Space*. International Society for Optics and Photonics, pp. 1–11.
- Winker, DM et al. (2010). "The CALIPSO mission: A global 3D view of aerosols and clouds". In: *Bulletin of the American Meteorological Society* 91.9, p. 1211.
- Zhang, Yunpeng et al. (2014). "Slope characterization in combining analog and photon count data from atmospheric lidar measurements". In: *Applied optics* 53.31, pp. 7312–7320.